UNIVERSIDAD CARLOS III DE MADRID
ESCUELA POLITÉCNICA SUPERIOR

Universidad
Carlos III de Madrid

EXPERIMENTAL STUDY OF A BUBBLING FLUIDIZED BED WITH A ROTATING DISTRIBUTOR

Tesis Doctoral

Por
Celia Sobrino Fernández
Ingeniera Industrial

Leganés, Madrid, Junio 2008

DEPARTAMENTO DE INGENIERÍA TÉRMICA Y DE FLUIDOS
ESCUELA POLITÉCNICA SUPERIOR

EXPERIMENTAL STUDY OF A BUBBLING FLUIDIZED BED WITH A ROTATING DISTRIBUTOR

Autora
Celia Sobrino Fernández
Ingeniera Industrial

Directora de Tesis
Mercedes de Vega Blázquez
Doctora Ingeniera Industrial

Leganés, Madrid, Junio 2008

A mis padres, a Elena

Acknowledgements

I would like to thanks the many people who helped me throughout the process of developing this thesis and also all those who had an important role during my PhD years.
Those who know me, know how important has been for me the assistance of my PhD advisor, Mercedes de Vega. She was always there to supervise and help with every single aspect of the research: lab work, discussions, writing... Her patience, rigor and bright ideas were crucial for this work. It was a real pleasure to work with her.
I am grateful to all PhD students in my Department with whom I shared a nice time and a confortable environment to work. I am specially grateful to Jose Antonio Almendros who began with me this "adventure" and was a real learning source. Rafael Salgado was the perfect office mate. I have to thank him for the 3D schematics of the experimental device. Sergio Sánchez provided the needed encouragement during these years and he was an example of predisposition and goodwill.
I want to thank Domingo Santana who provided a lot of ideas for this thesis, specially concerning the mathematical methods. His advises and experience helped a lot to focus my research. I have also to thank Ulpiano Ruiz-Rivas for the manuscript corrections.
I am indebted to Javier Rodriguez. I could never thank him enough for his help with the manuscript revision, the lab work and the Fluid-Mechanics.
I also want to thank the professors that taught me Fluid-Mechanics: Inmaculada Iglesias, Antonio Sánchez, Marcos Vera and Javier Rodriguez.
I have also to thank my group colleagues Néstor García, for his sense of humor, Antonio Acosta who was always willing to help and Antonio Soria.
Manuel Santos and Carlos Cobos had a crucial role in this thesis. I am indebted to Manuel Santos for his bright ideas and enormous help with the rotating device and Carlos Cabos who was always there when is technical knowledge was needed. David Díaz and Israel Pina also took part in the arrangement of the experimental set-up.
I am grateful to Maria Pavón, for her assistant with the paperwork.
I wish to thank Carlos Marcos for his constant aid with the electronic issues and his

availability. I have no words to thank him. Carmen Vázquez and Jose Luis Nombela of the Electronic Technology Department also deserve my thanks. Last chapters of these thesis would not have been possible without their collaboration with the optical probes. Pepe Sicre, from the Material Sciences Department, kindly helped me with the particle analysis and I am really grateful to him.

I would like to thank my colleagues of the running club of my University for all the relaxing and fun runs we did together. It was really helpful to cope with the long days of work.

I wish to thank Naoko Ellis from the University of British Columbia who host me during two summer research stays. She was a source of knowledge and knowhow. I also learn a lot from Ana Stefanova, who helped me with the experimental work in the circulating fluidized bed at UBC.

I am grateful to Jose for his help with the bibliography and his patience during the last months.

Abstract

This thesis presents the experimental fluid dynamic characterization of a new fluidized bed with a rotating distributor.

Many works in the literature analyze the factors that influence the quality of fluidization in bubbling beds, e.g. the rate of solids mixing, the size of the bubbles and the extent of heterogeneity in the bed. These factors include among other, the bed geometry, the gas flow rate and the type of gas distributor. The non heterogenous structures often found in industrial fluidization processes have led many investigators to modify the conventional fluidized bed devices, alter the air supply system or try innovative designs to avoid these heterogeneities. The novel distributor design studied in this thesis tries to solve some of these difficulties; the aim of the distributor rotation being to overcome low radial gas mixing and particle dispersion, and to achieve a more uniform fluidization. The possibility to control and adjust the rotational speed of the distributor plate offers a wide range of operating conditions while maintaining the quality of fluidization.

The fluidized bed is a transparent cylinder with 192 mm ID and a height of 0.8 m filled with Geldart B silica particles. The distributor is a perforated plate that is coupled to the shaft of an AC electric motor. It can rotates around the bed axis and the rotational speed can be varied using a frequency inverter. In the experiments this speed was varied between 0 and 100 rpm. A complete description of the experimental set-up can be found in Chapter 2.

The experimental fluid dynamic characterization presented in this thesis includes a global description of the bed behavior with and without rotation of the distributor, using pressure measurements (Chapter 4). In addition, the differences in the characteristics of the generated bubbles are studied by means of in house made optical probes (Chapter 6).

To better understand the pressure signal recorded for the bed characterization, the behavior of the standard deviation of pressure fluctuations in fluidized beds for group B particles in the bubbling regime is studied in Chapter 3. An empirical-theoretical function, which depends on the gas velocity, is proposed for predicting the pressure signal

fluctuations. The differences in the standard deviation of pressure fluctuations obtained from absolute or differential sensors are analyzed and compared to experimental values corresponding to different bed sizes, pressure probe positions and particle properties.
In chapter 4 the effect of the rotational speed of the distributor plate on the global hydrodynamic behavior of the bed is studied. Minimum fluidization velocity and pressure fluctuations were first analyzed. A decrease in the minimum fluidization velocity is observed when the rotational speed increases. The standard deviation and the power spectra of the pressure fluctuations are also discussed. Measurements with several initial static bed heights were taken in order to analyze the influence of the initial bed mass inventory over the effect of the distributor rotation on the bed hydrodynamics. The rotation of the distributor allows to fluidize very shallow beds which had a jet structure when the static distributor is used; the effect of the rotation becomes globally less important for deeper beds.
These characteristics show that adjusting the rotational speed it is possible to change the gas velocity needed to fluidize the bed, facilitating the fluidization and maintaining a uniform fluidization.
Once the global fluid dynamic behavior is known, local characteristics are analyzed. Differential pressure and optical probe measurements were carried out in order to obtain the size and velocity of the bubbles rising in the bed. Results obtained from the two types of probes were compared in Chapter 5. The probability distributions of bubble pierced length and velocity were obtained applying the Maximum Entropy Method. The minimum bubble pierced length that it is possible to measure using intrusive probes, due to their finite size, has been introduced as a constraint in the derivation of the size distribution equations. The probability density function of bubble diameter was inferred applying statistical tools to the pierced length experimental data. Results on bubble size obtained from pressure and optical probes have been found to be very similar, although optical probes provide more local measurements and can be used even at very low heights in the bed, near the distributor. The Maximum Entropy Method has been found to be a simple method that offers many advantages over other methods applied before for size distribution modeling in fluidized beds: the distribution shape does not have to be pre-established, the number of samples required is lower than in other methods and the backward transformation procedure is avoided.
The effect of the distributor rotation on the bubble size, bubble passage frequency and bubbles distribution at different radial and axial positions in the bed was studied with the optical probes and the results are presented in Chapter 6. A simple theoretical expression

is obtained in order to analyze the centrifugal acceleration influence on the bubble when it detaches from the distributor. This analysis points out that the centrifugal acceleration imparted by the distributor rotation causes the decrease of the initial bubble radius. The experimental results show that the bubbles are smaller when the rotating distributor is used if the excess gas for the static and rotating configuration is similar. The bubble size radial profile indicates that when the distributor rotates, the diameter of the bubbles close to the bed walls is smaller due to the effect of a higher centrifugal acceleration. The distributor rotation also promotes the more homogenous distribution of the bubbles over the bed surface. At higher axial positions even smaller bubbles are found for the rotating case. This may be due to a lower coalescence rate of the bubbles when the distributor rotates as the rotation may break the channeling in the bed.

Some of the results presented in this thesis have been published in:

Sobrino, C., Almedros-Ibáñez, J. A., Santana, D., de Vega, M., 2008. Fluidization of group B particles with a rotating distributor. Powder Technology 181, 273-280.

Sobrino, C., Almedros-Ibáñez, J. A., Sánchez-Delgado, S., de Vega, M., Santana, D., Ruiz-Rivas., U., 2007. Hydrodynamic characterization of a fluidized bed with rotating distributor. In: Bi, X., Berruti, F., Pugsley, T. (Eds.), Fluidization XII. pp 767-774.

and presented in:

Vázquez, C., Nombela, J. L., Sobrino, C., de Vega, M., Zubía, J. and Montero, D. S. M., 2007. Plastic fiber-optic probes for characterizing fluidized beds in bubbling regime. 16th International Conference on Plastic Optical Fiber (POF).

Resumen

Esta tesis consiste en la caracterización experimental de la hidrodinámica de un nuevo lecho fluido de distribuidor rotatorio.
Existen numerosas referencias en la literatura en las que se analizan los factores que influyen en la calidad de la fluidización en lechos burbujeantes, como son la tasa de mezcla, el tamaño de burbuja y la heterogeneidad en el lecho. Entre estos factores se encuentran la geometría del lecho, el caudal de gas empleado en la fluidización y el tipo de distribuidor. Las heterogeneidades que se producen con frecuencia en lechos industriales han hecho que numerosos investigadores hayan incorporado modificaciones de distinta índole sobre los lechos convencionales, como por ejemplo alterar el sistema de suministro de aire o usar diseños innovadores. El nuevo diseño de distribuidor que se estudia en esta tesis intenta, mediante la introducción del giro del distribuidor, lograr mayores tasas de mezcla del gas y aumentar la dispersión de las partículas, al tiempo que se consigue una fluidización más uniforme. La posibilidad de controlar la velocidad de giro del distribuidor permite operar en un amplio rango de condiciones de operación sin perder la calidad de fluidización.
Los experimentos fueron realizados en un lecho constituido por un cilindro transparente de diámetro 192 mm y altura 0.8 m lleno de partículas de arena del tipo B de acuerdo con la clasificación de Geldart. El distribuidor rotatorio es una placa perforada acoplada en su eje al eje de un motor eléctrico. La velocidad de giro se controla mediante un inversor de frecuencia que permite trabajar con un rango de velocidades que en los experimentos se varía de 0 a 100 rpm. La descripción completa de la instalación experimental se encuentra en el Capítulo 2.
La caracterización experimental de la hidrodinámica del lecho realizada en la tesis incluye, por un lado, la descripción global del lecho sin giro y con giro en el distribuidor, mediante medidas absolutas de presión (Capítulo 4) y por otro, el estudio de las propiedades de las burbujas que se forman en el lecho usando sondas ópticas específicamente diseñadas y construidas para esta tesis (Capítulo 6).
Con el fin de interpretar de manera adecuada las señales de presión que se utilizan para la

caracterización del lecho, el Capítulo 3 contiene un estudio de los valores de la desviación estándar de las señales de presión en lechos fluidos burbujeantes. Se ha obtenido una función semi-empírica, que depende de la velocidad del gas, que permite predecir dichas fluctuaciones de presión en lechos con partículas del tipo B. Este modelo permite explicar las diferencias en las medidas cuando se emplean sensores de presión en modo diferencial o absoluto, obteniéndose una buena correspondencia entre los valores teóricos y las medidas experimentales para diferentes tamaños de lechos, posición de los sensores y propiedades de las partículas.

En el Capítulo 4 se estudia el efecto del giro del distribuidor en el comportamiento hidrodinámico global del lecho, analizándose el cambio en la mínima velocidad de fluidización y en las fluctuaciones de presión. Se ha observado una disminución en el valor de la mínima velocidad de fluidización a medida que aumenta la velocidad de giro. Además se analizaron los espectros de frecuencia y la desviación estándar de las fluctuaciones de presión. Las medidas se repitieron a distintas alturas iniciales del lecho para ver como afectaba esta altura a la magnitud del efecto provocado por el giro. Se ha comprobado que la rotación del distribuidor permite fluidizar lechos con poca altura, que en ausencia de giro presentan una estructura de chorros y no se consiguen fluidizar. Por otro lado, conforme aumenta la altura inicial del lecho, el efecto de la rotación sobre la velocidad de mínima fluidización tiende a disminuir. Se demuestra por tanto que mediante el ajuste de la velocidad de giro en el distribuidor, se puede cambiar la velocidad del aire necesario para fluidizar el lecho, lo que permite mantener unas condiciones uniformes de fluidización en un rango mayor de caudales.

Una vez realizado el análisis global, se estudiaron las características locales del lecho. Para ello, se usaron sensores de presión diferencial y sondas ópticas con las que se midieron las cuerdas de las burbujas que se forman en el lecho y su velocidad. Los resultados obtenidos usando las dos sondas se encuentran en el Capítulo 5. Las funciones de densidad de probabilidad de la cuerda y de la velocidad se calcularon aplicando el Método de la Máxima Entropía. Existe un tamaño mínimo de cuerda que es posible medir usando sondas intrusivas para que el error sea tolerable. Este límite inferior se ha tenido en cuenta en la formulación de las ecuaciones para la obtención de las funciones de distribución de probabilidad. La función de densidad de probabilidad de los diámetros se ha deducido a partir de las medidas experimentales de las cuerdas, aplicando herramientas estadísticas. Los resultados de las sondas de presión y de las sondas ópticas son bastante parecidos, aunque las sondas ópticas proporcionan información más local, y pueden utilizarse en posiciones muy próximas al distribuidor. Se ha comprobado que el método de la Máxima Entropía

es un método simple que ofrece varias ventajas frente a otros métodos aplicados hasta la fecha para la obtención de las distribuciones de tamaño en lechos fluidos: no es necesario suponer a priori la forma de la distribución, el número de muestras requeridas es menor que en otros métodos y se evita la transformación inversa, que es un cálculo complejo.
Una vez desarrollado y validado el método de transformación de cuerdas en diámetros se estudió el efecto del giro del distribuidor en el tamaño de las burbujas y su frecuencia de paso a distintas posiciones en el lecho. Los resultados se presentan en el capítulo 6. Primero se ha obtenido un modelo simple para analizar la influencia de la aceleración centrifuga que actúa sobre la burbuja en el momento en que se desprende del distribuidor una vez formada. Este análisis indica que el giro hace que el diámetro inicial de la burbuja sea menor que si el distribuidor estuviera parado. Los resultados experimentales muestran que, a igualdad en el exceso de aire, el tamaño de las burbujas es menor cuando el distribuidor gira. Los tamaños medidos de burbuja en distintas posiciones radiales confirman la tendencia puesta de manifiesto por el modelo: para el distribuidor rotatorio el diámetro medio disminuye a distancias mayores del eje del lecho, donde la aceleración centrífuga es mayor. La rotación del distribuidor también hace que la distribución de burbujas en la sección radial del lecho sea más homogénea. Además, para el distribuidor rotatorio se observa que el aumento del tamaño de las burbujas a medida que aumenta la altura es menos acusado que con ausencia de giro. Esto puede deberse a una disminución de la coalescencia lograda por la ruptura de los caminos preferenciales de ascensión de las burbujas gracias al giro.

Algunos de los resultados presentados en la tesis han sido publicados en:

Sobrino, C., Almedros-Ibáñez, J. A., Santana, D., de Vega, M., 2008. Fluidization of group B particles with a rotating distributor. Powder Technology 181, 273-280.

Sobrino, C., Almedros-Ibáñez, J. A., Sánchez-Delgado, S., de Vega, M., Santana, D., Ruiz-Rivas., U., 2007. Hydrodynamic characterization of a fluidized bed with rotating distributor. In: Bi, X., Berruti, F., Pugsley, T. (Eds.), Fluidization XII. pp 767-774.

y presentados en:

Vázquez, C., Nombela, J. L., Sobrino, C., de Vega, M., Zubía, J. and Montero, D. S. M., 2007. Plastic fiber-optic probes for characterizing fluidized beds in bubbling regime. 16th

International Conference on Plastic Optical Fiber (POF).

Contents

List of Figures

List of Tables

Nomenclature

a	Coefficient in Eq. (1.7) and (5.38) $(-)$
A	Amplitude of pressure fluctuation (Pa)
	Cross-sectional area of the bed (m^2)
A_o	Distributor area per number of holes (m^2)
Ar	$\rho_f(\rho_p - \rho_f)d_p^3\mu_f^2/g$ Archimedes number $(-)$
b	Coefficient in Eq. (1.7) and (5.38) $(-)$
d_a	Sieve aperture (m)
d_p	Particle diameter based on screen analysis (m)
d_{pp}	Internal diameter of the pressure probe and line (m)
d_s	Surface diameter of the particle (m)
d_{sv}	Surface to volume diameter of the particles (m)
d_v	Volume equivalent diameter of the particles (m)
D	Bed diameter (m)
	Bubble diameter (m)
D_s	Diameter of the bubbles having $y > s$ (m)
D_v	Bubble volume equivalent diameter (m)

$D_{v,min}$	Lower limit of D_v distribution (m)
e_{u_b}	Relative error of the measured bubble velocity (m/s)
e_y	Relative error of the measured bubble pierced length (m)
f	Frequency (Hz)
	Function define in Eq. (5.26)
F	Probability function $(-)$
F_b	Buoyancy force (N)
F_c	Centrifugal Force (N)
g	Gravity acceleration (m/s^2)
	Gradient vector defined in Eq. (5.33)
G	Potential function defined in Eq. (5.32)
h	Generic function in Eq. (5.37)
H	Hessian matrix
i	Order of the sample raw moments
J	Pressure gradient at infinity (Pa/m)
L	Settled Bed height (m)
L_{mf}	Bed height at minimum fluidization (m)
L_{pp}	Length of the pressure probe and line (m)
n	Rotational speed of the distributor plate (rpm)
N_o	Number of orifices in distributor plate $(-)$
op	Optical probe signal (V)

p	Gauge pressure (Pa)
p_b	Fluctuating component of absolute pressure due to bubble passage (Pa)
p_{dif}	Differential pressure (Pa)
p_f	pressure within fluidizing fluid (Pa)
p_{fluc}	Fluctuating component of absolute pressure (Pa)
p_h	Hydrostatic pressure (Pa)
p_{signal}	Pressure signal (Pa)
p_w	Fluctuating component of absolute pressure due to pressure waves (Pa)
P	Probability density function $(-)$
P_s	Probability density function of the bubbles with $y > s$ $(-)$
q	Volumetric flow rate through a hole of the distributor (m^3/s)
Q	Bubble geometry factor $(-)$
r	Radial coordinate
	Distance between the probe and the bubble symmetry axis (m)
r_b	Bubble radius (m)
$r_{max,s}$	Maximum distance between the probe and the bubble symmetry axis for bubbles with $y > s$ (m)
R	Bed radius (m)
R_m	Average radius of the distributor plate (m)
Re	$Ud_p\rho_f/\mu_f$ Reynolds number $(-)$
Re_{mf}	$U_{mf}d_p\rho_f/\mu_f$ Reynolds number at minimum fluidization $(-)$

s	Distance between the lower and the upper probes (m)
s_{ports}	Distance between probe ports (m)
S	Parameter defined in Eq. (5.19)
t	Time (s)
t_1	Time at which the bubble nose reach the lower pressure probe (s)
t_2	Time at which the bubble nose reach the upper lower pressure probe (s)
t_u	Time lag between the signals measured by the lower and the upper probes (s)
t_y	Time period $\approx y/u_b$ (s)
u_b	Vertical velocity of bubbles (m/s)
u_o	Vertical velocity of the bubble center (m/s)
U	Superficial gas velocity (m/s)
U_{mb}	Minimum bubbling velocity (m/s)
U_{mf}	Minimum fluidization velocity (m/s)
$U_{mf,0}$	Minimum fluidization velocity for the static distributor plate (m/s)
$U_{mf,100}$	Minimum fluidization velocity for the distributor plate rotating at 100 rpm (m/s)
V	Bubble volume (m^3)
V_d	Dead volume of the pressure probe (m^3)
V_v	Volume of a sphere having the same diameter as the bubble (m^3)
w	Gauss-Legendre weights
x	Generic variable in Eq. (5.5)
y	Bubble pierced length (m)

z	Height above the distributor (m)
z_{op}	Axial position of the optical probe (m)
z_{pt}	Axial position of the pressure probe (m)
α_1	Bubble geometry factor $(-)$
α_2	Bubble geometry factor $(-)$
δ	Ratio of the bubble diameter to the diameter of a sphere of the same volume D_v/D $(-)$
Δ	Integration domain $(-)$
Δ_{KL}	Kullback-Leibler discrepancy
Δp	Pressure drop across the bed (Pa)
Δt	Time between samples (s)
Δu_b	Error of the measured bubble velocity (m/s)
Δy	Error of the measured bubble pierced length (m)
ϵ	Voidage $(-)$
ϵ_{mf}	Value of voidage at minimum fluidization $(-)$
θ	Angular coordinate (rad)
λ	Lagrangian multiplier
μ_f	Viscosity of fluid $(kg/(m \cdot s))$
ξ	Variable in Eq. (5.38)
ρ	Ratio of the volume of the bubble to the volume of a sphere with the same diameter V/V_v $(-)$
ρ_{bulk}	Density of particle phase $= [\rho_p(1-\epsilon) + \rho_f\epsilon]$ (kg/m^3)

ρ_f	Density of fluidizing fluid (kg/m^3)
ρ_p	Particle density (kg/m^3)
σ_p	Standard deviation of pressure fluctuations (Pa)
τ_{pp}	Response time of the pressure probe (s)
ϕ	Factor in Eq. (5.29) (m^{-1})
ϕ_s	Particle sphericity $(-)$
$\omega = \frac{2\pi n}{60}$	Angular velocity of the distributor plate (s^{-1})

Subindex

1	Lower measuring probe
2	Upper measuring probe

Chapter 1

Introduction

Davidson and Harrison (1963) described the phenomenon of fluidization in terms of a simple experiment in which a bed of solid particles is supported on a horizontal gauze in a vertical tube. Gas or liquid is then forced to flow upwards through the gauze, and so through the particle bed. This flow causes a pressure drop across the bed, and when this pressure drop is sufficient to support the weight of the particles the bed is said to be incipiently fluidized (at minimum fluidization). The fluidized bed thus formed looks very much as a liquid; its upper surface remains horizontal when the containing apparatus is tilted, light objects float on its surface, solids will gush in a jet from a hole in the side of the container and when two beds are connected their levels equalize.

In gas-solid systems an increase in gas flow rate above that of minimum fluidization, results in the formation of bubbles or channels. In this regime referred as bubbling fluidization there is a fairly clearly defined upper surface. However, at a sufficiently high fluid flow rate the terminal velocity of the solids is exceeded, the upper surface of the bed disappears, entrainment becomes appreciable, and solids are carried out of the bed with the fluid stream.

Fluidized systems have a number of advantages regarding temperature control and heat transfer. The same temperature is quickly established throughout the system because the general agitation of the particles disperses local regions of hot or cold. There is also a high rate of heat transfer to a solid object placed in the bed. Another useful property is the ease of the solid particles handling, as they behave as a liquid, what allows the continuous operation of the system. Fluidization is also an excellent way of bringing a gas into contact with a solid, and therefore catalytic reactions are often well suited to the technique.

Nevertheless fluidized beds show also a number of disadvantages. The bubbles of gas

present in gas-solids beds can cause both chemical and mechanical difficulties. For instance the bypassing of solids by bubbles lowers the gas-solids contact and the efficiency in the conversion of gaseous reactant decreases. Also the pipes and vessels that are inside the fluidized bed reactor to recover the heat, suffer erosion due to the particle abrasion. The entrainment of solids is another difficulty since a system to replace the entrained solids is needed. Besides that, the quality of fluidization can vary enormously and situations with particles which do not flow freely or which agglomerate often occur.

Even if there are still some drawbacks, the main advantages described above make fluidized beds very suitable for many applications. These applications can be classified as (i) physical and mechanical processes (ii) chemical reactions and catalysis. Physical processes which use fluidized beds include drying, mixing, granulation, coating, heating and cooling. All these processes take advantage of the excellent mixing capabilities of fluidized beds. Good solids mixing gives rise to good heat transfer, temperature uniformity and ease of process control. The fluidized bed is also a good medium in which to carry out a chemical reaction involving a gas and a solid. The main reason for choosing the fluidized bed in preference to fixed bed for synthesis reactions (solid catalyzed gas phase reactions) is the demand for strict temperature control of the reaction zone, and the conditions in fluidized bed reactors are near isothermal. Practically all cracking and reforming of hydrocarbons processes are done in pneumatic solids circulation systems employing one or more fluidized beds.

Fuel conversion applications are nowadays one of the hot topics in fluidized beds technology. The principle of Fluidized Bed Combustion (FBC) technology is a fluidized bed of inert solids (e.g. sand or ash) which during start up, is first heated up by start-up burners with oil or gas and when a high enough temperature has been reached (at least 600 °C) solid fuel can be added to the bed and after it ignites, the start-up firing can be shut-down. The combustion of the solid fuel can be maintained at a temperature of about 850 °C which yield low NO_x emissions. In order to maintain the combustion temperatures, the heat balance of the bed is controlled by cooling tubes typically located at the furnace walls (hence the name boiler). FBC is today a well established technology for generation of heat, power and a combination of these. The main advantage of FBC is the fuel flexibility. Commercial fluidized bed boilers are operating today around the world for burning not only coal but also biomass and waste derived fuels or cofiring of coal and biomass (Johnsson, 2007). Other new applications of FBC are CO_2 Capture and Storage that is developed by two processes, the oxyfuel combustion, where the fuel is combusted in a mixture of pure oxygen and recycled flue gas, and the chemical looping combustion,

where metal oxide particles are used to transfer oxygen from air to a gaseous fuel. Gasification using fluidized bed technology in the energy sector (for production of clean gases such as to be used as transportation fuel and for high efficient gas turbine power generation) is still at an early stage of development, although gasification itself is well proven.

1.1 Motivation of the thesis

This thesis presents the fluid dynamic characterization of a new fluidized bed with a rotating distributor working at cold conditions. This novel distributor tries to solve some of the difficulties described above, that are often found in fluidization processes.
The main results show that the novel design promotes the bubble size decrease and helps to make the fluidization smoother and more homogenous. Many investigators have tried also to enhance the fluidization quality by modifying the conventional fluidized bed devices, altering the air supply system or trying innovative designs. Many of these attempts are reviewed in this thesis. The distributor employed in this work, was designed to be used in a biomass gasifier and the results presented in this thesis, obtained in the cold model are expected to give reliable improvements in the hot application leading to a higher gas conversion rate and a higher heating value of the product gas.

1.2 Some basic principles of fluidization

The superficial gas velocity at which the packed bed becomes a fluidized bed is known as the minimum fluidization velocity, U_{mf}. For gas-solid systems, especially when relatively coarse solid particles are used, fluid velocity increment beyond U_{mf} is accompanied by the formation of rising bubbles or voids with hardly any solids particles inside them. According to the theory of the two-phases the gas flow beyond that of minimum fluidization (excess gas) goes through the bed in the form of bubbles, thus implying that gas velocity through the surrounding dense continuous phase remains essentially at the value of U_{mf}. This regime is referred as bubbling fluidization and experiments carried out in this thesis were conducted under these conditions. If the gas velocity is higher increased, it is possible to alter the shape of the bubbles so much, especially with recycling of solids from the top to the bottom of the fluidized bed. In this way, a new two phase structure with strands or clusters of solids, appears as a discontinuous phase dispersed in a dilute continuous phase

of a population of sparse solid particles. The new high velocity phenomenon, realizable only with suitable solid materials, is associated with the mode of gas-solid contacting called circulating fluidized bed or fast fluidization (Kwauk and Li, 1996).
The ease with which particles fluidize and the range of operating conditions which sustain fluidization varies greatly depending on the particle properties.
Geldart (1973) classified powders into four groups according to their gas-fluidization properties. The Geldart's classification of powders is widely used in many fields of powder technology. Powders in group A exhibit dense phase expansion after minimum fluidization and prior to the beginning of bubbling; those in group B bubble at the minimum fluidization velocity; those in group C are very fine and cohesive powders that are difficult to fluidize at all and those in group D are very large particles that can form stable spouted beds. Fig. 1.1 shows how the group classification are related to the particle and gas properties.
Since the range of gas velocities over which non-bubbling fluidization occurs for Group A powders is small, bubbling fluidization is the most commonly type encountered in gas fluidized systems in commercial use. The superficial gas velocity at which bubbles first appear is known as the minimum bubbling velocity U_{mb}. For Geldart B and D particles this velocity coincides with U_{mf} and it is quite similar for Geldart A particles. In group C particles, bubbles as such do not appear; instead, the gas flow forms channels through the particles. Fluidization, of sorts, can be achieved with the assistance of a mechanical stirrer or vibration. When the size of bubbles is greater than about one third of the bed diameter, they become slugs of gas. Slugging is unlikely to occur at any velocity if the bed is sufficiently shallow.
This description of fluidized bed indicates that there are two important aspects that need to be understood in depth when a particular fluidization process is studied: the minimum fluidization velocity, which is also crucial in the defluidization detection, and the characteristics of the bubbles rising in the bed.
When a bed filled with particles of density ρ_p is fluidized with a flow of gas of density ρ_f, at minimum fluidization conditions, the pressure drop, Δp, is enough to support the weight of the particles in unit cross-section, and therefore

$$\frac{\Delta p}{L_{mf}} = (\rho_p - \rho_f) g (1 - \epsilon_{mf}) \tag{1.1}$$

ϵ_{mf} is the voidage or volume fraction occupied by the fluid at minimum fluidization velocity and L_{mf} is the height of the bed at this condition.

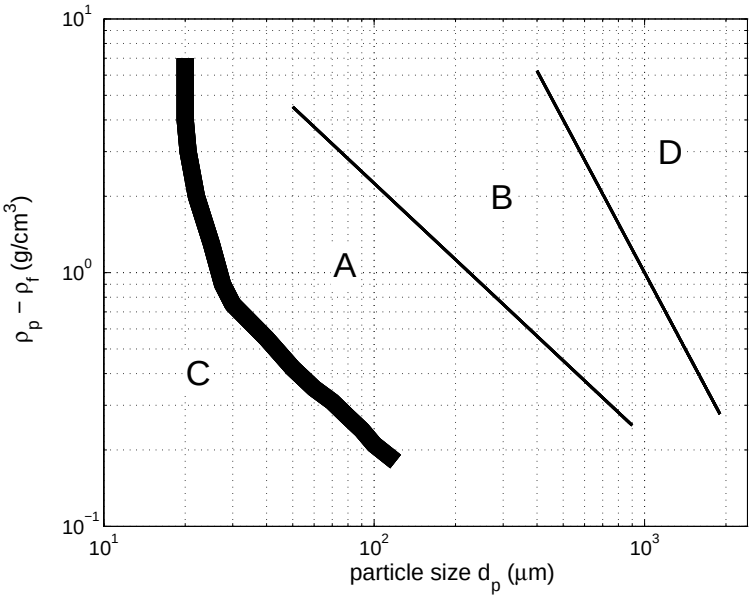

Figure 1.1: Geldarts classification of powders.

The particle density, that is used in fluidization equations is defined as the mass of a particle divided by its hydrodynamic volume. This is the volume "seen" by the fluid in the interactions with the particles and it includes the volume of the open and closed pores. For non-porous solids this density is the same as the absolute or true density, ρ_p, which is the mass of the particle divided by the volume of solid material making up the particle. The bulk density of particle phase or bed density, ρ_{bulk}, is defined as the mass of particles in the bed divided by the volume occupied by the particles and the voids between them:

$$\rho_{bulk} = \rho_p(1-\epsilon) + \rho_f\epsilon \tag{1.2}$$

The gas density is much smaller than the particles density and hence the term $\rho_f\epsilon$ can be neglected.

The pressure drop Δp across a fixed bed of particles when a gas passes through it with a velocity U has been correlated by Ergun (1952),

$$\frac{\Delta p}{L} = 150\frac{(1-\epsilon)^2}{\epsilon^3}\frac{\mu_f U}{(\phi_s d_p)^2} + 1.75\frac{1-\epsilon}{\epsilon^3}\frac{\rho_f U^2}{\phi_s d_p} \tag{1.3}$$

where d_p is the diameter of a sphere having the same volume of the particle and ϕ_s is the sphericity, which is the relation between the surface of a sphere and the surface of a particle both having the same volume. μ_f is the viscosity of the gas, L the height of the bed of particles and ϵ the voidage. The first term of Eq. (1.3) predominates at

low Reynolds numbers. At high Reynolds number the second term predominates and it represents the drag on the individual particles. The two terms thus represent the effect of viscous and inertia forces respectively.
The minimum fluidization velocity can be obtain from Eq. (1.1) and (1.3), evaluating Eq. (1.3) at minimum fluidization conditions. Doing this the following expression is obtained:

$$Ar = 150\frac{1-\epsilon}{\epsilon^3}Re_{mf} + 1.75\frac{1}{\epsilon^3}Re_{mf}^2 \tag{1.4}$$

where Ar is the Archimedes number and Re_{mf} is the Reynolds number at minimum fluidization,

$$Ar = \frac{\rho_f(\rho_p - \rho_f)}{g}d_p^3\mu_f^2 \tag{1.5}$$

$$Re_{mf} = \frac{U_{mf}d_p\rho_f}{\mu_f} \tag{1.6}$$

The main difficulty in predicting U_{mf} is to know the value of the void fraction at minimum fluidization. Taking ϵ_{mf} as the voidage of the packed bed, a crude U_{mf} is obtained. However the voidage at minimum fluidization is considerable greater than the packed bed voidage due to the bed expansion. A typical often used value of ϵ_{mf} is 0.45.
The minimum fluidization velocity can also be obtained experimentally. Fig. 1.2 is a typical plot of pressure drop for a bed of sand particles. For the relatively low flow rates in a packed bed the pressure drop is approximately proportional to gas velocity. The pressure drop at minimum fluidization conditions is that needed to support the weight of the particles, as expressed in Eq. (1.1). With gas velocities beyond minimum fluidization, the bed expand and bubbles start to rise in the bed. Despite this rise in gas flow, the pressure drop remains practically unchanged.
The minimum fluidization velocity, U_{mf}, is taken as the corresponding to the intersection of pressure drop lines for regime of developed fluidization and packed bed, respectively.
The shortcoming of the pressure drop method to evaluate U_{mf} is that two different sets of experimental data including the complex transition region are necessary to calculate U_{mf}. Moreover this method can not be used on line since it is necessary to defluidized the bed.
Puncochar et al. (1985) proposed another experimental method based on the pressure fluctuations measurement. They found out that the standard deviation of pressure fluc-

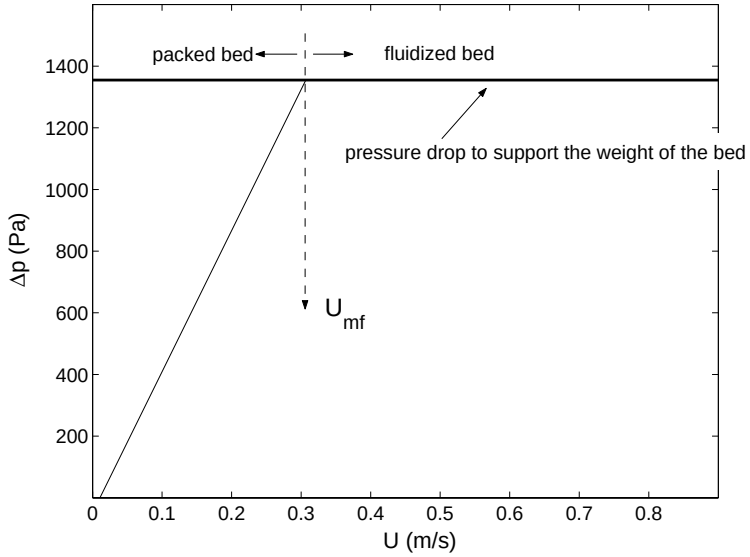

Figure 1.2: Pressure drop versus gas velocity for a bed of sand particles (adapted from Sobrino et al. (2008)).

tuations, σ_p was a practically linear function of the gas velocity, U:

$$\sigma_p = a + bU \tag{1.7}$$

where a and b can be determined by regression analysis.
Assuming that the pressure fluctuations in the bed arise at gas velocities higher than U_{mf}, this velocity is obtained as

$$U_{mf} = -\frac{a}{b} \tag{1.8}$$

The use of this method is illustrated in Fig. 1.3.
It was shown that in bubbling fluidized beds the gas bubble characteristics, i.e. gas bubble size and velocity, are important for the fluidized bed performance. On the one hand, gas bubbles promote the particle mixing, thus enhancing heat and mass transfer; on the other hand, the gaseous reactants in the gas bubbles barely touch catalysis particles or fuel and thus reactor efficiency decreases.
The gas bubble characteristics can be determined from the measurement of the pressure fluctuations caused by rising gas bubbles in fluidized beds.
Pressure measurements are widely applied in fluidized beds since they are cheap and relatively easy to perform. Time-averaged pressure measurements are used both in lab-scale setups and in commercial units. In fact, together with temperature measurements it is

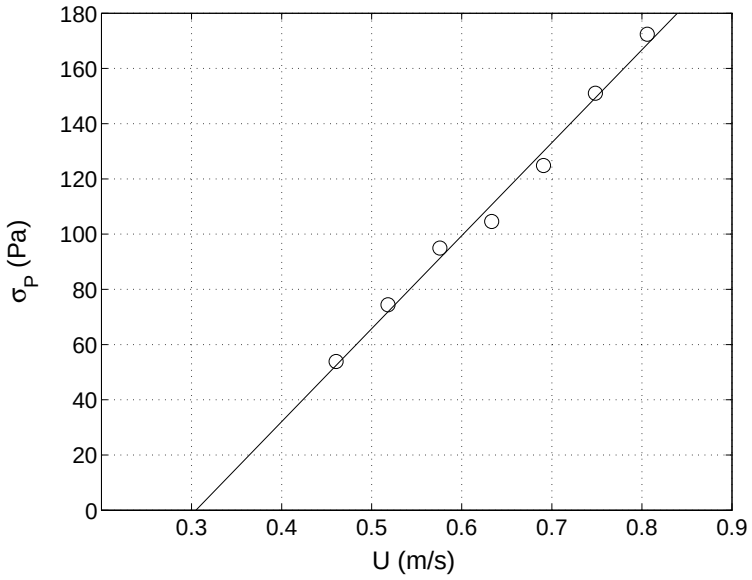

Figure 1.3: Standard deviation of pressure fluctuations versus gas velocity (adapted from Sobrino et al. (2008)).

the only measurement technique that is applied in industry on a routine basis (van Ommen and Mudde, 2007). When the pressure is sampled at a sufficiently high frequency, the pressure fluctuation signal obtained, can yield much more information on the bed fluid dynamics. Different analysis can be applied to the study of time-series of pressure fluctuations: interpretation of results in time domain, such as standard deviation, may sometimes lead to erroneous conclusions; the results from the frequency domain (power spectra) and state-space analysis (correlation dimension and Kolmogorov entropy together with a non-linearity test) are generally in agreement and should be used in addition to time domain analysis (Johnsson et al., 2000).

There are another techniques also applied to characterize gas-solid fluidized beds. The opaque nature of these beds make it quite difficult to obtain information about the particles and gas, either in the emulsion phase or in the form of bubbles inside the bed. Visual observation is only possible in very dilute systems, the outer layer or the free surface of the bed or 2-D beds. Another techniques as electric capacitance tomography, X-ray and gamma-ray tomography, optical or capacitance probes are also often applied.

When a gas bubble rising upward through the fluidized bed crosses the measurement position, a pressure fluctuation is generated with a characteristic shape described by the Davidson's model (Davidson and Harrison, 1963). Davidson and Harrison (1963) deduced a theory for describing the motion of fluid and particles in a fluidize bed at small Reynolds numbers ($Re = \rho_f U d_p / \mu_f$). The particulate phase is treated as an incompressible fluid

having the same bulk density as the whole bed at minimum fluidization. The fluidizing fluid is also assumed to be incompressible. The relative velocity between the fluidizing fluid and the particles is assumed to be proportional to the pressure gradient within the fluidizing fluid. The detailed derivation of the fluid motion can be found elsewhere (Davidson and Harrison, 1963), but it is noteworthy that the resulting equation for the pressure in the fluid is the Laplace's equation:

$$\nabla^2 p = 0 \tag{1.9}$$

The pressure distribution around a bubble within the fluidizing fluid must satisfy the above equation and the boundary condition far above and below the bubble that the pressure gradient shall have a constant value J.

$$p_f = -J\left(r - \frac{r_b^3}{r^2}\right) cos\theta \tag{1.10}$$

where the coordinates system is that of Fig. 1.4. The value of J is determined by the need to incipiently fluidized the particles, and J is the pressure gradient in a vertical direction such that the weight of the particles shall be just supported ($J = -\rho_{bulk} g$). The dense phase is assumed to be at minimum fluidization conditions and then $\rho_{bulk} = \rho_p(1 - \epsilon_{mf})$. The pressure around a rising bubble in an incipiently fluidized bed is represented in Fig. 1.5.

Coalescence of bubbles in fluidized beds leads to growth of bubble sizes with the distance to the distributor. Harrison and Leung (1961) concluded that bubbles may coalesce in a vertical line, i.e. one bubble may catch up another since when the following bubble approaches the leading bubble closely enough, it appears to be accelerated and gathered into the back of the leading bubble. This mode of coalescence may be explained by supposing that a wake behind a spherical-cap bubble, that carries solid particles, travels with the bubble. The following bubble may be elongated, and so loose its spherical-cap shape, as a consequence of its front taking up the wake velocity of a leading bubble before the rear. Harrison and Leung (1961)'s experiments showed that a velocity can be associated with the wake of the bubble. This velocity is sensibly constant (approximately equal to that of the bubble) over a distance of about a bubble diameter behind the bubble and beyond that the wake velocity falls off sharply. Afterwards Darton et al. (1977) modeled this phenomenon assuming that coalescence occurs between bubbles of neighboring streams and stated that except at the distributor plate, where bubbles formed in vertical alignment, this capture will generally involve an initial lateral movement.

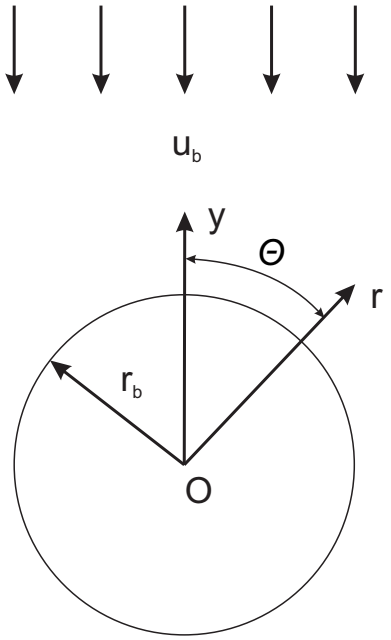

Figure 1.4: Coordinate system for a bubble in a fluidized bed, r being measured from the center of the bubble O.

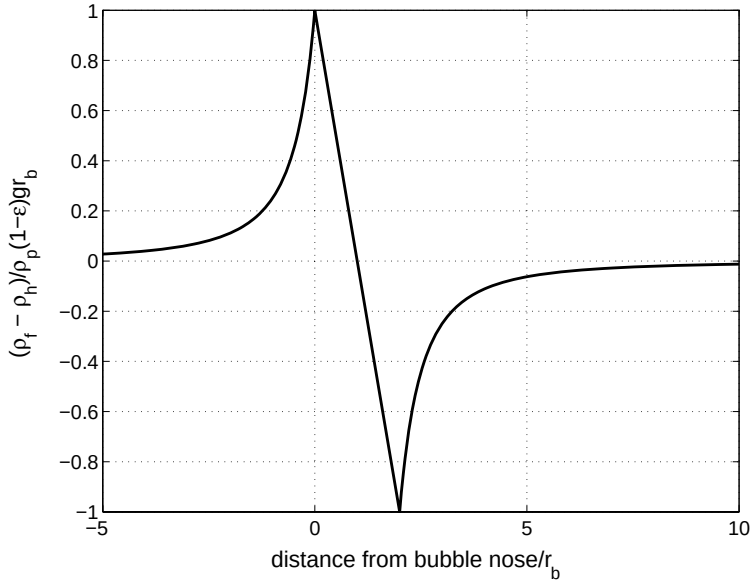

Figure 1.5: Pressure along the vertical axis of a rising bubble. p_h is the hydrostatic pressure at the measuring point $p_h = \rho_{bulk}(1-\epsilon)g(L-z)$.

The rising velocity of bubbles in fluidized beds is usually estimated following the semiempirical equation derived for large bubbles in liquids of low viscosity, where the effects of viscosity and surface tension are small (Davidson et al., 1977):

$$u_b = 0.71\sqrt{gD_v} \tag{1.11}$$

where D_v is the diameter of a sphere having the same volume as the bubble. This equation may be derived by considering potential flow around the nose of the bubble but the coefficient come from experiments with ordinary liquids like water.

1.3 Objectives of the thesis

The key objectives of this thesis are:

- Carry out a study on pressure fluctuations in fluidized beds in order to find out which are the parameters that affect pressure fluctuations and also distinguish between the phenomena captured by differential and absolute pressure measurements.
- Characterize the novel fluidized bed with rotating distributor from a global point of view and determine important parameters as the minimum fluidization velocity or the characteristic frequency and study the influence of the rotation on these parameters.
- Study the bubble characteristics in the bed and the influence of the rotation on these bubbles.

The development of an appropriate instrumentation and the use of a correct measurement method as well as the buildup of a procedure to carry out the signal processing is needed to achieve these targets successfully. Therefore it is needed to understand the nature of pressure measurements and also to develop probes capable to record the bubble passage in the bed and to derive a suitable method to determine the bubble parameters from the probe signals.

1.4 Thesis layout

An overall explanation of the experimental set up is included in **Chapter2**. A more detailed description on the used probes, the experimental method and the signal analysis

can be found in the experimental section of each chapter.

In **Chapter 3** a model to predict the standard deviation of pressure fluctuation is obtained. It is also explained which phenomena are captured either by differential or absolute pressures in a fluidized bed.

Chapter 4 shows the pressure drop in the bed, the minimum fluidization velocity and the frequency analysis of the pressure fluctuations. The effect of the distributor rotation on these results is studied. The results of this chapter have been published in Sobrino et al. (2007, 2008)

In **Chapter 5** pressure and optical probes are used to measure bubble characteristics in the bed. The signal processing is shown and a method to obtain the probability density function of the bubble velocity and bubble size is inferred. Some aspects of this chapter were presented in Vázquez et al. (2007)

In **Chapter 6** the method derived in Chapter 4 is used to obtain the bubble size in the bed at different radial and axial positions. The results for the distributor with and without rotation are compared.

Finally **Chapter 7** summarizes the conclusions of the previous chapters and suggests some future perspectives of this research.

Chapter 2

Experimental set-up

This chapter contains the description of the fluidized bed where the experiments were conducted. The different components of the measurements systems, details on the distributor design and a description of the particles is included. Specific aspects as the sensors description and details on the measurement method will be described in each chapter.

2.1 Experimental system

The experimental set-up consists of a fluidization column of 0.192 m i.d. and a height of 0.8 m. This column was filled up with silica particles and air was forced to flow upward through a perforated plate distributor and so through the particle bed. The fluidizing air was supplied by the building compressed air line at a pressure about 1 bar. The air flow rate was measured with a calibrated rotameter that could measure up to 1400 litre per minute. Pressure and optical probes were used in the study and the signals were logged into a computer via a 12 bits data acquisition board (ICP DAS PCI-1802H). A/D channels of the board were configured in single-ended mode. The data acquisition software was DasyLab.

2.2 Rotating system and distributors

The air distributor was a perforated plate with 2 mm diameter holes, giving a total open area ratio of 1%. The plate was covered with a fine-mesh net to prevent particles from falling down through the plate into the wind-box. The holes were laid out in a hexagonal pitch of 15 mm. An spiral pitch distributor with the same open area ratio was also tested.

An schematic of the holes lay out in the two different distributor designs is shown in Fig. 2.1.

The air distributor could rotate in the horizontal plane as it was coupled at the bed axis

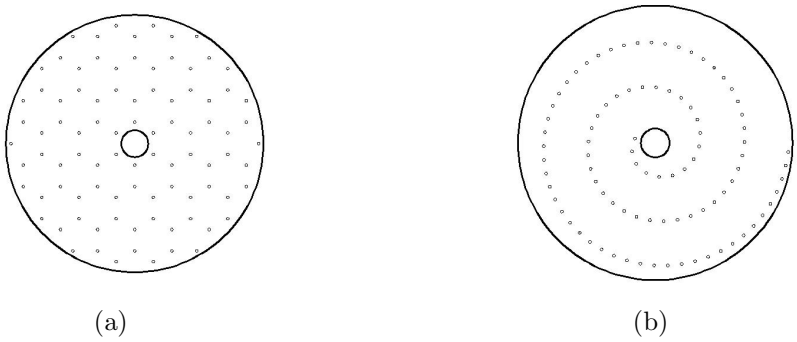

(a) (b)

Figure 2.1: (a) Uniform pitch distributor. (b) Spiral pitch distributor.

with the shaft of an AC electric motor with a 1:15 reducer. The rotational speed could be controlled using a frequency inverter and it ranged from 0 to 100 rpm. A detail of the mechanical assembly of the rotating distributor is shown in Fig. 2.2. The distributor was sandwiched with two flanges that were also machined in order to hold the tube containing the particles and the wind-box tube. Two screws in the distributor axis just rest above two holes in the structure axis which is inside the wind-box. A 3D schematic of the set-up can be seen in Fig. 2.3

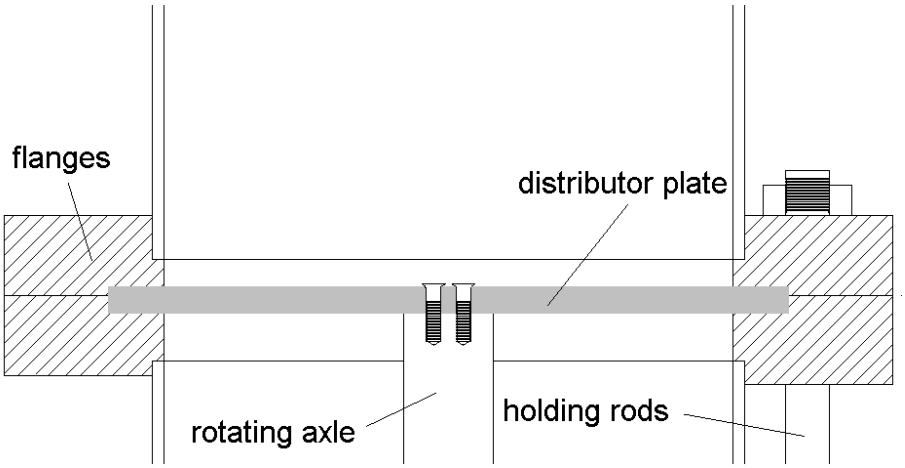

Figure 2.2: Mechanical assembly of the rotating distributor.

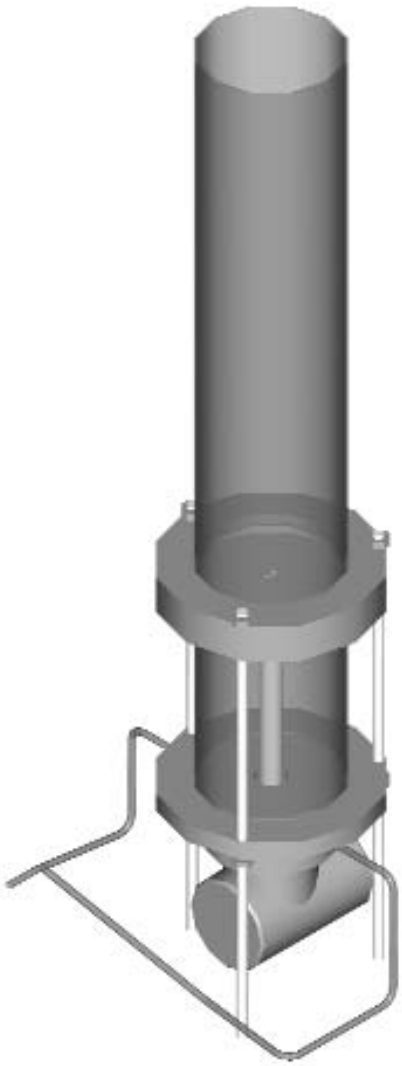

Figure 2.3: 3D schematic of the fluidized bed.

2.3 Distributor pressure drop

The distributor pressure drop at different gas velocities was measured with the empty bed for the static and the rotating distributor (Fig. 2.4). Several investigators (Karry and Werther, 2003) found that the ratio of the distributor to the bed pressure drop should be in the range of 0.015 to 0.4 to have a uniform distribution of the fluidizing gas. This criterium has been taken into account in the distributor design.

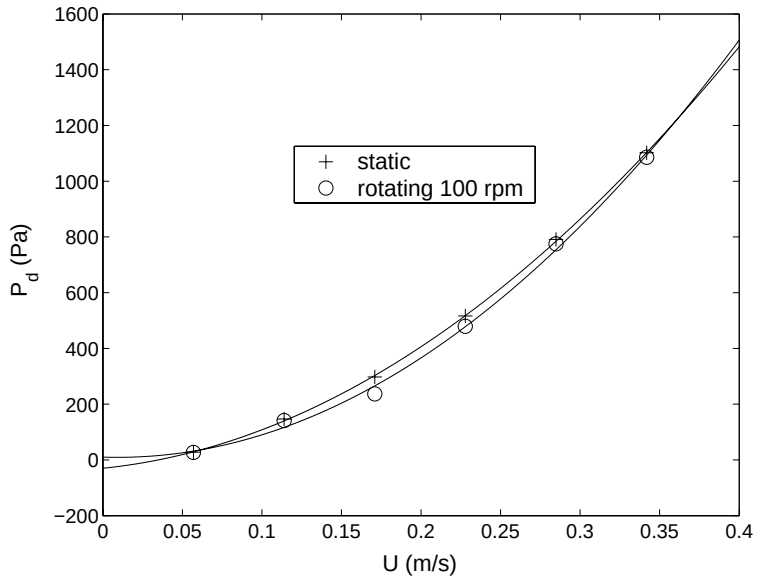

Figure 2.4: Distributor pressure drop against gas velocity for the static distributor and the distributor rotating at 100 rpm.

2.4 Particulate material

The solids used in this work were silica particles that can be classified as Group B according to Geldart's classification. An image of the particles used in the experiments is shown in Fig. 2.5.

It is important to obtain the size distribution, shape and density of the particles used in the fluidized bed. These parameters explicitly and implicitly will influence its behavior. For a particle of any shape, other than a sphere, there are many ways of defining its size, mainly d_v, d_{sv}, d_s and d_a, defined as follows,

- Volume diameter (d_v): the diameter of a sphere having the same volume as the particle.

- Surface to volume diameter (d_{sv}): the diameter of a sphere having the same surface/volume ratio as the particle.

- Surface diameter (d_s): the diameter of a sphere having the same surface as the particle.

- Sieve size (d_a): the width of the minimum square aperture through which the particles will pass.

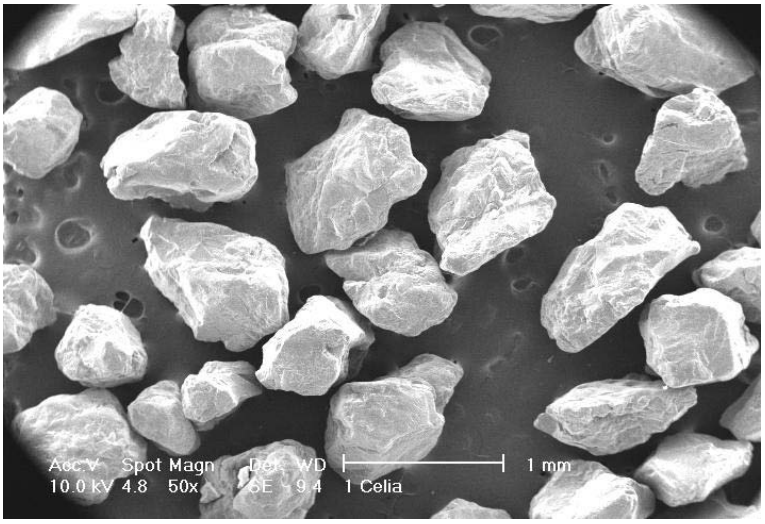

Figure 2.5: Microscopy of the sand used in the bed.

The sphericity ϕ_s is defined as

$$\phi_s = d_{sv}/d_v \tag{2.1}$$

d_v and d_{sv} can be calculated when particles have a regular shape. Nevertheless, in most of the cases, particles present irregular shapes and it is not so easy to characterize their sphericity. Typical values for sand are around 0.8-0.9.
The characteristic size of these non-spherical particles could be obtained in several ways. The size of larger particles ($>$ 1mm) can be found by direct measurement, if the particles are regular in shape. If this is not the case, their size can be inferred by weighing the solids if their density is known or by fluid displacement (Kunii and Levenspiel, 1991). Nevertheless, for intermediate particle sizes as it is the present case, sieve analysis is the most convenient way to measure particle size. The cumulative size distribution of the particles has been obtained as follows. A dry sample of 1570 g of sand is poured over a sieving column (Retsch AS 200). The column had 8 sieves, being the one with the larger opening size on the top of it. The column is mechanically vibrated and the particles retained in each sieve are weighted. The process is considered fully completed when the particles retained in a sieve does not change more than a 1% in a minute. The distribution of the mass fraction retained in the different screens is shown in Fig. 2.6.
It can be established that particles passing through a 250 μm mesh screen but resting on a 425 μm mesh screen have a sieve size d_p defined as the mean of both apertures. The size distribution of d_p calculated following this procedure is shown in Fig. 2.7. This

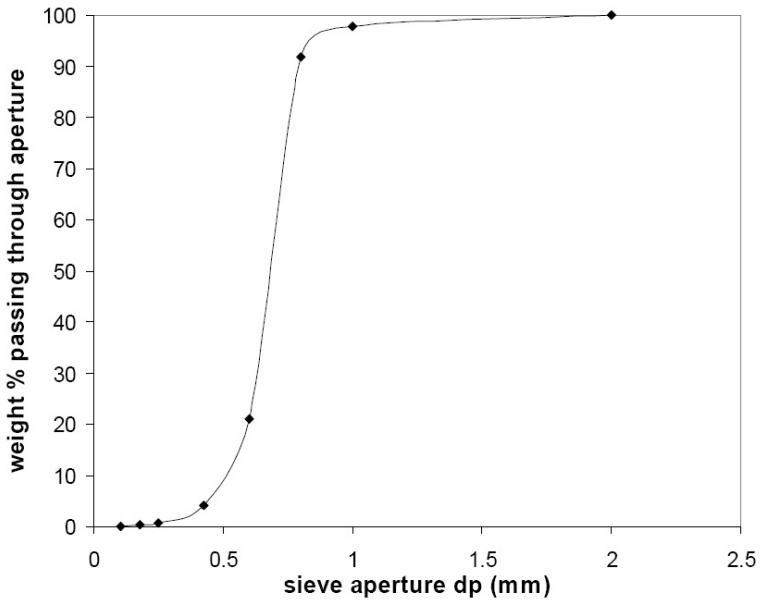

Figure 2.6: Cumulative distribution of the percentage of particles retained at a sieve aperture.

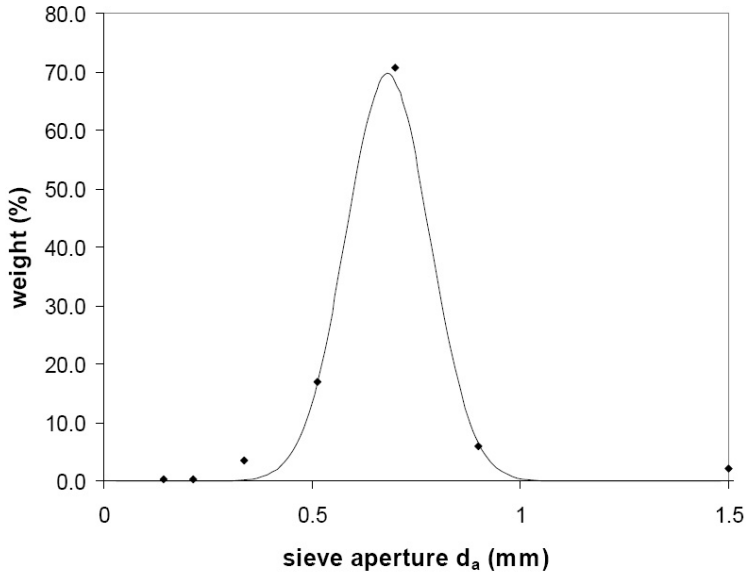

Figure 2.7: Probability density distribution of the percentage of particles retained at a sieve aperture. Solid line: normal distribution approximation.

distribution can be approximated to a normal distribution with a mean of 680 μm and a standard deviation of 100 μm.

There is no general relationship between the sieve size d_p and d_{sv} or d_v. Nevertheless, according to Kunii and Levenspiel (1991) and Geldart (1973), for irregular particles, with

no seemingly longer or shorter dimension (hence isotropic in shape), the following can be accepted:

$$d_{sv} = \phi_s \cdot d_v \approx \phi_s \cdot d_p \tag{2.2}$$

If this relationship is assumed and the sphericity factor is taken as 0.8, the d_{sv}=540 μm for the analyzed particles.
The particle density or true density of the solid material was measured using a pycnometer. The mean density was 2632.5 kg/m^3 with a standard deviation of 2.5 kg/m^3.

Chapter 3

Standard deviation of absolute and differential pressure fluctuations

This chapter describes the behavior of the standard deviation of pressure fluctuations, σ_p, in fluidized beds for group B particles in the bubbling regime. An empirical-theoretical function, which depends on the gas velocity, is proposed for predicting the pressure signal fluctuations, and the corresponding values of σ_p are calculated. The differences in the standard deviation of pressure fluctuations obtained for absolute or differential sensors are analyzed and compared to experimental values corresponding to different bed dimensions, pressure probe positions and particle properties.

3.1 Introduction

Knowledge of bed fluctuations in a gas-solids fluidized bed is important for its design and operation. Due to the ease of measurement and its significance in understanding dynamic behaviors, pressure time series and pressure fluctuations have been investigated by numerous researchers (Bi, 2007). It is accepted that the complex pressure signal is a result of the superposition of local fluctuations caused mainly by traveling gas bubbles and fast-traveling pressure waves arising due to bubble formation, coalescence and eruption. In order to characterize the hydrodynamics of the bed, statistical methods and spectral analysis have been used to identify these phenomena and to establish the different fluidization regimes (Lirag and Littman, 1971; Fan et al., 1981; Johnsson et al., 2000; van der Schaaf et al., 2002; Bai et al., 2005; Puncochar and Drahos, 2005). A simple statistical parameter, the standard deviation of pressure fluctuations, is commonly used to determine the minimum fluidization velocity (Puncochar et al., 1985; Wilkinson, 1995;

Felipe and Rocha, 2007). In spite of the measurement simplicity, the nature of pressure fluctuations in a fluidized bed is a complex function of particle properties, bed geometry, flow conditions, pressure and temperature. Fan et al. (1981) investigated the effect of particle size, static bed height and gas velocity. Svoboda et al. (1984) showed that the magnitude of the pressure fluctuations increases with both excess gas velocity and particle diameter. Svoboda et al. (1983) also reported that the amplitude of pressure fluctuations depends upon the height above the distributor. Pressure fluctuations can be very different at different locations on the axis of the bed (the region of bubble coalescence is displaced as the gas velocity increases) and thus the position at which pressure fluctuations are measured becomes an important factor in determining the relationship between the standard deviation of pressure fluctuations and the gas velocity. The effect of the probe location was studied by Hong et al. (1990) and Wilkinson (1995) for several particle sizes and static bed heights. The use of absolute or differential probes has also been discussed in order to elucidate wether or not they provide similar or different information: Roy and Davidson (1989) showed that single point pressure measurements were different from differential pressure measurements because the former included contributions from all sources while differential pressure mainly reflected pressure fluctuations across the measurement interval. The majority of the investigators agree upon the existence of a dominant frequency for the pressure fluctuations. This frequency has been shown to be related to the emergence of gas bubbles at the surface of the bed. Verloop and Heertjes (1974) reported that pressure fluctuations are similar to sinusoidal waves. Hiraoka et al. (1984, 1986) developed a dynamic model to predict the dominant frequency of bed fluctuations. Baskakov et al. (1986) and Alzahrani and Wali (1993) proposed correlations for predicting the amplitude and frequency of the pressure fluctuations. Chen and Bi (2003) developed a mechanistic model to simulate pressure fluctuations for group A particles with the aim of determining the transition to turbulent fluidization.

The aim of this chapter is to describe the behavior of the standard deviation of pressure fluctuations, σ_p , in fluidized beds for group B particles in the bubbling regime. A model for the pressure fluctuating signal is presented, taking into account the contribution of two different terms: the global absolute oscillation of the bed and the local passage of an ascending bubble. This simple model allows to understand the differences found between σ_p in absolute and differential pressure measurements. Results are analyzed and compared to experimental values, for different static bed heights, probe positions and particle properties.

3.2 Experiments

Pressure fluctuations are commonly measured with the use of sensitive pressure transducers connected to a pressure probe either flush with the inner wall of the column or immersed in the fluidized bed. However, the measurements can be difficult to interpret. Fan et al. (1981) proposed using single pressure transducers to describe fluidized beds while Bi et al. (1995) used several differential transducers to describe the nature of the bed. In this chapter, experimental measurements have been carried out in two different beds. The first test rig (rig A) is a transparent cylinder with 192 mm ID and a height of 0.8 m. The bed was filled with Geldart B silica particles with a mean diameter $d_p = 680$ μm and a density $\rho_p = 2632.5$ kg/m^3. The settled bed height was 20 cm. The pressure probes were mounted at the bed axis at 12 cm, 13 cm and 14 cm from the distributor plate. The pressure oscillations were measured with Omega PX piezoresistive differential pressure transmitters. The sensors were mounted on a 3 mm i.d. steel probe and silicone connecting tubing with a total length of about 2 m. The response time of the pressure probe can be calculated using the following expression (Xie and Geldart, 1997)

$$\tau_{pp} = \frac{128\mu_f L_{pp} V_d}{\pi p d_{pp}^4} \tag{3.1}$$

where μ_f is the gas viscosity, L_{pp} is the length of pressure probe and line, V_d is the dead volume, i.e. the volume between the probe tip and the transducer, d_{pp} is the internal diameter of pressure probe and line and p is the pressure that the probe is measuring. Applying this equation it can be seen that the response time is fast enough to measure the pressure fluctuations.

The data were recorded with a 12 bits data acquisition board (ICP DAS PCI 1802H) assembled in a PC. The sample frequency was 500Hz. Fig. 3.1 represents the corresponding absolute (Fig. 3.1(a)) and differential pressure (Fig. 3.1(b)) measured signals in the bubbling regime, at a superficial gas velocity U in excess of the minimum velocity U_{mf} equal to $U = 1.3U_{mf}$.

A second set of measurements have been taken in a second test rig (rig B) consisting of a cylinder of 300 mm ID bed, with pressure probes placed flush with the column wall at z = 8 cm, 11 cm and 15 cm. The bed was filled with silica sand and the settled bed height was 20 cm.

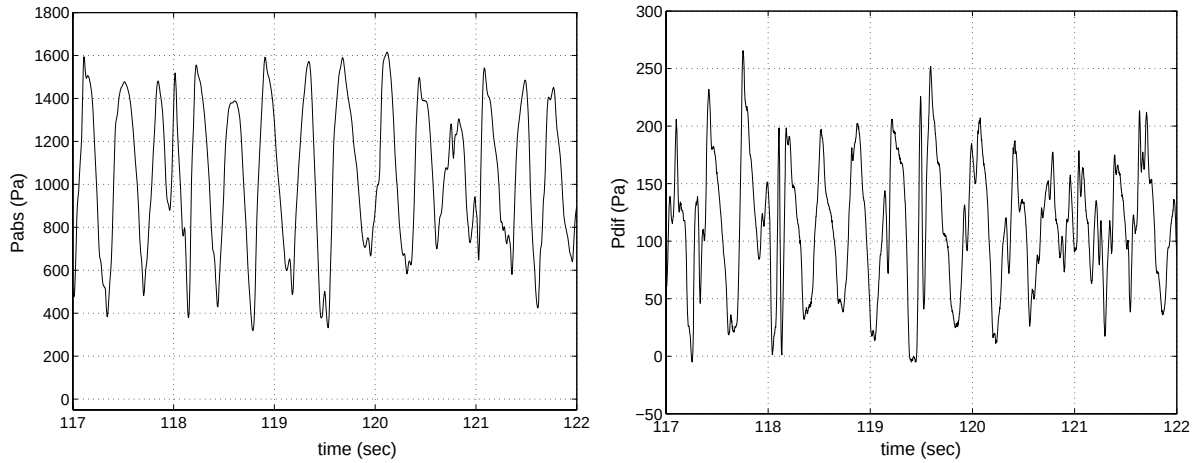

(a) (b)

Figure 3.1: (a) Absolute and (b) differential pressure signals measured in the rig A. $U/U_{mf} = 1.3$.

3.3 Model development

Pressure fluctuations in gas-solid bubbling fluidized beds are a consequence of different phenomena: rising gas bubbles, bed mass oscillation, bubble coalescence, bubble eruption and gas turbulence. van der Schaaf et al. (2002) proposed a way to decompose the power spectral density of the pressure fluctuations into a component corresponding to global phenomena (the coherent part of the pressure signal) and a component corresponding to local phenomena (the incoherent part of the pressure signal). They assumed that all pressure waves caused by bubble coalescence, gas flow fluctuations, bubble eruption and bed mass oscillation could be measured almost instantaneously throughout the entire bed and also in the plenum; bubbles were assumed to be the only local phenomenon. This is reasonable for small fluidized beds (diameters below 0.5 m).

When a gas bubble rising through the fluidized bed passes the measurement position a pressure fluctuation is generated with a characteristic shape. A model for the pressure fluctuation caused by a single rising bubble was proposed by Davidson and Harrison (1963). According to this model, the pressure distribution around a bubble of radius r_b relative to that in the dense phase (at a great distance above or below the bubble) can be written as (Ramaya et al., 1996):

$$p_b(t) = \rho_p g(1-\epsilon)\frac{r_b^3}{r^2}\cos\theta \qquad r > r_b \tag{3.2}$$

$$p_b(t) = \rho_p g(1-\epsilon) r\cos\theta \qquad r < r_b \tag{3.3}$$

with the origin of the polar coordinate system at the bubble centre. The bubble diameter at a given height z measured from the distributor, $d_b = 2r_b$ can be calculated, for group B particles by Darton's correlation (Darton et al., 1977):

$$d_b = 0.54(U - U_{mf})^{0.4}(z + 4\sqrt{A_o})^{0.8}/g^{0.2} \tag{3.4}$$

where A_o is the distributor area per number of holes. The Davidson's model assumes an infinitely wide fluidized bed. However, according to van Ommen et al. (2004), for small diameter columns the effect of moving bed mass should be included. When the bed is in the bubbling regime, waves originated at the bed surface due to the motion in the freeboard caused by the erupting bubbles can be sensed also in the plenum therefore they represent the oscillating bed global behavior (van der Schaaf et al., 2002). Contrarily, rising bubbles generate local pressure fluctuations (Puncochar and Drahos, 2005; van der Schaaf et al., 2002). According to this, Bi (2007) proposed an expression for the fluctuating component of the signals from the absolute pressure measurement as:

$$p_{fluc}(t) = p_w(t) + p_b(t) \tag{3.5}$$

In the present work, p_b represents the fluctuating component corresponding to bubble passage calculated according to Eq. (3.2) and (3.3) and p_w represents the fluctuating component caused by other sources. A sinusoidal function is proposed to describe p_w

$$p_w(t) = A\sin(2\pi f t) \tag{3.6}$$

The amplitude of the global fluctuation A and its frequency f are determined as follows.

3.3.1 Main amplitude and frequency

Many studies have reported before that the amplitude of pressure fluctuations is proportional to the superficial gas velocity. According to Puncochar and Drahos (2005), the standard deviation of pressure fluctuations depends on the density of the particles, the excess gas velocity and a constant of proportionality dependent on bed geometry and probe position. Baskakov et al. (1986) and Alzahrani and Wali (1993) reported that the amplitude of the fluctuations is directly proportional to $\Delta p^{0.42}$. As the term Δp is proportional to the distance between the probe port and the bed surface, the amplitude can be considered proportional to $(L - z)^{0.42}$. Also Alzahrani and Wali (1993), using the empirical correlation developed by Talmor and Benenati (1963) established a relation between

the pressure fluctuation amplitude and the particle diameter. Provided the dependence on these parameters an empirical correlation for the amplitude of pressure fluctuations has been adjusted using experimental data available in the literature. In Fig. 3.2 data of the amplitude of absolute pressure fluctuations from several studies are presented (Felipe and Rocha, 2007; Hong et al., 1990; Svoboda et al., 1984; Puncochar et al., 1985; Croxford et al., 2005). Table 3.1 shows the particle properties, bed static height and probe position from the distributor for each measurement in Fig. 3.2.

The amplitude of the global pressure fluctuations $p_w(t)$ in Eq. 3.6 is therefore represented

Reference	Series in Fig. 3.2	L (cm)	z (cm)	ρ_p (kg/m^3)	d_p (μm)
Felipe and Rocha (2007)	A	22	14	2480	193
	B	22	15	980	329
	C	22	15	2720	106
Hong et al. (1990)	A	11	10	2670	715
	B	22	12.5	2670	715
	C	11	7.5	2670	359
	D	11	10	2670	359
	E	16.3	12.5	2670	359
	F	22	7.5	2670	359
Svoboda et al. (1984)		17	8.5	2220	565
Puncochar et al. (1985)		17	8.5	1680	90
Croxford et al. (2005)		46	10	2600	159

Table 3.1: Particle density, ρ_p, and diameter, d_p, bed height, L, and probe axial position, z, for experiments in Fig. 3.2.

by:

$$A = k(U - U_{mf})(L - z)^{0.4}\rho_p d_p^{1/5} \tag{3.7}$$

When spectral analysis of pressure signals in fluidized beds is applied, multiple peak frequencies can be identified. There is generally one with the highest power intensity in the power spectrum, which is usually identified as the dominant frequency. According to Bi (2007) most natural frequency equations in the literature agree reasonably well with the dominant frequency data. In the present model, the value of the frequency f representing the overall behavior of the bed is obtained from the equation by Hao and Bi

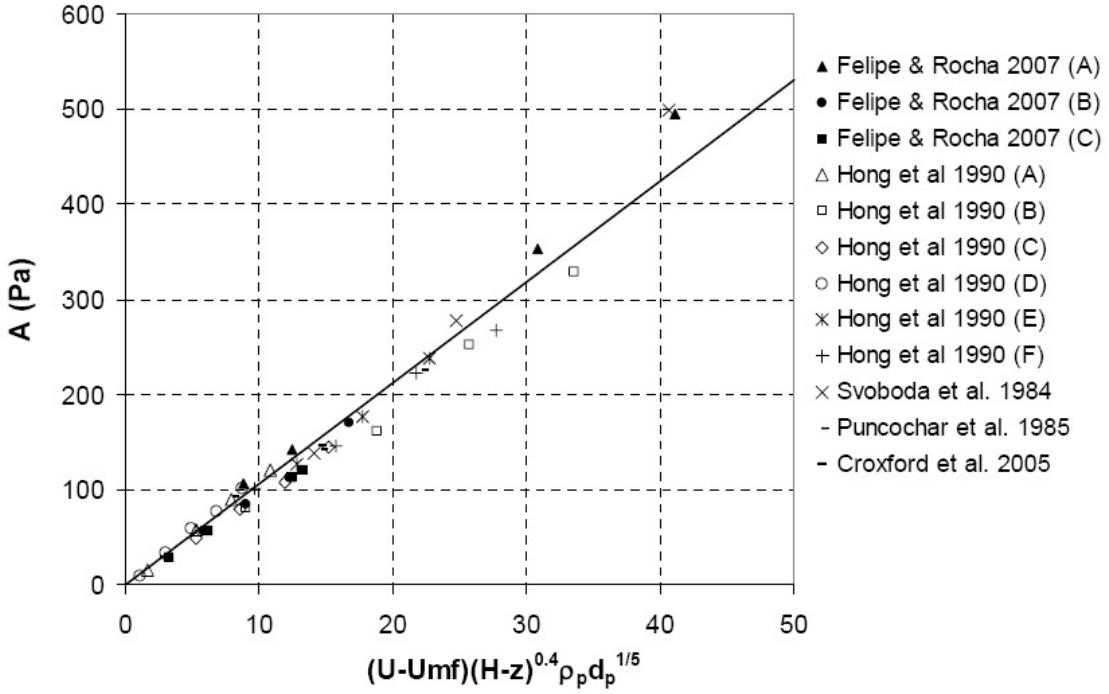

Figure 3.2: Amplitude of absolute pressure fluctuations.

(2005):

$$f = \frac{1}{\pi}\sqrt{\frac{g}{L}} \tag{3.8}$$

3.4 Results and discussion

The synthetic signals generated with the present model for the same conditions of the measurements described for rig A are compared in Fig. 3.3. The modeled pressure signal is:

$$p_{signal} = \rho_p(1-\epsilon)g(L-z) + p_{fluc}(t) \tag{3.9}$$

Where the first term is the hydrostatic pressure and the second term is the fluctuating component given in Eq. (3.5). Differential pressure has been calculated as the difference between the two pressure values p_{signal} at two different positions. Both absolute and

differential pressure values are shown for an enlarged time period of that of Fig. 3.1. The passage of three bubbles can be identified in the experimental measurements and in

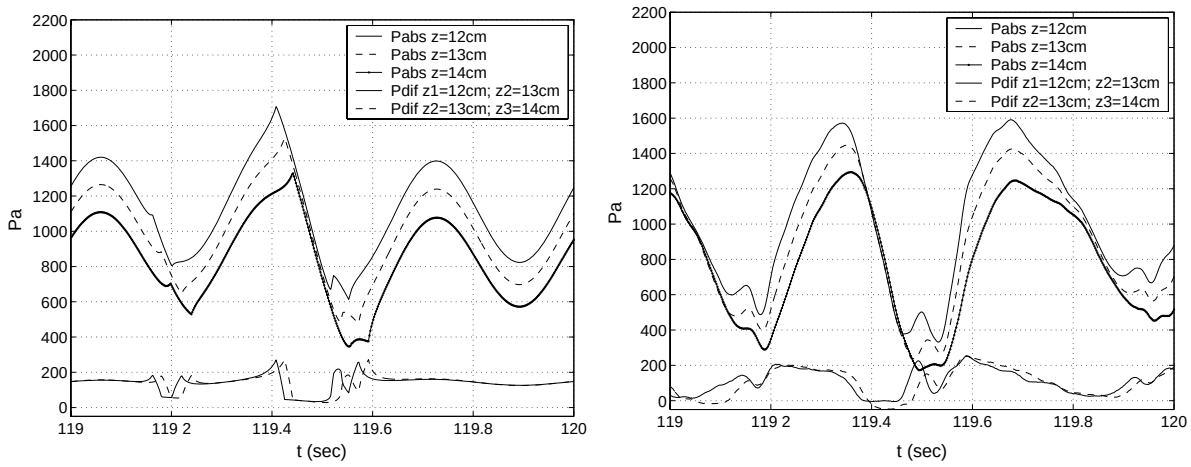

(a)

Figure 3.3: Absolute and differential pressure records: model (a) and (b) measurements.

the simulated records: one of the bubbles passes across the sensors giving a value of zero in the differential sensor (119.5 sec) and the two other bubbles are passing the probe with a certain eccentricity (Ramaya et al., 1996). A close agreement between experimental and simulated records is found. It can be observed that differential dual-sensors are more suitable than single point sensors to detect bubble passage and measure bubble parameters. As explained before pressure measurements from a single probe reflect more global phenomena in the bed as opposed to the differential probes that reflect phenomena occurring between the probe ports.

3.4.1 Standard deviation of pressure fluctuations

Fig. 3.4 shows the modeled standard deviation of differential and absolute pressure fluctuations against the gas velocity U, varying the probe height. The pressure has been calculated according to Eq. (3.9) where the fluctuating component p_{fluc} is obtained for particles of diameter $d_p = 680$ μm and density $\rho_p = 2632.5$ kg/m^3, in a bed of height $L =$ 22 cm, and with a minimum fluidization velocity $U_{mf} = 0.44$ m/s. Differential pressure has been calculated as the difference between the two pressures values at two different positions z_1 and z_2.

Standard deviation of absolute pressure fluctuation increases linearly with excess gas, when the first term in Eq. (3.5) is large compared to pressure fluctuations caused by a

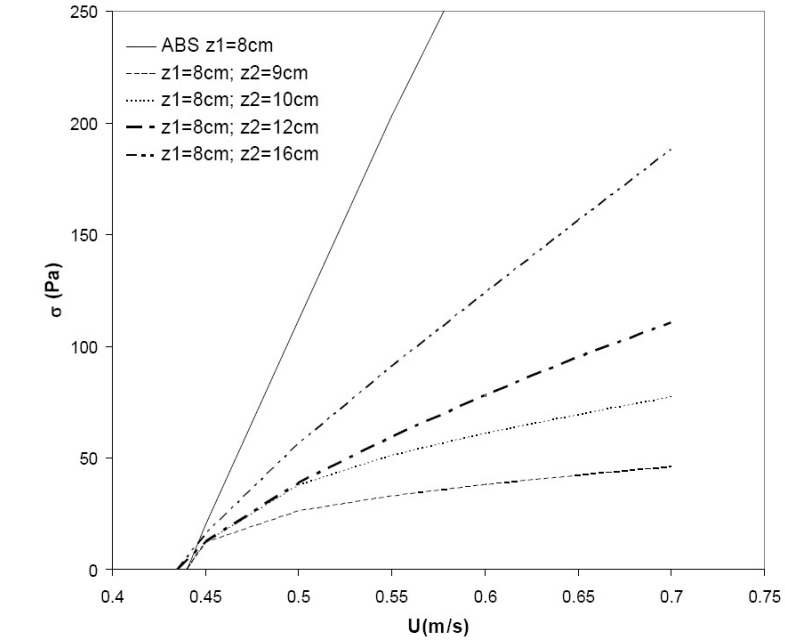

(a)

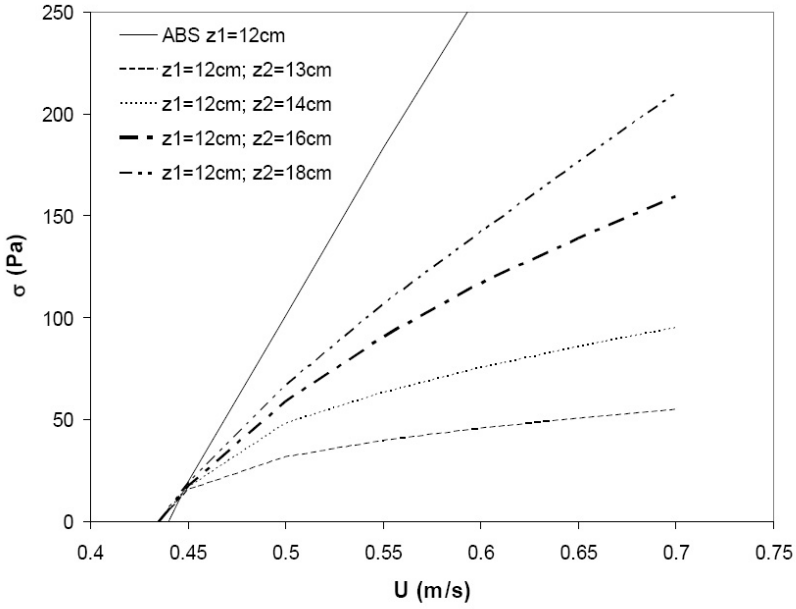

(b)

Figure 3.4: Standard deviation of absolute and differential pressure fluctuations calculated from the simulated pressure signal - Eq. 3.9 - at (a) $z_1 = 8$ cm (b) $z_1 = 12$ cm and different distances between pressure ports.

bubble passage. It can be observed in Fig. 3.4 that there is a low dependency of probe position on the absolute pressure measurement. On the other hand, for differential pres-

sure measurements, the standard deviation increases with excess gas, but it is found to be strongly dependent on the distance between ports and the probe height above the distributor. As the distance between ports of the differential probe increases, the local passage of the bubble becomes less important, and the differential probe tends to the absolute probe behavior. When the distance between probes is smaller than the expected bubble diameter for a given height, the standard deviation of differential pressure fluctuations as a function of air velocity correlates well with the diameter, as shown in Fig. 3.5. In this figure, the evolution of bubble diameter d_b with height z, for different excess gas velocities is represented (Fig. 3.5(a)) along with the calculated relation σ_P/d_b (Fig. 3.5(b)) for different probes heights and separation between ports. The expected bubble diameter for a given height has been calculated using Eq. (3.4). For low separation between ports, σ_P/d_b remains constant, at any excess gas: the diameter in all the range is larger than the probe separation and the fluctuation represents the bubble diameter behavior. As the separation increases (e.g. $s = 3$ cm), this holds only for higher excess gas. If the separation between ports increases still, then the fluctuation (represented by σ_p) does not follow only the diameter behavior but the contribution of the first term in Eq. (3.9), i.e. global phenomena in the bed, becomes more important. This result is in agreement with the work by van der Schaaf et al. (2002) who reported that the incoherent standard deviation of pressure fluctuations was proportional to the average bubble diameter, provided the incoherent standard deviation gives information on the amplitude of pressure fluctuations caused by rising gas bubbles, solids clusters, and turbulence.

That is in agreement with Sitnai (1982) and Ramaya et al. (1996) who recommended a maximum distance between ports for a correct measurement of the bubble characteristic length. Nevertheless, the experimental measurements they present were conducted injecting one controlled bubble in a bed at incipient fluidization condition, and therefore the general oscillation of the bed was not present.

The method of the standard deviation of pressure fluctuations to predict the minimum fluidization velocity (Puncochar et al., 1985), has been extensively used in the literature. According with the shown results this holds for absolute measurements and may also be used with differential sensors, as long as the distance between ports is large enough. This is for example, the case of the measurements of Felipe and Rocha (2007) who reported absolute and differential pressure measurements in a bubbling fluidized bed. Fig. 3.6 shows values from their experiments and those predicted by the present model. In this case, the distance between the differential pressure ports is large enough and then standard deviation trend for differential and absolute measurements is similar and a linear

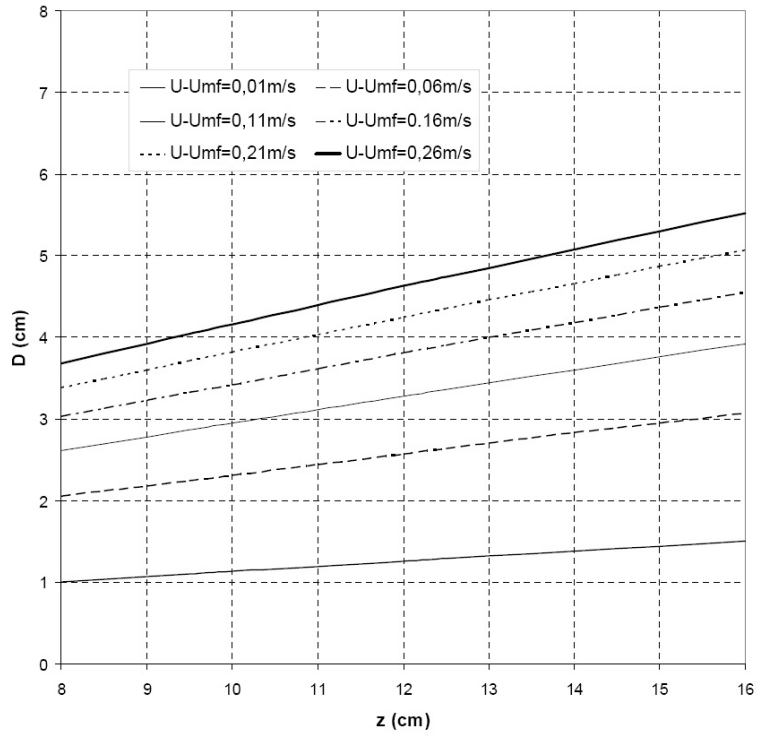

(a)

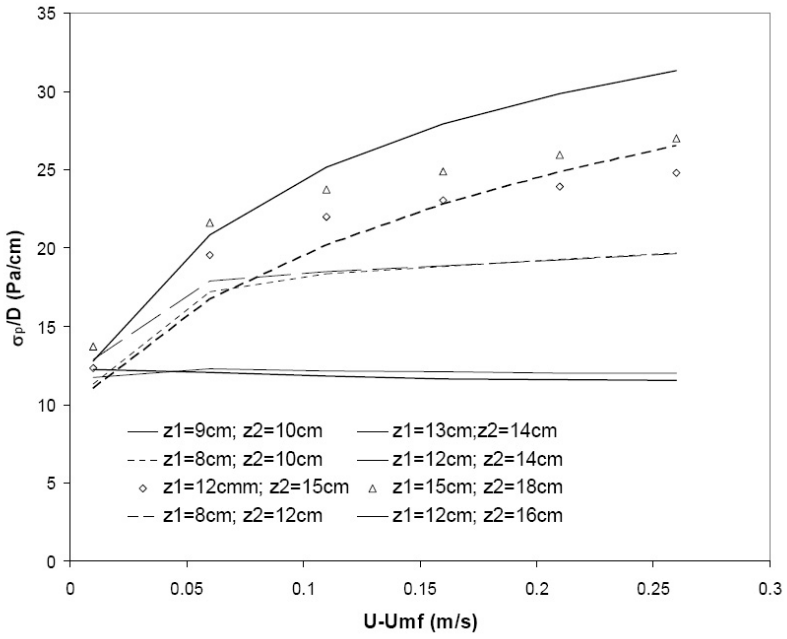

(b)

Figure 3.5: (a) Expected bubble diameter d_b. (b) Calculated σ_P/d_b at different bed heights z and excess gas conditions.

increase with the excess gas is found.
Finally, the predicted evolution of the standard deviation of absolute and differential

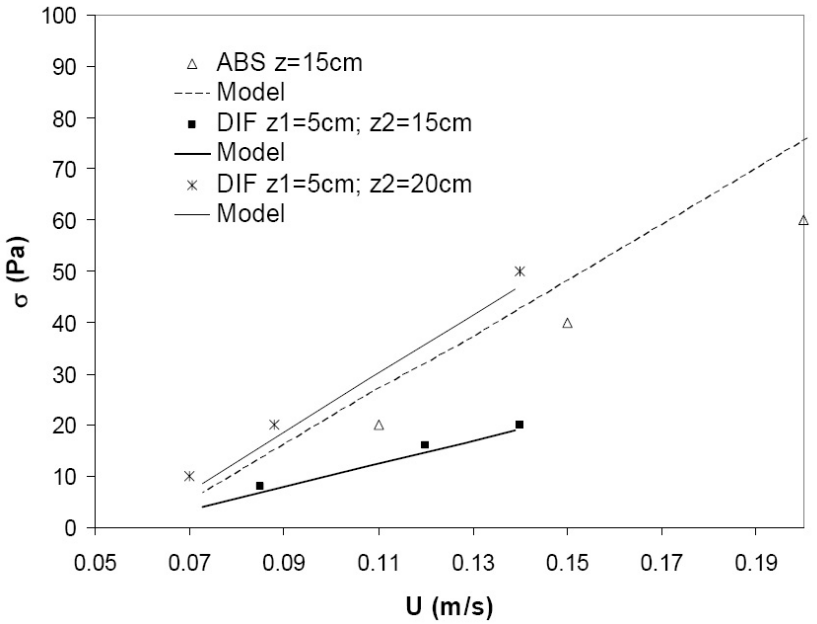

Figure 3.6: Standard deviation of pressure fluctuation against superficial velocity U for differential and absolute pressure measurements from work of Felipe and Rocha (2007) and this work model.

pressure fluctuations as a function of excess gas has been validated with two set of measurements. Experimental results for rig A are shown in Fig. 3.7.
The model and the experimental values follow the same trend. Fig. 3.8 depicts the standard deviation of pressure fluctuations against the gas velocity for the second set-up (rig B). It can be seen that experimental data follow the linear relationship predicted by the model for the absolute pressure fluctuations. It can also be observed that as predicted, the differential pressure probe with a higher distance between ports shows a behavior that resembles the absolute measurements.

3.5 Conclusions

A simple method for the simulation of the pressure signal in a bubbling fluidized bed for group B particles is presented. The corresponding standard deviation of the synthetic signal compares well with experimental results. The use of standard fluctuations of differential pressure to determine the minimum fluidization velocity can be achieved

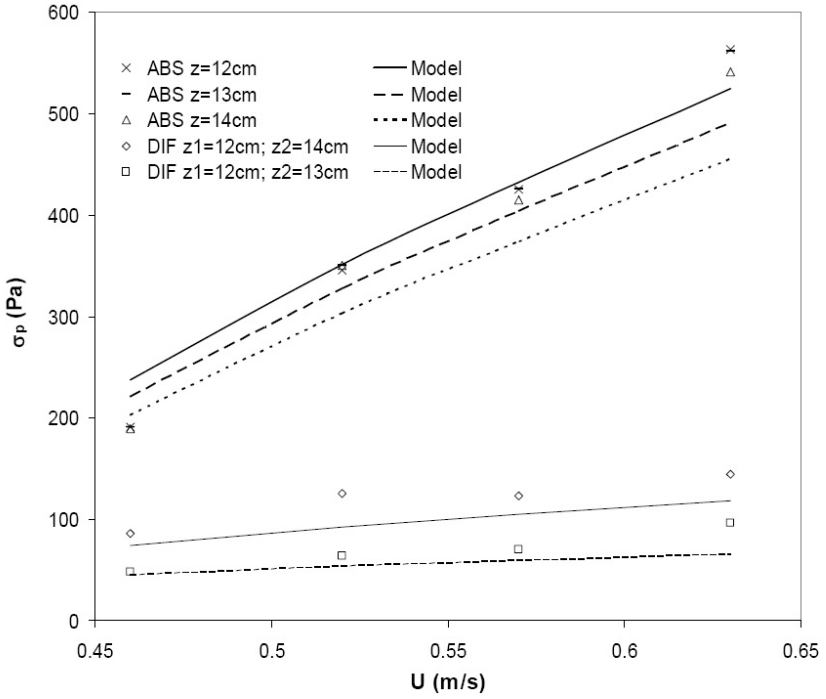

Figure 3.7: Standard deviation σ_p of absolute and differential pressure measurements carried out in rig A against gas velocity U.

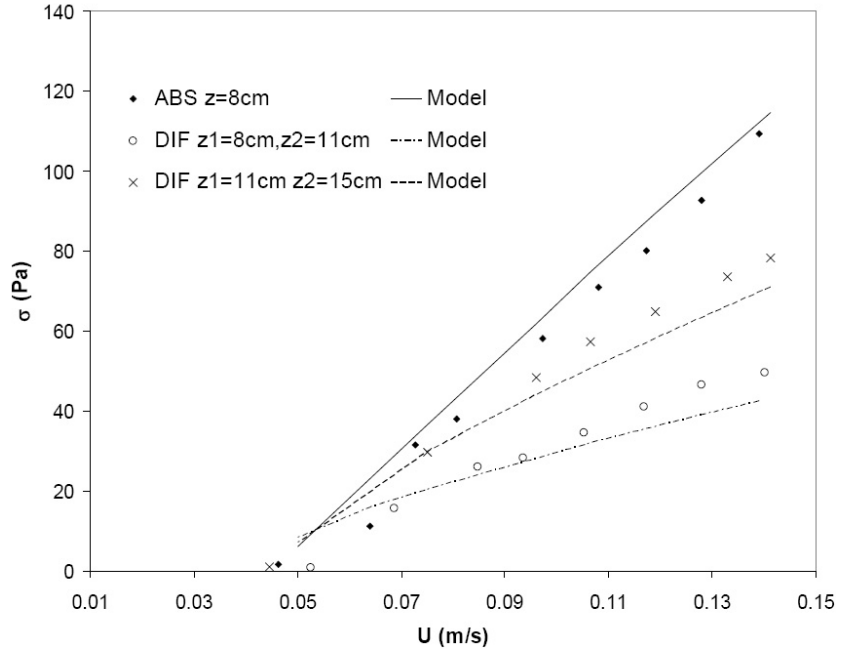

Figure 3.8: Standard deviation σ_p of absolute and differential pressure measurements carried out in rig B against gas velocity U.

provided that the separation between probes is larger than the expected diameter for the given measurement position. The standard deviation of differential pressure fluctuations was found to be proportional to the bubble diameter, provided that the distance between probes is small enough.

Chapter 4

Global characterization of the fluidized bed with rotating distributor

This chapter evaluates the performance of this new design, considering pressure drop, Δp, and quality of fluidization. Bed fluidization was easily achieved with the proposed device, improving the solid mixing and the quality of fluidization.
In order to examine the effect of the rotational speed of the distributor plate on the hydrodynamic behavior of the bed, minimum fluidization velocity, U_{mf}, and pressure fluctuations were analyzed. The pressure drop across the bed and the standard deviation of pressure fluctuations, σ_p, were used to find the minimum fluidization velocity, U_{mf}. A decrease in U_{mf} is observed when the rotational speed increases and a rise in the measured pressure drop was also found. Frequency analysis of pressure fluctuations shows that fluidization can be controlled by the adjustable rotational speed, at several excess gas velocities.
Measurements with several initial static bed heights were taken in order to analyze the influence of the initial bed mass inventory over the effect of the distributor rotation on the bed hydrodynamics.

4.1 Introduction

Fluidized beds present high mass and heat transfer rates what make them suitable in many industrial gas-solid applications (such as drying and granulation) as well as in the combustion, pyrolysis or gasification of many solid fuels, where they offer advantages

over other types of reactors. Nevertheless, depending on the application, fluidization is sometimes difficult to achieve due to the agglomeration or cohesion between particles and defluidization or non-uniform fluidization may occur.

The non-homogeneous structures found in industrial fluidization processes have been studied by many investigators who have analyzed, among others, the influence of the particle size distribution and the bed pressure (Wiman and Almstedt, 1998; Olowson and Almstedt, 1990) or the effect of the type of gas distributor (Werther, 1978) on the hydrodynamics of gas fluidized beds. The difficulty to fluidize A and C particles, as well as the need to maintain a good mixing between phases and a high particle dispersion, has led many investigators to modify the conventional fluidized bed devices, alter the air supply system or try innovative designs.

Flow pulsation to control the bubble size and enhance the quality of fluidization has been used in a few experimental studies (Moussa et al., 1982). In a fluidized bed, pulsation can be introduced by several methods: intermittent air supply, sonic waves or vibration. Vibrated beds (Bratu and Jinescu, 1971; Mawatari et al., 2003; Noda et al., 1998) have been extensively tested to fluidize A and C particles. The vibration imparted to the bed breaks the stable fixed channels that appear when operating with these groups of particles, and a better mixing between gas and particles in the bed is achieved. Minimum fluidization velocity becomes lower for vibrating fluidized beds and the pressure tends to decrease at incipient fluidization. A similar decrease in minimum fluidization velocity is obtained for Group B particles in sound assisted beds (Leu et al., 1997; Herrera and Levy, 2001). In this case, the pressure in the bed does not change. Low-frequency vibrations have also been applied in gas-liquid fluidized bed, turning out in smaller bubbles to be generated in the distributor (Ellenberger and Krishna, 2003). Providing the different nature of gas-solid and gas-liquid fluidized beds, there are studies that show analogies on the hydrodynamic behavior of gas-solid and gas liquid fluidized beds (Ellenberger and Krishna, 1994).

Other investigators have tried to overcome the difficulties in mixing between phases and between solids in the bed, by modifying the distributor layout. In the spiral distributor (Ouyang and Levenspiel, 1986) and its improved version (Sreenivasan and Ragahavan, 2002), the gas enters the bed tangentially through overlapping blades shaped as full sectors of a circle, welded at the center. This configuration imparts a swirling motion to the solids. This horizontal convective movement of the particles improves the radial mixing of solids and the gas-solids contact. This effect is restricted to the lower part of the bed and its complete effectiveness is only appreciable in shallow fluidized beds. A similar effect

is found in the swirling distributor (Chyang and Lin, 2002) where the swirling fluidizing pattern is generated by a multi-horizontal nozzle distribution in the plate.
The present design consists on a rotational distributor plate, whose aim is to overcome low radial gas mixing and particle dispersion, and to achieve a more uniform fluidization. Other investigators (Esin and Cakaloz, 1979; Elder, 1956) found a more uniform concentration gradient in the radial direction using rotating distributor plates. A decrease of the mean bubble diameter by increasing the rotational frequency of a porous plate distributor, has also been observed in generation of micro-air-bubbles in gas-liquid experiments (Fujikawa et al., 2003).
The rotating distributor offers the advantages found in both, the swirling designs, that improved solid mixing and achieved the fluidization even for very shallow beds and the vibrating and sound assisted beds where the minimum fluidization velocity decreases. Besides, its design is simpler than the sound assisted or vibrated beds ones. Furthermore, the possibility to control and adjust the rotational speed of the distributor plate offers a wider range of operating conditions while maintaining the quality of fluidization.
The effect of the distributor plate rotation on the structure of a fluidized bed operated with Group B particles was experimentally studied: the influence of the rotational speed on the minimum fluidization velocity, the standard deviation of pressure fluctuations and the hydrodynamic characteristics of the bed are presented. It was found that the minimum fluidization velocity decreases as the rotational speed increases and a change in the pressure drop was also noticed. Experiments were carried out at several static bed heights, in order to detect the bed depth limit beyond which the influence of the distributor rotation is negligible.

4.2 Experiments

The schematic diagram of the test rig is given in Fig. 4.1. The experimental set-up consists of a transparent cylinder with 0.192 m i.d. and a height of 0.8 m.
The rotating distributor is a perforated plate with 2 mm holes, giving a total open area ratio of 1%. The plate is covered with a fine-mesh net to prevent particles from falling down through the plate into the wind-box. The holes are laid out in hexagonal pitch of 15 mm. A spiral pitch distributor with the same open area ratio was also tested. At the bed axis, the distributor is coupled to the shaft of an AC electric motor with a 1:15 reducer. The rotational speed can be controlled using a frequency inverter and it ranges from 0 to 100 rpm. A detail of the mechanical set-up and the design of the distributor plates are

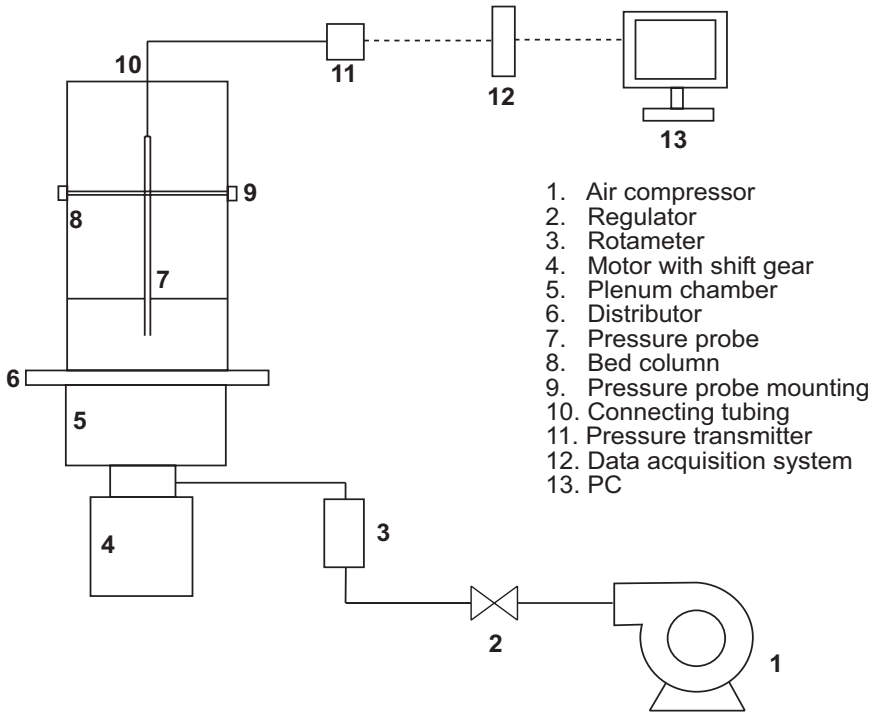

Figure 4.1: Schematic diagram of the experimental fluidized bed.

shown in Fig. 4.2.

The bed was filled with Geldart B silica sand particles with a mean diameter of 680 μm and a density of 2632.5 kg/m^3. The settled bed heights were varied from $L/D = 0.35$ to $L/D = 0.75$, corresponding to bed inventories of 2 kg to 6 kg of sand. The air flow rate was measured with a rotameter. The volumetric flow rates ranged from 0 l/min to 1400 l/min, resulting in a fluidizing velocity of 0 to 0.8 m/s.

Pressure measurements were taken in the bed. The pressure sensor was initially placed flush to the bed wall. Nevertheless, the pressure fluctuations series showed a periodic cycle due to the distributor rotating frequency, what hindered the analysis of the frequency distribution in the fluidized bed. To avoid this problem the pressure probe was mounted at the bed axis (Svoboda et al., 1983). The pressure drop across the bed and the pressure oscillations were measured with an Omega PX 291 piezoresistive differential pressure transmitter (0-5 in H_2O) with a 1% FS accuracy. The sensor was mounted on a 5 mm i.d. steel probe and silicone connecting tubing of 4 mm i.d. and the whole set-up had a length of about 2 m. According to Xie and Geldart Xie and Geldart (1997), the response time of the probe-transducer set-up depends mainly on the diameter of the probe and the connecting line. The probe used in the experiment proved to give a fast response

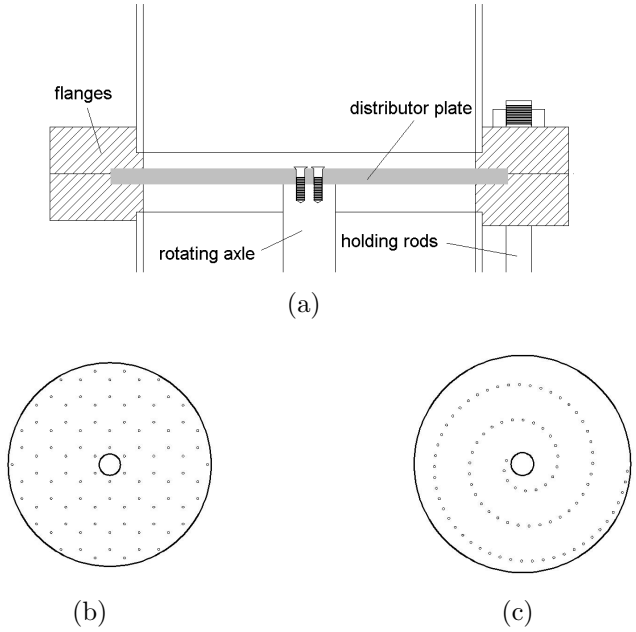

Figure 4.2: (a) Detail of the mechanical set-up of the rotating distributor (b) Uniform pitch distributor (c) Spiral pitch distributor.

without notably distorting the bubble path. The measurements were taken about 5 cm below the bed surface, roughly in the middle of the bed. The high pressure port was placed at this point and the low pressure port was exposed to atmosphere. The tip of the pressure probe was covered with a fine-mesh net at the side facing the flow in order to avoid the fine particles going into the tube. The data were recorded with a 12 bits data acquisition board (ICP DAS PCI-1802H) assembled in a PC. The resultant accuracy in pressure measurements was approximately ± 12 Pa. Time series of 12000 data points measured with a sample frequency of 200 Hz were processed to obtain standard deviations and power spectral density functions.

4.3 Results and discussion

Pressure measurements were used to examine the effect of the rotational speed of the distributor plate on the hydrodynamic behavior of the bed. The following aspects were evaluated:

1. The pressure drop across the bed over a wide range of gas velocities.

2. The minimum fluidization velocity U_{mf} calculated with the standard deviation of pressure fluctuations, σ_p.

3. The response of the bed in the frequency domain.

Additional experiments were carried out at several fixed bed heights to find out the bed height up to which the global effect of the rotation is still perceptible.

4.3.1 Effect of the rotational speed on the hydrodynamic behavior of the bed

Minimum fluidization velocity

The pressure drop across the bed was measured at a range of superficial gas velocities, U, beginning with a vigorously fluidized bed and reducing to zero velocity. All measurements were taken decreasing the flow rate, in order to avoid the hysteresis that appears when the velocity is increased from U = 0 m/s. This hysteresis is due to the wedging action within the fixed bed (Davidson and Harrison, 1963). Fig. 4.3 compares the measured pressure drop for the distributor plate rotating at the maximum rotational speed (n = 100 rpm) with the measurements without rotation.

When the distributor plate rotates, U_{mf} decreases, and a moderate increase in the pressure drop is found, for gas velocities below $2U_{mf}$. The rise in the pressure drop is in agreement with the results of other investigators (Esin and Cakaloz, 1979). The change in this trend, when operating at higher gas flows, can be attributed to a predominant influence of the axial gas velocity, as opposed to the tangential velocity imparted by the distributor rotation to the bed. The method used above for the experimental determination of the minimum fluidization velocity needs measurements made in both, free bubble fluidization and fixed bed regimes, including the complicated transition region.

A better estimate of U_{mf} for Geldart B particles is obtained using a second method consisting on measuring the pressure fluctuations in the bed (Puncochar et al., 1985; Wilkinson, 1995; Briongos et al., 2006). Fig. 4.4 shows the standard deviation of pressure fluctuations, σ_p, for a range of gas velocities at several rotational speeds. U_{mf} is calculated for each rotational speed by the intercept of the extrapolated line with the U axis ($\sigma_p = 0$). The least squares method was used to calculate the linear relationship between σ_p and U. Fits with a R-square greater than 0.98 were obtained.

The values of U_{mf} at each rotational speed, normalized with respect to U_{mf} for the static distributor configuration, $U_{mf,0}$, are plotted in Fig. 4.5 against the centripetal acceleration, $\omega^2 R_m$ (ω is the angular velocity of the distributor plate and R_m its average radius), nondimensionalized with the gravitational acceleration, g. The value $\omega^2 R_m/g$ is proportional to the quotient between the centrifugal force and the buoyancy force acting on the

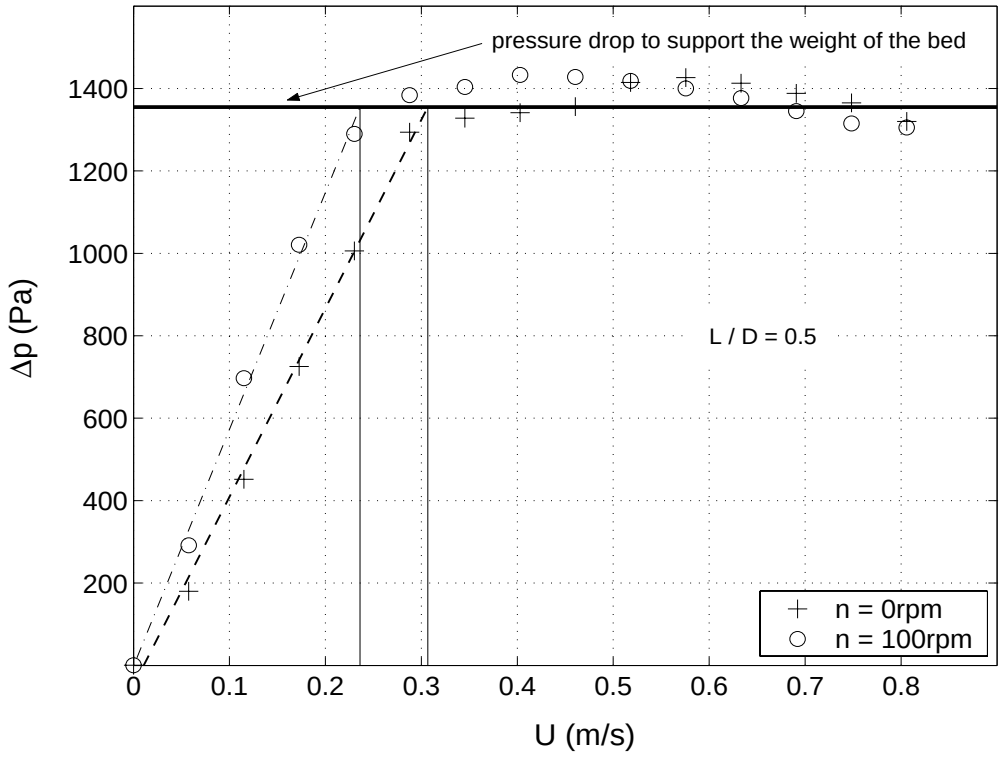

Figure 4.3: Pressure drop across the bed, Δp, as a function of the superficial gas velocity, U, for $n = 0$ rpm and $n = 100$ rpm.

bubbles ascending through the bed. It is shown that the decrease in U_{mf} is higher as the angular velocity of the distributor plate, ω, increases. For low values of ω a negligible effect was found.

A second hole layout in the distributor plate was experimented besides the triangular pitch. It consisted on a spiral pitch layout. The experiments suggested a worse performance compared with the triangular pitch layout (holes uniformly distributed). However the same trend was found with regard to the U_{mf} decrease when the distributor plate rotates, as also shown in Fig. 4.5.

To compare the performance of the bed at several rotational speeds but at the same fluidization regime, gas velocity U is nondimensionalized with the minimum fluidization velocity for the respective rotational speed. This approach is shown in Fig. 4.6, where it can be seen a very similar amplitude of pressure fluctuations, σ_p against U/U_{mf} for several rotational speeds. This result indicates that the fluidization quality is very similar independently of the rotational speed for the same excess gas U/U_{mf}. However this similarity tends to disappear for an excess gas about $U/U_{mf} = 1.6$.

The bed behavior using the novel rotating design could be advantageous for partial oxi-

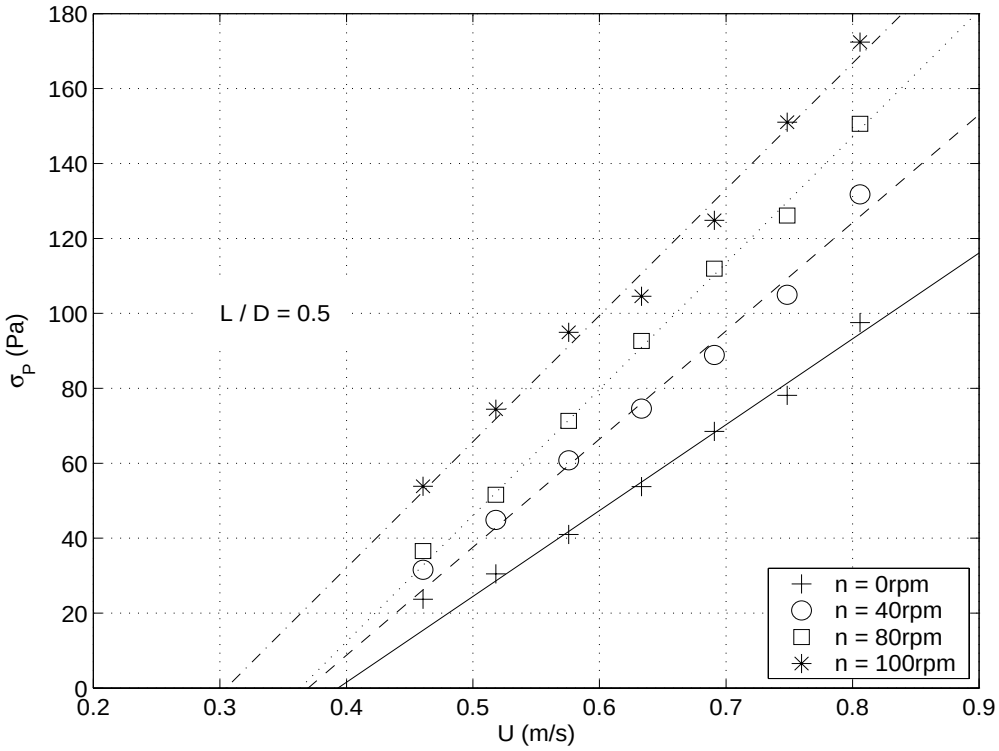

Figure 4.4: Standard deviation of pressure fluctuations, σ_p, for several rotational speeds, n, against gas velocity, U.

dation processes in fluidized beds (e.g., coal gasification) operating in the free bubbling regime, as the proposed design would enable to fluidized the bed more easily, even in the case of particle agglomeration due to the low melting point of some compounds. The fluidization might more closely resemble particulate than bubbling fluidization. Besides that, the rotation would add a new free parameter which allows to operate with a lower air rate keeping the desired excess air ratio.

Frequency domain analysis

According to Johnsson et al. (2000), the amplitude of pressure fluctuations signals expressed as standard deviation, is not sufficient to quantify the bed dynamics and in some cases can be misleading. A change in amplitude can be caused by a redistribution of solids in the fluidized bed without any significant change in the dynamics of the flow. Spectral analysis may give a quite different picture from that of amplitude analysis. Therefore analysis of frequency distribution of pressure time series is also discussed.
Welch method is used for power spectrum estimation (Welch, 1967). A hamming window

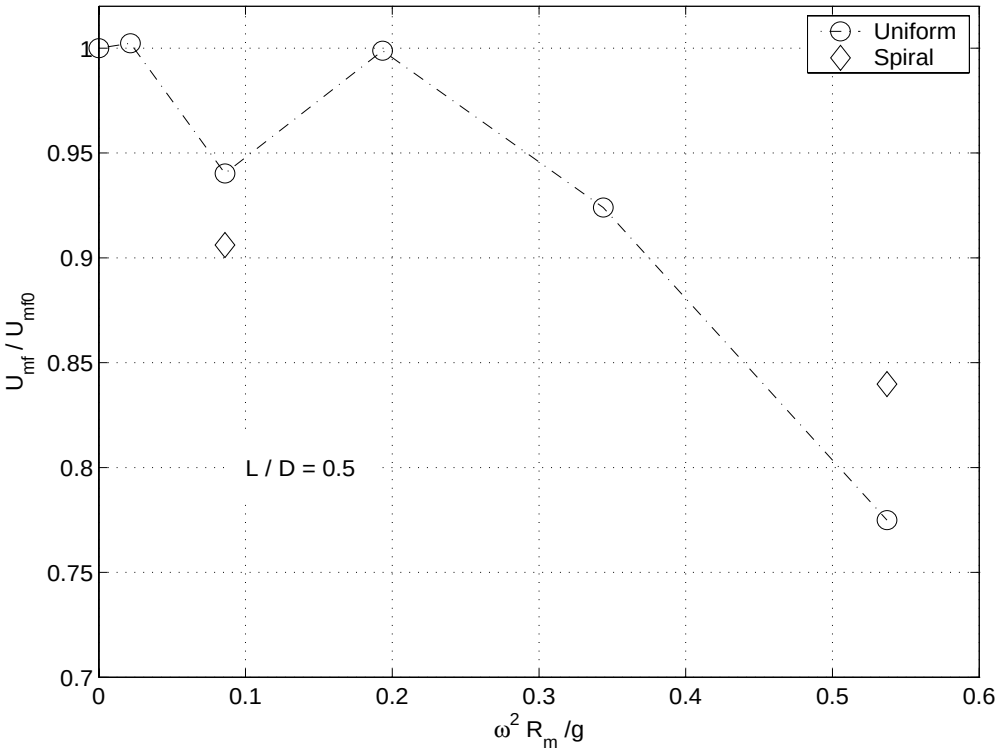

Figure 4.5: $U_{mf}/U_{mf,0}$ against the non-dimensional centripetal acceleration of the distributor plate, $\omega^2 R_m/g$.

is chosen as window function. All sub-spectra are based on 4096 samples yielding an average of 8 sub-spectra.

The power spectra of pressure time series of the static distributor and the rotating distributor, have been compared for the same gas velocity, in order to determine the gas flow needed to fluidize the bed. Fig. 4.7 shows the power spectra for a gas velocity close to U_{mf} at $n = 100$ rpm ($U = 0.3$ m/s). At this gas velocity bubbles are detected when the distributor plate rotates. However using the static distributor no bubbles are found. It is confirmed that a lower gas velocity is needed to fluidize the bed when the rotating distributor is used.

The influence of the rotational speed of the distributor plate in the bed dynamics was analyzed at a given excess gas U/U_{mf}. Fig. 4.8 shows the first 10 Hz (of 100 Hz measured) of the bed power spectra for an excess gas flow of $U/U_{mf} = 1.3$, at 4 different rotational speeds.

A quite similar behavior in the frequency domain is shown at every distributor rotational speed. The same dominant frequency of 4 Hz and an energy of the signals about 1000 Pa^2/Hz is observed.

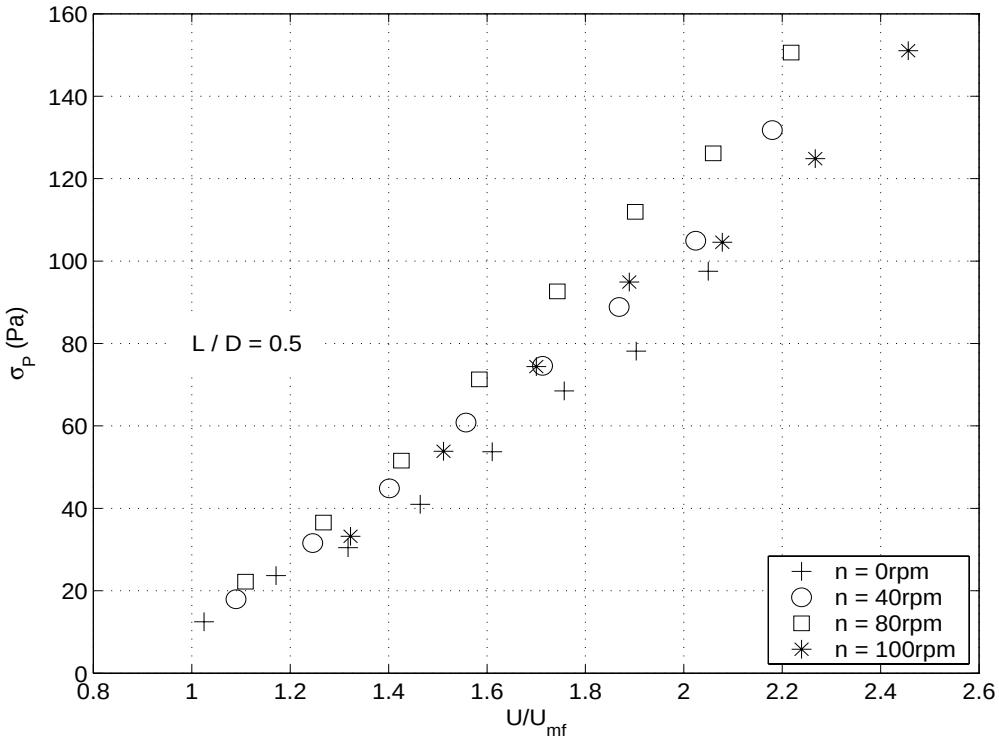

Figure 4.6: Standard deviation of pressure fluctuations, σ_p, for several rotational speeds against the excess gas U/U_{mf}.

The influence of the rotational speed on the bed dynamics can be explained in terms of the relation between the tangential velocity, ωR_m, imparted to the flow by the distributor rotation and the superficial gas velocity, U, which has an axial direction. The average tangential velocity of the gas in contact with the distributor plate, ωR_m, is about 0.5 m/s when the plate rotates at 100 rpm. This velocity value is about $1.6U_{mf}$. Accordingly, with gas velocities U, above $1.6U_{mf}$, the gas would have a predominantly axial direction. Otherwise, that is $U < 1.6U_{mf}$, the effect of the tangential velocity imparted to the gas by the distributor would be dominant. Fig. 4.8 compares at $U/U_{mf} = 1.2$ (Fig. 4.9(a)) and $U/U_{mf} = 2$ (Fig. 4.9(b)) the power spectrum of pressure fluctuations for the static distributor, with the corresponding power spectrum of the distributor rotating at 100 rpm. It was already shown that if the tangential velocity is of the same order of the superficial gas velocity, the same amplitude of the pressure signal can be observed regardless of the rotational speed (Fig. 4.6). Moreover, attending to frequency domain tools, it is now shown that an smaller peak in the power spectrum is found when the rotating distributor (Fig. 4.9(a)) is used.

Nevertheless, the improvement in the quality of fluidization achieved with the novel dis-

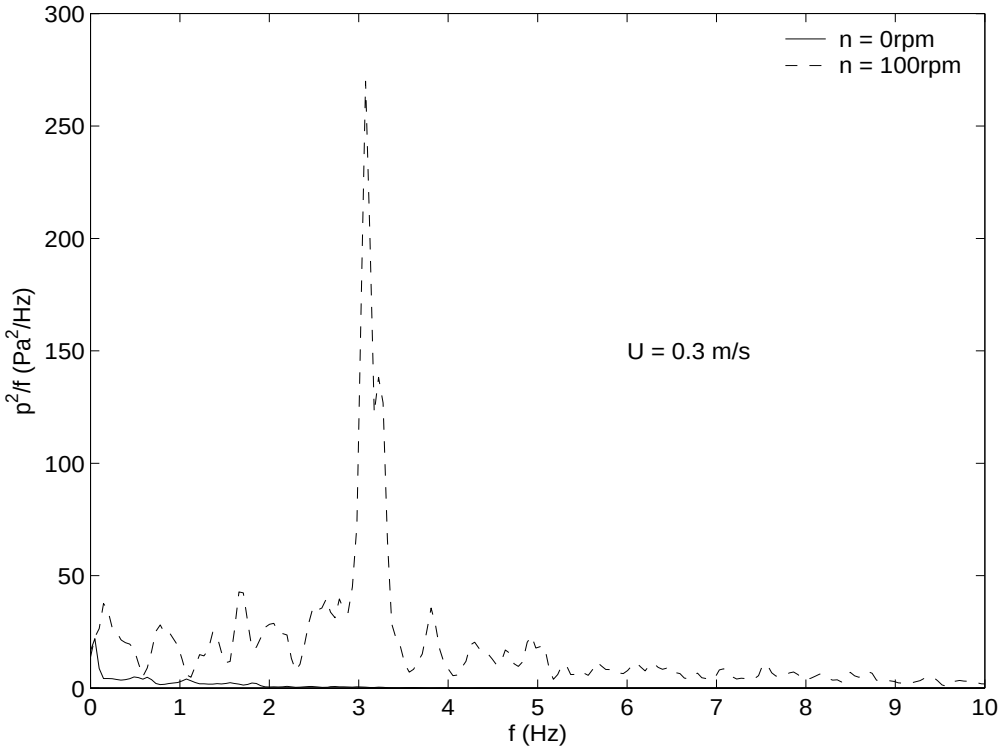

Figure 4.7: Power spectra for a gas velocity $U = 0.3$ m/s and a fixed bed height $L/D = 0.5$ at $n = 0$ rpm and $n = 100$ rpm.

tributor, tends to disappear when the tangential velocity, ωR_m, becomes smaller than the gas velocity. In Fig 4.9(b), at an excess gas of $U/U_{mf} = 2$, the gas flow supplied to the bed with the rotating distributor is such that $U > \omega R_m$. In this case the standard deviation of pressure fluctuations has a higher amplitude for the rotating distributor configuration, as already shown in Fig. 4.6. However, using frequency domain analysis, power spectra of the same energy are found for both the static and the rotating distributor configurations. The dominant frequencies observed are also the same.

Comparing Fig. 4.9(a). and Fig. 4.9(b). a rise in the dominant frequency can be observed when the gas velocity increases for both rotational speeds.

The performance of the novel fluidized bed proposed in this paper has two main contributions. On the one hand, a lower gas flow is needed to fluidize the bed what is useful in applications with this request. On the other hand, a new operating parameter appears; if an specific value of the gas flow is required in practical applications, the bed dynamics can be controlled by adjusting the rotational speed of the distributor plate, without loosing the quality of the fluidization. In other words, at a fixed gas velocity a more vigorously fluidization can be achieved by increasing the rotational speed of the distributor while a

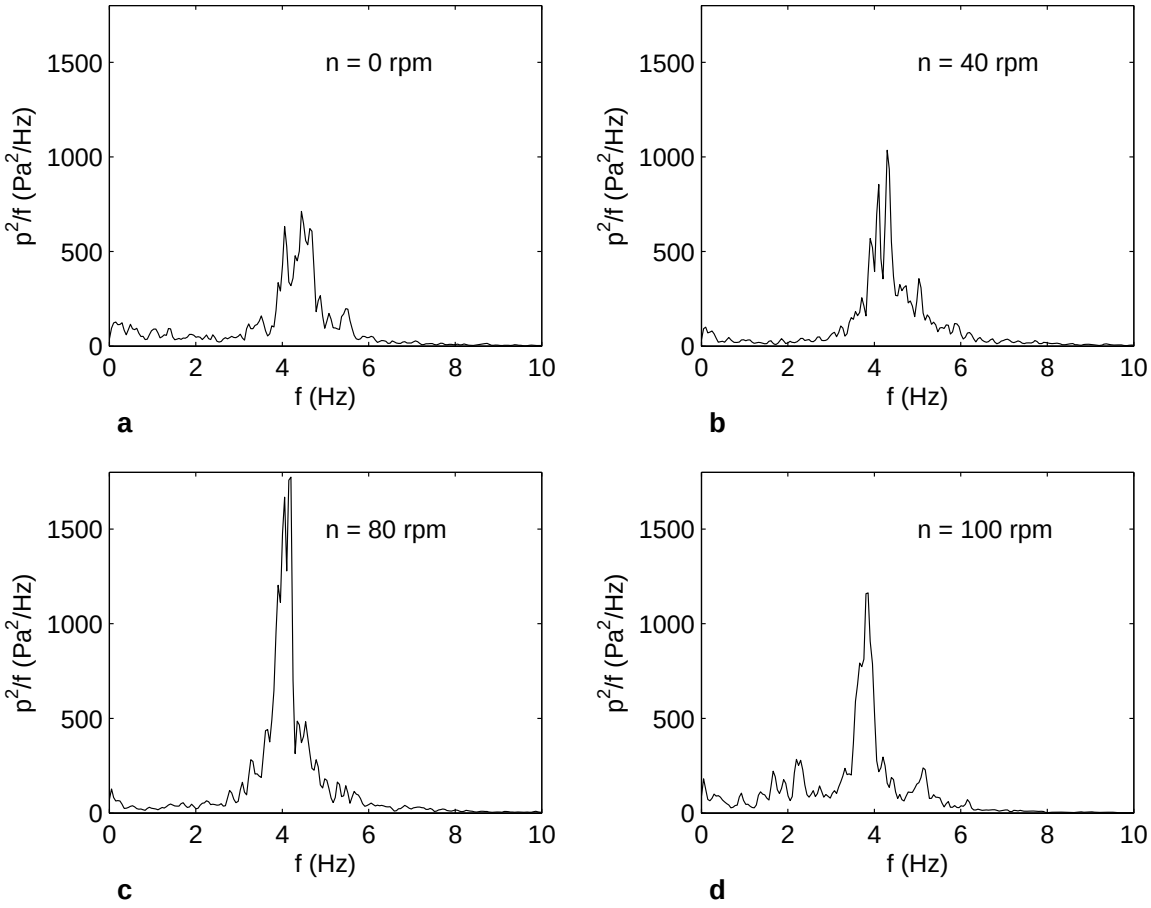

Figure 4.8: Power spectra: (a) $n = 0$ rpm, (b) $n = 40$ rpm, (c) $n = 80$ rpm and (d) $n = 100$ rpm, fixed bed height $L/D = 0.5$ and excess gas $U/U_{mf} = 1.3$.

lower bubble formation is achieved by decreasing the rotational speed.

4.3.2 Effect of the bed height in the rotating distributor configuration

Several studies have demonstrated that there is not a significant change in U_{mf} when the settled bed depth varies (Delebarre et al., 2004). In order to study how the effect of the distributor rotation on the hydrodynamics of the bed is affected by the static bed height, experiments were carried out at several fixed bed heights with the static distributor and with the new distributor rotating at $n = 100$ rpm.

For very shallow beds, $L/D \sim 0.25$, continuous gas channels are observed in the bed for the static distributor configuration. When the distributor plate rotates, the gas flow is locally interrupted and jets formed at each hole are broken, achieving a bubbling like

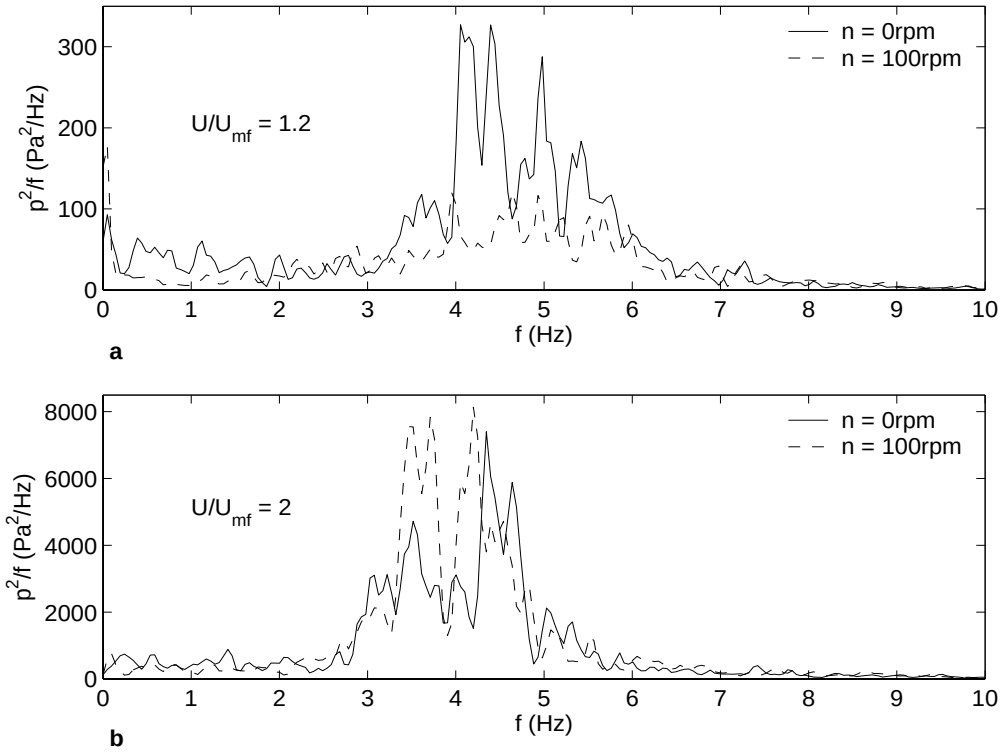

Figure 4.9: Power spectra for an excess gas: (a) $U/U_{mf} = 1.2$, (b) $U/U_{mf} = 2$ and a fixed bed height $L/D = 0.5$.

fluidization. Visual observation of the flow at the wall of the column shows how particles and bubbles are dragged by the plate rotation, what together with the axial gas flow results in an helicoidal path of the bubbles along the bed.

Fig. 4.10 compares the power spectra of the rotating distributor configuration ($n = 100$ rpm) with the static distributor configuration, both operating at the same gas velocity $U = 2U_{mf}$ and fixed bed height $L/D = 0.35$. The U_{mf} used to determine the gas flow rate U/U_{mf} are the values calculated in section 4.3.1 for a fixed bed height $L/D = 0.5$, since no change in U_{mf} with height is assumed. The power spectrum shows how the rotation makes the fluidization of the bed possible and a bubbling characteristic frequency of 5 Hz appears when using the distributor plate rotating at 100 rpm.

For a high enough bed height (about $L/D = 0.5$) uniform fluidization is achieved with both, static and rotational distributor beds. Fig. 4.11 shows the trend of the minimum fluidization velocity of the rotating distributor bed non-dimensionalized with the minimum fluidization velocity of the static distributor bed, $U_{mf,0}$, with the settled bed height. The rotation effect becomes less important when the bed height increases and it is globally negligible for bed heights over $L/D = 0.75$. However a local study of the bottom bed

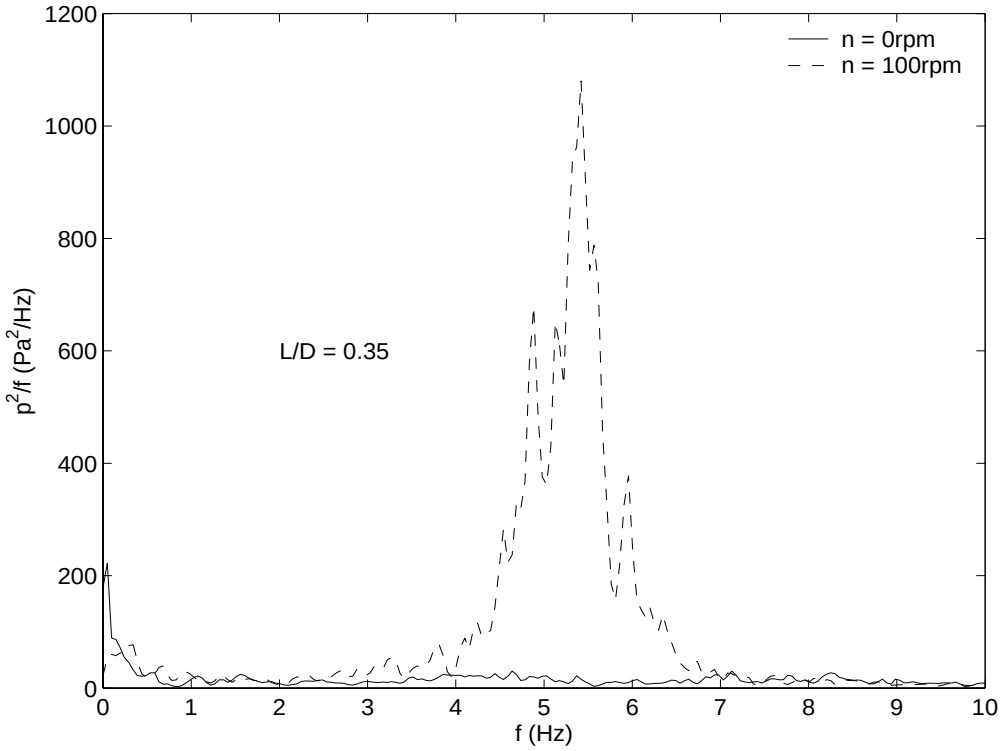

Figure 4.10: Power spectra at $U/U_{mf} = 2$, fixed bed height $L/D = 0.35$, $n = 0$ rpm and $n = 100$ rpm.

area would probably show an important effect of the rotation in this area independently of the bed height.

4.4 Conclusions

This study has shown the characterization of the proposed rotating distributor plate. This design is optimum when a feed stream of solids must be quickly dispersed all over the bed as they may be immediately horizontally transported by the rotation. The distributor plate rotation promotes an increase in the radial dispersion of the particles, reducing the high concentration zones present at the fluidized beds. This rapid mixing also prevents the temperature gradient, such as a hot spot near the feed point, in a fluidized bed combustor. Some differences were found in the hydrodynamics of the bed in relation to the classical static distributor:

(a) If $\omega^2 R_m > 0.2g$ the minimum fluidization velocity is 10% lower for the rotating distributor configuration and this value decreases when increasing ω.

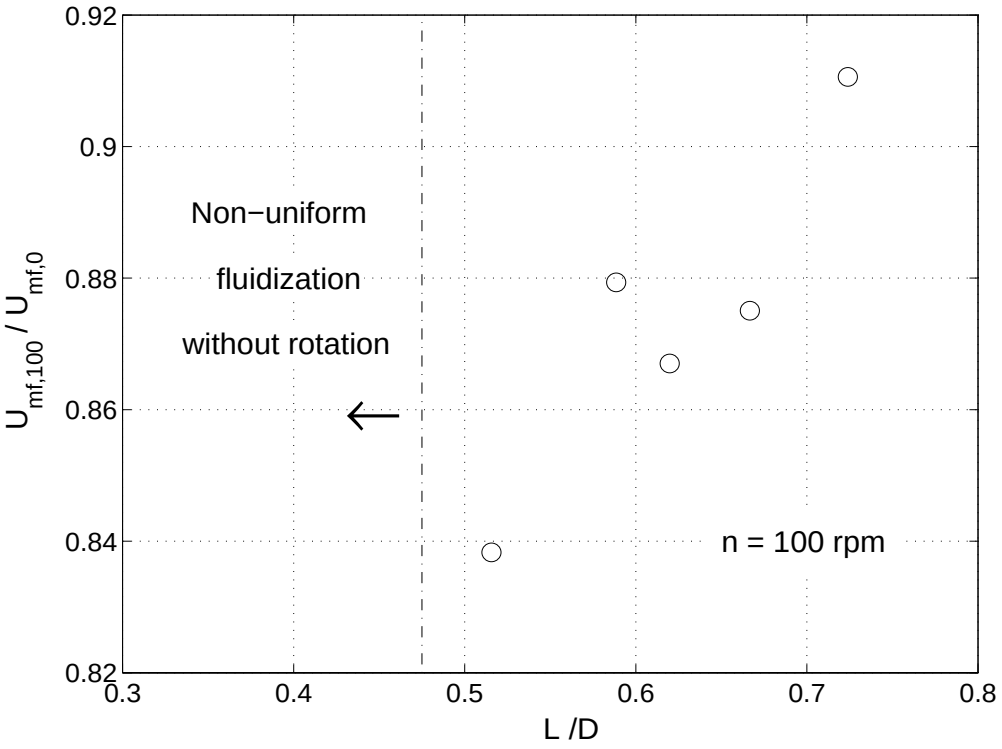

Figure 4.11: $U_{mf}/U_{mf,0}$ relation against non-dimensional bed height for a distributor rotational speed $n = 100$ rpm.

(b) If $\omega R_m \sim U$ the same fluidization quality is found not depending on the rotational speed.

(c) If $\omega R_m < U$ the effect of the plate rotation on the bed dynamics disappears due to the dominant influence of the axial gas velocity with respect to the tangential velocity caused by the the distributor rotation.

(d) The rotation of the distributor allows to fluidize very shallow bed which had a jet structure when the static distributor was used; the effect of the rotation becomes globally less important for deeper beds.

These characteristics show that adjusting the rotational speed it is possible to change the gas velocity needed to fluidized the bed, facilitating the fluidization and maintaining a uniform fluidization.
Further work could investigate the performance of the rotating distributor in Geldart A and C particles which are more difficult to fluidized. Moreover, similar experiments could be carried out encouraging the effect of the rotation by increasing the rotational speed above 100 rpm, or modifying the holes layout on the distributor.

Chapter 5

Determination of bubble characteristics using pressure and optical probes

The global characterization described in the previous chapter, is now completed by local measurements. In this chapter, a method to obtain the bubble characteristics is derived. Measurements are carried out using optical and pressure probes in a three-dimensional fluidized bed of Geldart B particles. The signals measured from two probes placed a short vertical distance apart are processed in order to calculate the bubble velocity and the pierced length. The velocity is obtained from the time lag between the two signals and the pierced length is calculated measuring the time the probe remains inside the bubble. This time, in the case of the differential pressure probes, is obtained according to Davidson's model.

The probability distributions (PDF) of bubble pierced length and velocity are obtained applying the Maximum Entropy Method. The relationship between the probability distribution of the bubble diameter and the raw moments of the experimentally measured pierced lengths is derived. Then the Maximum Entropy Method is applied to obtain the PDF of bubble diameter using the pierced length experimental data. It has been considered that there is a minimum bubble pierced length that it is possible to measure accurately using intrusive probes, due to their finite size. This lower limit, which is the distance between probes, s, has been introduced as a constraint in the derivation of the size distributions equations.

Results on bubble size obtained from pressure and optical probes have been found to be very similar, although optical probes provide more local information and can be used

at any position in the bed. The maximum entropy principle has been found to be a simple method that offers many advantages over other methods applied before for size distribution modeling in fluidized beds.

5.1 Introduction

Bubble characteristics, as bubble size, bubble shape, bubble ascending velocity and emulsion expansion are important parameters in the design and analysis of fluidized beds since they affect their performance as a reactor. As bubbles are not directly observable, there have been a number of techniques developed to study the bubble properties in fluidized beds, some of them reviewed by Cheremisinoff (1986), Yates and Simons (1994) or Werther (1999).

Non intrusive techniques such as X-ray (Kai et al., 2000) or magnetic resonance imaging (Müller et al., 2006) provide valuable information on bubbles in three-dimensional fluidized beds. However they are expensive and limited to small equipment. Moreover they exhibit a limited spatial or temporal resolution. Although disturbing the process to some degree, submerged probes are applicable to equipment and processes virtually of any size. Capacitance probes have been used in fluidized beds with some success (Werther and Molerus, 1973). However, they must be calibrated for every fluid-solid system and operating conditions, which is their main drawback.

Optical probes have been widely applied for the measurement of particle velocity and particle concentration in three-dimensional fluidized beds. Some of them have been adapted to detect the passage of bubbles (Ishida and Shirai, 1980; Hatano and Ishida, 1981). However the use of optical probes for the specific characterization of the bubble properties in three-dimensional fluidized beds is not so extensive. The operation is usually the same (Yasui and Johanson, 1958): two transmission probes are positioned one above the other spaced apart a variable short distance. The bubble rise velocity is estimated from the time lag between the signals from the two probes and their separation. The characteristic length associated with a bubble passage is calculated as the product of the bubble rise velocity and the time length of the light pulse transmitted by each bubble.

The interpretation of differential pressure measurements to determine the bubble parameters has received considerable attention because of its potential application in industrial fluidized beds. Sitnai (1982) first suggested the use of differential pressure measurements for the determination of bubble characteristics. He compared experimental measurements with simulated pressure gradient signals based on the theoretical pressure field around a

bubble in a fluidized bed according to Davidson's model (Davidson and Harrison, 1963). Dual probes have also been used to detect bubble passage in a gas sampling system by Littman and Homolka (1973) and in freely bubbling beds by Chan et al. (1987), Dent et al. (1989) and Ramaya et al. (1996).

One of the shortcomings of dual submergible probes is the interpretation of the signals as they give information on pierced length rather than characteristic diameter. This conversion is not straightforward, since the probes do not always intersect the bubble at its center, the assumption of vertical bubble rise from the lower to the upper probe tips is also to be considered and also the shape of the bubble has to be taken into account. This problem may be aggravated by the fact that bubbles may be disturbed as they pass the probe to a great or a lesser extent, depending on its design (Rowe and Masson, 1981).

The methods used to determine size distribution in multiphase flows can be classified as parametric, non-parametric and semi-parametric methods. Lee et al. (1990); Liu and Clark (1995) and Clark et al. (1996) applied parametric methods to estimate the bubble size distribution from measurements (typically Gamma, Rayleigh or LogNormal). Then the bubble size distribution can be inferred by a backward transformation (Herringe and Davis, 1976; Liu and Clark, 1995; Clark et al., 1996) or by an optimization problem (Lee et al., 1990). The main advantage of these methods is that they provide a bubble size distribution in closed form, however they need to assume a probability distribution function for the pierced length data a priori. If non-parametric methods are used the probability density function does not need to be established beforehand. Clark and Turton (1988); Turton and Clark (1989); Liu and Clark (1995); Liu et al. (1996., 1998) and Santana and Macías-Machín (2000) employed this type of methods. The main disadvantage of non-parametric methods is that the bubble size distribution obtained is not in a closed form.

(Santana et al., 2006) applied a semi-parametric approach based on the maximum entropy principle to estimate the bubble size, area and volume distributions requiring only the moments inferred from the measurements given by a sampling probe. In the present work the Maximum Entropy Method is used to characterize bubble size and velocity in fluidized beds for the first time and any truncated spheroidal geometry is considered. Moreover the method is modified in order to introduce the effect of the sampling probe. Due to the finite size of the probe it is not possible to measure pierced lengths smaller than the probe size. This fact has an important effect that must be taken into account in the estimation of the bubble size distributions.

The main advantages of the proposed method is that the distribution shape does not have

to be pre-established, the number of samples required is lower than in other methods and the backward transformation procedure is avoided. Moreover, although the distribution should match a certain number of moments obtained from the experimental measurements, the number of moments required does not need to be known a priori.
The first objective of this chapter is to compare the performance of a plastic dual optical fiber probe operating in the reflection mode (Vázquez et al., 2007) and a dual differential pressure probe for the determination of bubble velocity and pierced length in bubbling fluidized beds. The range of applicability of each technique for inferring bubble size distribution from the probe signals is analyzed. The signal processing needed to obtain bubble properties from the pierced time duration and the time lag between probes is explained. The second objective is to apply the methodology developed by (Santana et al., 2006) for the conversion of pierced length into bubble diameter using the semi-parametric approach based on the maximum entropy distribution estimation into a freely bubbling fluidized bed.

5.2 Experiments

Experiments were carried out in a bubbling fluidized bed of 0.193 m ID. and 0.8 m height. The bed was filled with Geldart B silica sand particles with a mean diameter of 680 μm and a density of 2632.5 kg/m^3.The settled bed height was 22 cm. The column had a perforated plate to distribute the air with 90 holes of 2 mm diameter laid out in hexagonal pitch of 15 mm. The total open area ratio of the distributor was 1%.
Pressure and optical probe measurements had a duration of 10 min and the sample frequency was 500 Hz. The data were recorded with a 12 bits data acquisition board (ICP DAS PCI-1802H) assembled in a PC. Optical probes developed for this study are based on backscattering principle.

5.2.1 Pressure probes

Gauge pressure measurements were carried out using piezoresistive differential pressure transducers Omega PX 291 (0-5 in H_2O) with a 1% FS accuracy. The high pressure port was connected to a probe immersed in the bed and the low pressure port was exposed to atmosphere. The pressure measurement accuracy was approximately $\pm$12 Pa.
Three pressure probes of 4 mm external diameter were located at the bed axis opposed

to the flow direction with the probe tip at a distance of 12 cm, 13 cm and 14 cm from the distributor. Pressure probes had to be positioned in the axis direction to enhance the transmission of the pressure signals what was a requirement for a subsequent signal analysis. No mesh was installed at the pressure probe tip since it was found to dampen the signal. For this reason a probe diameter of 4 mm had to be chosen to prevent particles to clog the probe. The vertical position of the probe prevented from particles getting to the transducer. The three probes were positioned tangentially (Fig. 5.1(b) left) because although a triangular configuration (Fig. 5.1(b) right) presents a lower eccentricity between probes it hinders the reception of the pressure signal due to the presence of the other two probes.

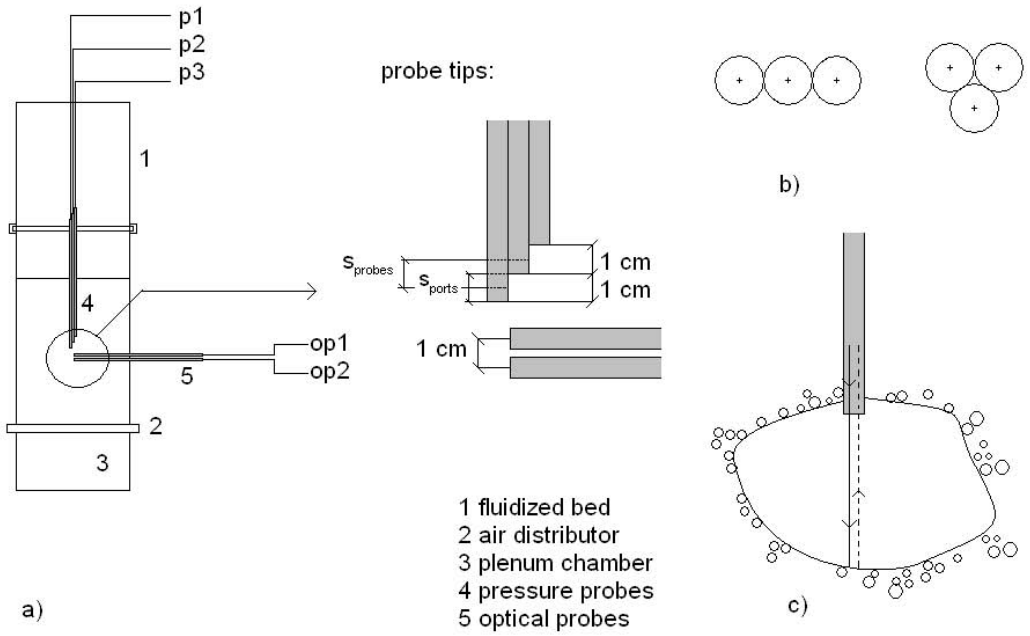

Figure 5.1: (a) Experimental set-up. (b) Pressure probes configuration. (c) Optical probe light reflected by the particle phase.

5.2.2 Optical probes

In-house developed optical probes were also used in the experiments. Two probes were placed at the bed axis but positioned along the radial direction and at a distance of 10 cm and 11 cm from the distributor. Optical probes were located 1 cm below the pressure probe bundle to avoid the interference in the optical probe light. An schematic of the set

up is shown in Fig. 5.1(a). The optical fiber probes (OFP) were made of two standard step-index plastic optical fibers (emitter and receiver fibers) embedded in a metallic coil of 3 mm external diameter for avoiding bending influences. The fibers had a diameter of 1 mm with 0.22 dB/m attenuation and 0.47 NA. The propagation delay constant of the fiber was 5 ns/m and the whole probe had a length of about 1m. The diameter of the fiber was larger than the particle size and smaller than the bubble characteristic size, thus these fibers are suitable for measuring both voidage and bubble parameters (Liu and Clark, 1995). The emitter fiber was illuminated by a 650nm laserdiode with a maximum power of 10mW (Roithner s6510mg) and a phototransistor was used at the reception, both encapsulated in ST connectors. A 50/50 passive splitter is used for splitting the optical power into the emitter fibers of both probes. The optical probes are suitable for operating temperature from -40 to 85℃. Fig. 5.2 presents the experimental reflective curve for the developed optical probe. The power ratio is expressed in percentage and it is the power of the light captured by the receiving fiber divided by that delivered by the projecting fiber. This curve has been calculated positioning a white surface at increasing distances from the probe tip. From Fig. 5.2, it is possible to specify limits of the penetration depth. For a distance of 5 mm the signal intensity falls about a 10% its maximum value, hence this may be considered to represent the outer limit of the measuring volume of the probe (Liu et al., 2003). The optical probes have to be placed perpendicular to the flow to preclude the light reflected at the bottom of the bubble from affecting the determination of the time instant the probe leaves the bubble (see Fig. 5.1(c)), what would make more difficult to distinguish between bubble and emulsion phase in the subsequent signal processing.

5.3 Signal processing

5.3.1 Pressure signal

The differential pressure signal has been widely proposed as a useful method to study bubble properties in fluidized beds (Dent et al., 1989; Sitnai, 1982; Ramaya et al., 1996). Several authors (Littman and Homolka, 1973; Sitnai, 1982; Ramaya et al., 1996) have proved that Davidson's model (Davidson and Harrison, 1963) represents well the pressure field around a rising bubble in a fluidized bed. Sitnai (Sitnai, 1982) also noted that knowledge of the precise details of the pressure field is not essential for the determination of the main bubble parameters. Indeed the dominant features of the real pressure field are

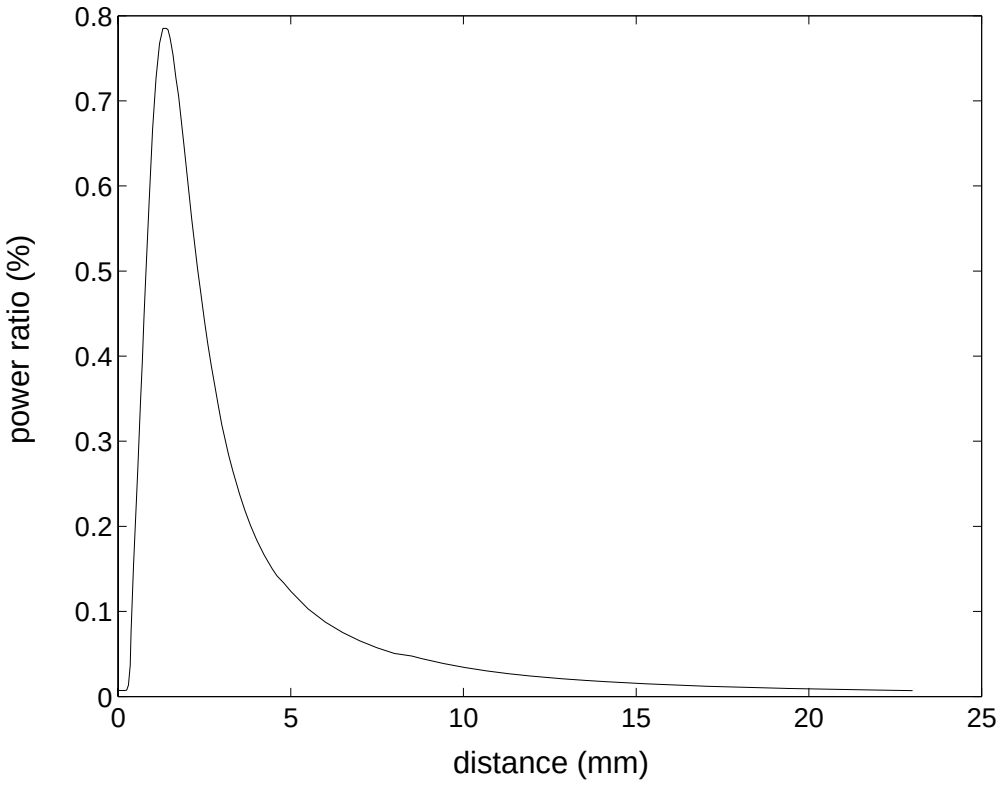

Figure 5.2: Reflective curve of the optical fiber probe.

a negligible pressure gradient inside the bubble and high recovery gradients at the bubble nose and tail. Fig. 5.3 shows the pressure distribution around a bubble resulting from Davidson's model. The normalized differential pressure is plotted against time. The solid line in Fig. 5.3 is the differential pressure p_{dif1} that has been obtained subtracting the the gauge pressure at the middle port p_2, from the gauge pressure p_1 at the lower pressure port. The dash line is the differential pressure p_{dif2} that has been obtained subtracting the gauge pressure at the upper port, p_3, from p_2. Care must be taken to keep the same dead volume in the three pressure lines (Clark and Atkinson, 1988), otherwise signals are generally spurious and as much dependent on global fluctuations in the bed as on local differential pressures. Other authors (Sitnai, 1982; Dent et al., 1989; Ramaya et al., 1996) have installed two pairs of pressure probes one above the other and connected each pair to a differential pressure transducer. On the contrary, for the configuration chosen here, the distance between probes s and the distance between ports, s_{ports} are necessarily equal (see Fig. 5.1(a)). Nevertheless this configuration has the advantage of requiring only three pressure probes to be immersed in the bed.

The bubble ascending velocity, u_b, and the bubble pierced length, y, can be determined

from differential pressures measurements. In Fig.5.3 it can be observed that at t_1 the bubble nose reaches the lower pressure port while at t_2 the bubble reaches the upper one. Hence bubble velocity can be calculated as:

$$u_b = \frac{s}{t_u} \tag{5.1}$$

where t_u is the time lag $t_2 - t_1$.
The time period between the two instants where the pressure gradient curve crosses the reference line (labeled t_y in Fig. 5.3) was approximated by Sitnai (Sitnai, 1982) as equivalent to the ratio of bubble pierced length to its rise velocity (y/u_b). Therefore the bubble pierced length may be computed as:

$$y = u_b \cdot t_y \tag{5.2}$$

It can be easily deduced from Eq. (5.1) that the relative error of the calculated velocity is mainly given by:

$$e_{u_b} = \frac{\Delta u_b}{u_b} = \frac{\Delta t}{t_u} = \frac{u_b}{s} \cdot \Delta t \tag{5.3}$$

where $\Delta t = 0.002$ s, is the time between samples.
The relative error of y can be deduced from Eq. (5.2):

$$e_y = \Delta t(\frac{1}{t_u} + \frac{1}{t_y}) = \frac{u_b}{s} \cdot \Delta t + \frac{u_b}{y}\Delta t \tag{5.4}$$

This error analysis shows that a higher distance between pressure probes minimizes the error in the calculation of bubble velocity. However, if this distance is too high it may happen that the bubble does not cross both pressure probes when it rises. Therefore, there must be a compromise between those parameters. In the present work a separation between probes $s = 1$ cm has been chosen. It can also be deduced from Eq. (5.4) that if $y < s$ the second term in the equation dominates over the first one; the relative error of y, e_y, increases when y decreases. For this reason pierced length measurements smaller than s have not been considered reliable.
An example of the differential pressure measured in the bed is shown in Fig. 5.4(a). Bubble velocity could therefore be determined from the time delay between the two differential pressure signals. However, Werther (Werther, 1974b) showed that the instantaneous velocity of a bubble is a stochastic quantity, thus, it is convenient to divide the signal in time

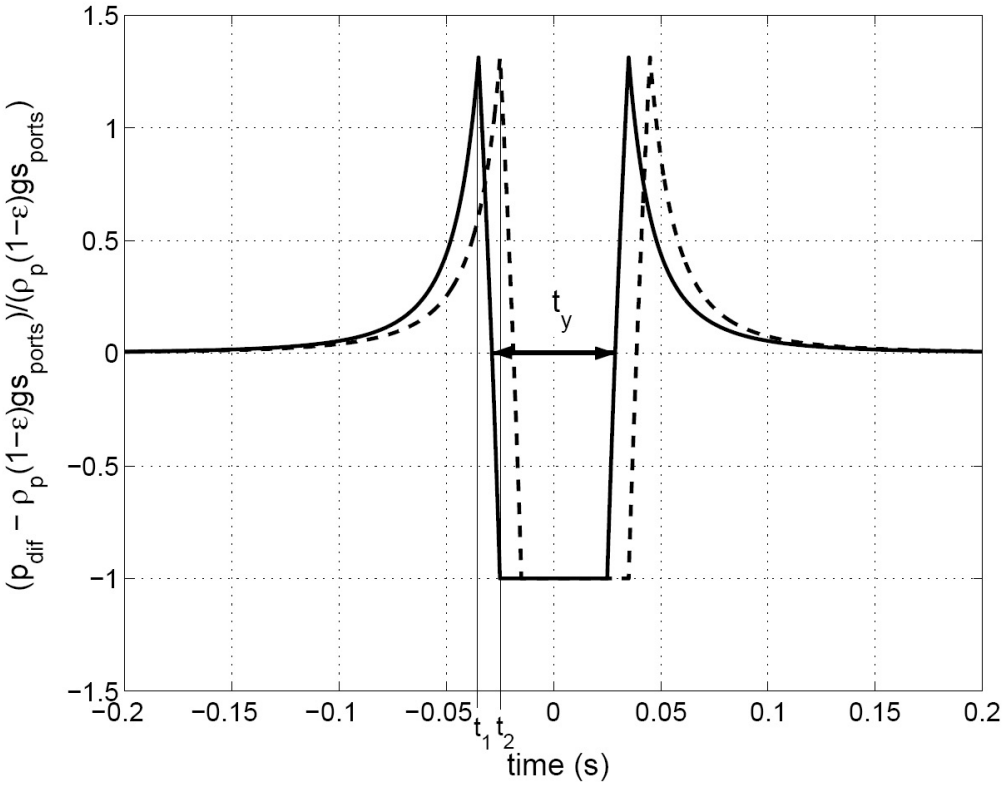

Figure 5.3: Pressure field around a rising bubble. Solid line: p_{dif1}, dash line: p_{dif2}

portions and treat each bubble independently. In this way the velocity of the demarcated bubble is obtained by applying correlation techniques only over the length of the signal corresponding to an individual bubble (Ghadiri et al., 1988).

The first criterion that must be fulfilled in order to detect a bubble presence is that p_{dif1} and p_{dif2} fall below their mean value $(\rho_p g(1-\epsilon)s_{ports})$ and approach zero. A further criterion has been used to reject bubbles rising with an horizontal eccentricity greater than the bubble radius, in which case the record differential pressure falls half of its average value (Dent et al., 1989; Sitnai, 1982). In Fig. 5.4(a) bubbles detected following these criteria are marked with an arrow.

Once the bubble is detected, bubble velocity is obtained from the cross correlation of the differential pressure signals (Sitnai, 1982) as shown in Fig.5.5(b). The cross correlation is computed in the time interval spanning from the first maximum of p_{dif1} to the second maximum of p_{dif2} (Fig. 5.5(a)). The maximum of the cross correlation occurs for a time s/u_b. Once the bubble velocity u_b has been obtained it can be used to determine the bubble pierced length y, which also depends on the time interval t_y. This time interval has been obtained from the raw signal (Ramaya et al., 1996) as shown in Fig. 5.5(a).

p_{dif1} has been chosen to perform this calculation since the bubble distortion caused by the probe is weaker at this moment.

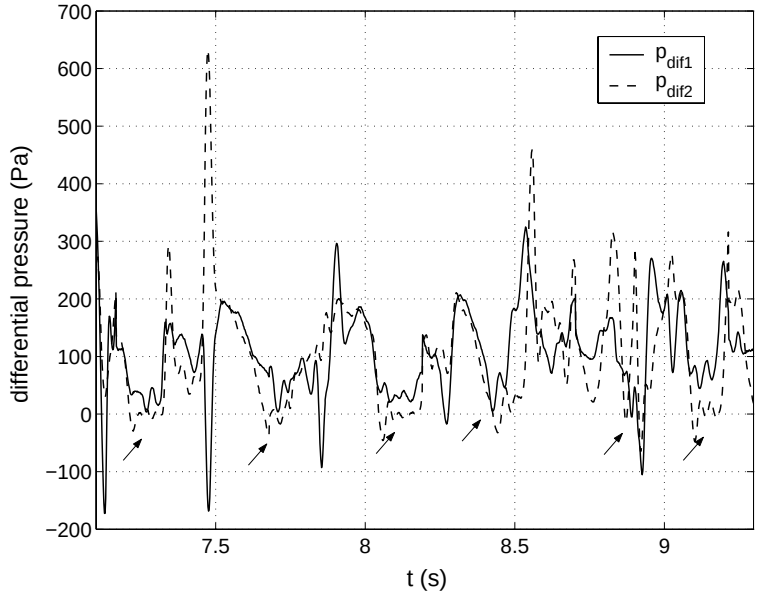

(a)

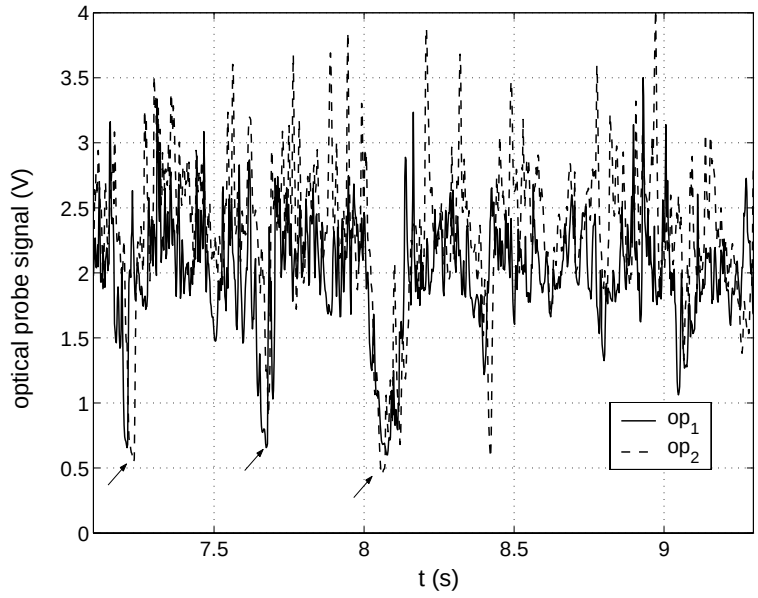

(b)

Figure 5.4: (a) Differential pressure signals p_{dif1} and p_{dif2}. (b) Optical probes signals op_1 and op_2. Bubble passages are marked with arrows.

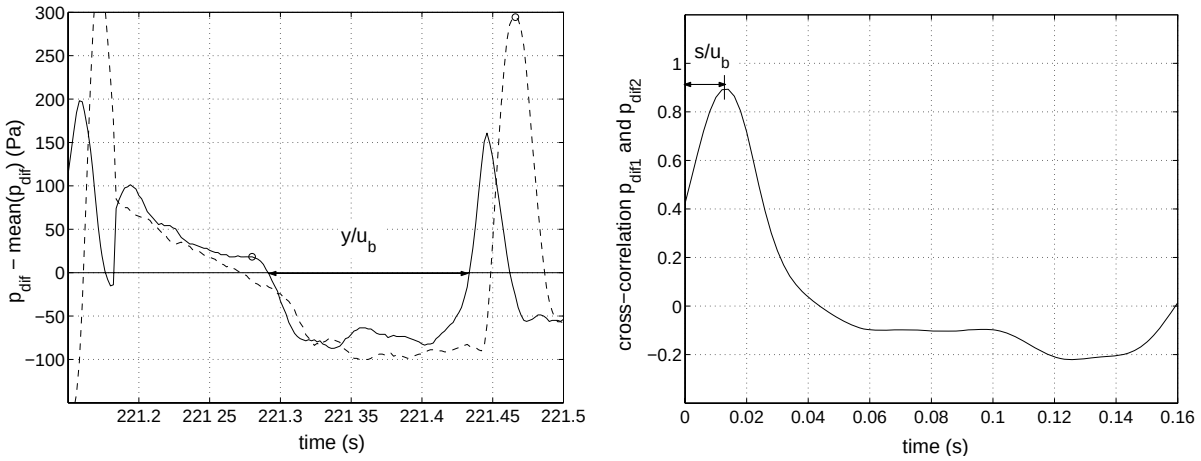

(a) (b)

Figure 5.5: (a) Differential pressure signals p_{dif1} and p_{dif2} (b) Cross correlation of the differential pressure signals. The cross correlation was computed for the time interval marked with circles.

5.3.2 Optical probe signal

A similar procedure is used to calculate bubble characteristics from optical probe signals. Fig. 5.4(b) shows an example of the raw signal measured by optical probes op_1 and op_2. When a bubble passes in front of the probe the reflected light is lower than the reflected light by the emulsion phase (high concentration of particles) and the voltage falls rapidly. In order to come up with a bubble detection criterion for the optical probe signal processing, it is needed to set a threshold voltage (bubble detection threshold), below which it is considered a bubble passage is occurring. This threshold can be determined by plotting the histogram of the output voltage from optical probes (Schweitzer et al., 2001). Fig. 5.6 shows an example. It exhibits a peak corresponding to emulsion-phase responses at voltage around 2 V and a tail at lower voltages corresponding to gas bubbles. The bubble detection threshold has been defined as the voltage where the histogram tail begins, i.e. where the slope of the histogram becomes nearly zero. Bubbles detected following this criterion are marked with an arrow in Fig. 5.4(b) .When two bubbles are very close it is subjective whether to consider them as one or two bubbles. The assignment of the bubble boundary location is also subjective due to the high void fraction region at the boundary and the relatively large particle content inside the bubbles (Mainland and Welty, 1995). In the present work, the mean value of the signal has been considered an appropriate threshold to demarcate the bubble length (bubble length threshold), since bubble properties are not overly sensitive to this value.

Signals op_1 and op_2 were correlated in order to calculate bubble velocity as explained for the pressure signals (Fig. 5.7(b)). The time interval where the cross correlation was computed was that part of the signal between maxima found just before and after the bubble boundaries, where the signal begins to fall abruptly. The piercing time ,t_y, is the time during which the probe is immersed into the bubble. It has been calculated from the lower probe signal as the time interval between the two instants where the signal crosses its mean value (see Fig. 5.7(a)).
There are bubbles that are detected by the pressure probes but not by the optical probes

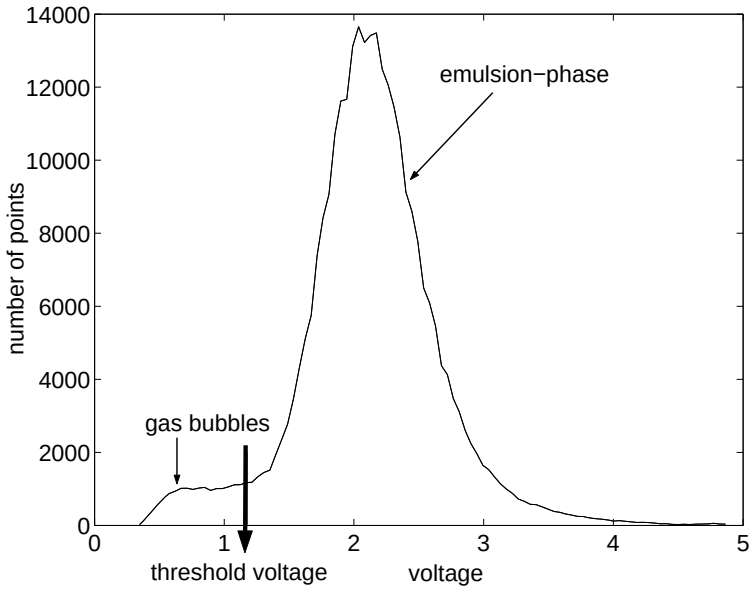

Figure 5.6: Optical signal histogram.

since they do not meet the detection criterion. This occurs because optical probes provide more local measurements and they do not detect a bubble unless the measuring volume is to some degree free of particles

5.4 Modeling of the bubble size distribution using the Maximum Entropy Method

In this section the Maximum Entropy Method is used to obtain the probability density function (PDF) of the bubble velocity, bubble pierced length and bubble size from experimental measurements of the bubble pierced length and bubble velocity (Jaynes, 1957).

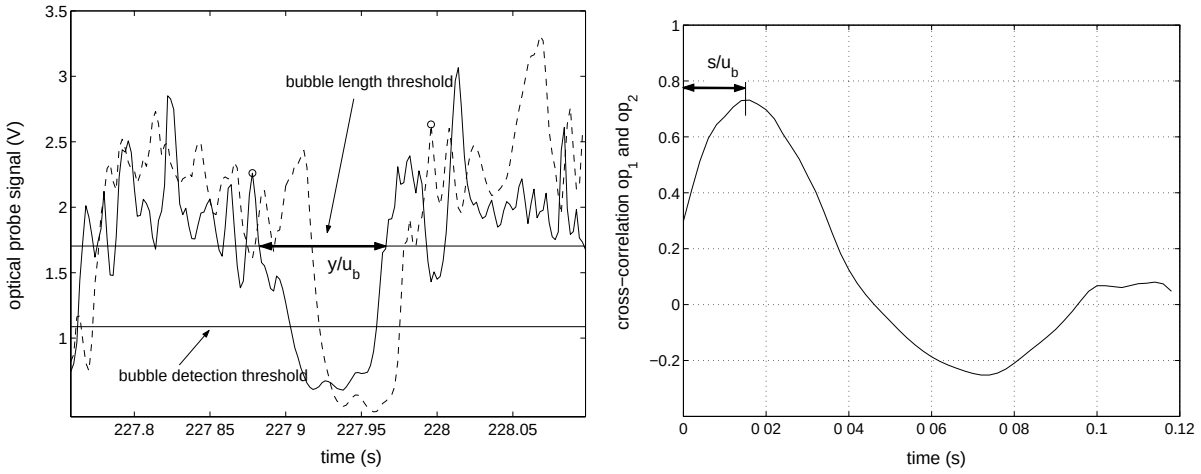

(a) (b)

Figure 5.7: (a) Optical probe signals op_1 and op_2. (b) Cross correlation of the optical probe signals. The cross correlation was computed in the time interval marked with circles.

5.4.1 Maximum Entropy Method

Santana et al. (2006) applied the entropy principle of Shannon to obtain the bubble size, surface and volume distributions in bubbly flows from the moments inferred from pierced length measurements. Intuitively, this method consists in, given a collection of constraints that an objective function has to satisfy, choosing a function which is consistent with all the constraints, but otherwise being as uniform as possible. In other words, model all that is known and assume nothing about what is unknown. Following the formulation of Sellens and Brzustowski (1985) the probability distribution is the function that maximizes the Shanon entropy

$$\begin{aligned} &\max_{P(x)} \int_{x\in\Delta} -P(x)ln(P(x))dx \\ &\text{constrained to } \int_{x\in\Delta} f_i(x)P(x)dx = \langle f_i \rangle \quad i = 1, 2, ...n. \\ &\text{and also constrained to the normalization condition } \int_{x\in\Delta} P(x)dx = 1 \end{aligned} \tag{5.5}$$

When the entropy is maximum, subjected to the constraints, the resulting $P(x)$ is the least biased distribution which satisfies the physics embodied in the constraints.

5.4.2 Size and velocity estimation using the maximum entropy method

The Maximum Entropy Method can be used to determine the probability density function of bubble pierced lengths, bubble diameter and bubble velocity. The problem to be solved for the PDF of bubble pierced length estimation is

$$\begin{aligned} &\max_{P(y)} \int_{y\in\Delta} -P(y)ln(P(y))dy \\ &\quad \text{s.t} \quad \int_{y\in\Delta} y^i P(y)dy = \langle y^i \rangle \quad i = 1, 2, ...n. \\ &\qquad \int_{y\in\Delta} P(y)dy = 1 \end{aligned} \tag{5.6}$$

and for the PDF of bubble velocity is

$$\begin{aligned} &\max_{P(u_b)} \int_{u_b\in\Delta} -P(u_b)ln(P(u_b))du_b \\ &\quad \text{s.t} \quad \int_{u_b\in\Delta} u_b^i P(u_b)du_b = \langle u_b^i \rangle \quad i = 1, 2, ...n. \\ &\qquad \int_{u_b\in\Delta} P(u_b)du_b = 1 \end{aligned} \tag{5.7}$$

The raw sample moments $\langle y^i \rangle$ and $\langle u_b^i \rangle$ are directly obtained from the measurements. A similar procedure could be used to calculate the PDF of bubble diameter

$$\begin{aligned} &\max_{P(D)} \int_{D\in\Delta} -P(D)ln(P(D))dD \\ &\quad \text{s.t} \quad \int_{D\in\Delta} D^i P(D)dy = \langle D^i \rangle \quad i = 1, 2, ...n. \\ &\qquad \int_{D\in\Delta} P(D)dD = 1 \end{aligned} \tag{5.8}$$

Unfortunately, the raw moments of the bubble diameter are not known and they must be estimated from pierced length measurements.

5.4.3 Estimation of the probability distribution of bubble diameter from pierced length raw moments

In this section it will be explained how to calculate an estimation of the sample raw moments of the bubble diameter distribution using the raw moments of the pierced length distribution. The bubble geometry (Fig. 5.8) considered in the following formulation will be the most general one: a truncated oblate spheroidal (an ellipsoid having two equal principal axis). This geometry has axial symmetry and then there is not a dependance on the azimuthal angle. The pierced length PDF can be obtained assuming that bub-

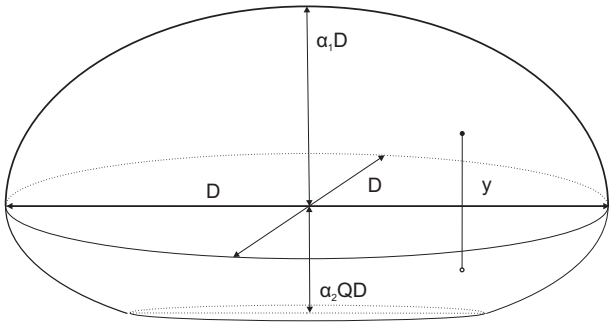

Figure 5.8: Schematic of the truncate oblate ellipsoidal bubble

bles will rise randomly distributed in a horizontal circular surface containing the probe (Werther, 1974b). Furthermore it was found by Santana et al. (2006) that considering the general case where the bubble velocity vector forms a certain angle of attack with the vertical direction, the errors in the angle of attack produce a negligible effect on the PDF estimation, therefore the ascending velocity will be considered vertical in the following formulation. Provided the bubble touches the probe and taking into account that pierced lengths smaller than the distance between probes (s) can not be measured, the maximum distance between the probe tip and the bubble symmetry axis that allows the bubble to be measured is, as shown in Fig. 5.9

$$r_{max,s} = \begin{cases} \sqrt{\left(\frac{D}{2}\right)^2 - \left(\frac{s - \alpha_2 Q \frac{D}{2}}{\alpha_1}\right)^2} & s > (\alpha_1 + \alpha_2)\frac{D}{2}Q \\ \sqrt{\left(\frac{D}{2}\right)^2 - \left(\frac{s}{\alpha_1 + \alpha_2}\right)^2} & s < (\alpha_1 + \alpha_2)\frac{D}{2}Q \end{cases} \tag{5.9}$$

Subindex s in $r_{max,s}$ has been used to mark that this is the maximum distance between the probe tip and the bubble centre for bubbles with pierced lengths larger than the distance between probes, s. This subindex will be used with this meaning hereafter.
Since it has been assumed that the distance between the probe and the bubble symmetry axis, r, follows a uniform distribution, its cumulative distribution function is given by

$$F_s(r|D,\alpha_1,\alpha_2,Q) = \frac{r^2}{r_{max,s}^2} \quad ; \quad r \in (0, r_{max,s}) \tag{5.10}$$

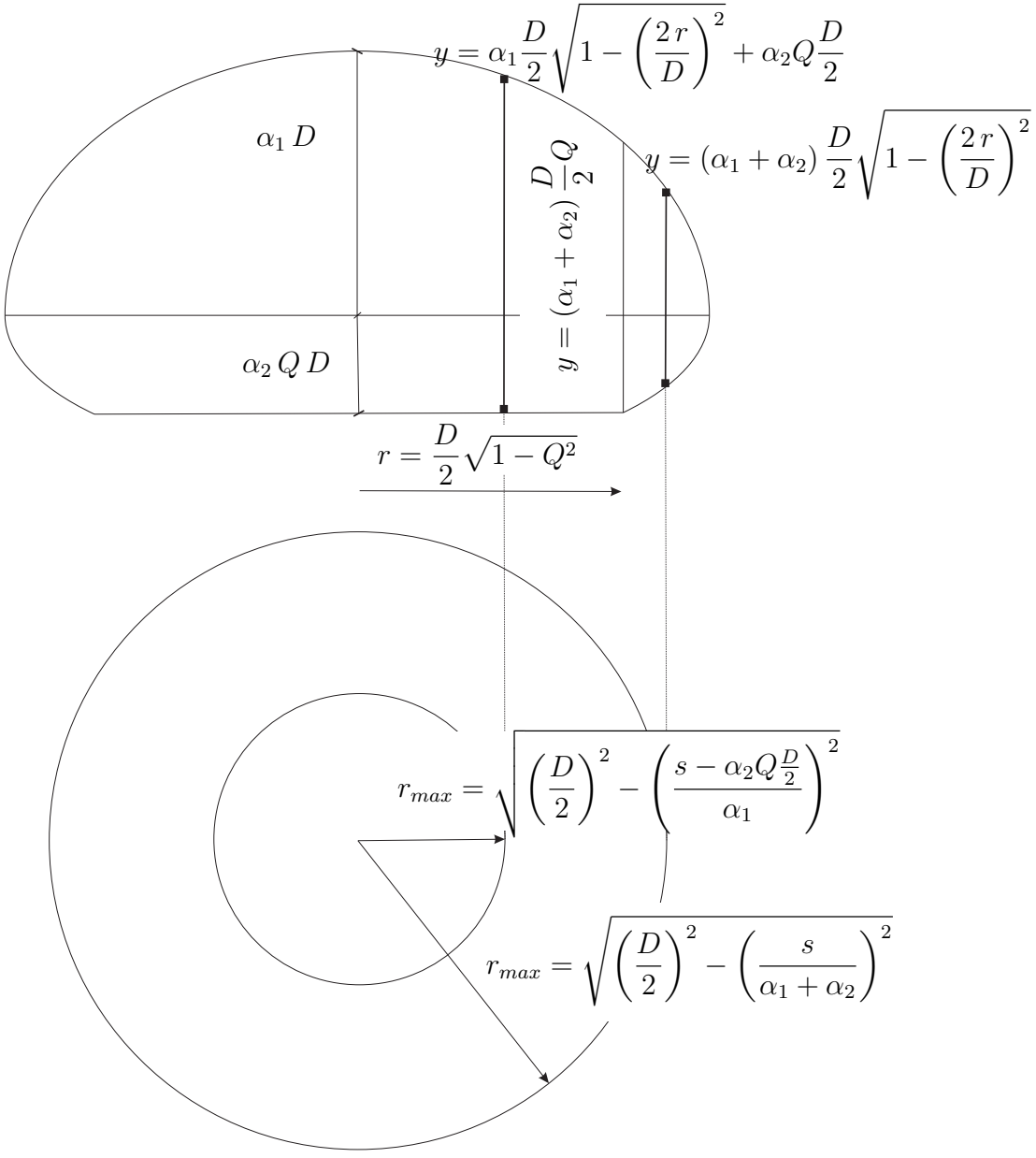

Figure 5.9: Vertical section of the truncated ellipsoidal bubble.

Deriving this equation the probability density function (PDF) of the distance r between the probe and the bubble center for a given bubble diameter D is obtained:

$$P_s(r|D,\alpha_1,\alpha_2,Q) = \begin{cases} \dfrac{2r}{\left(\dfrac{D}{2}\right)^2 - \left(\dfrac{s}{\alpha_1+\alpha_2}\right)^2} & D \le \dfrac{2s}{(\alpha_1+\alpha_2)Q}; \qquad r \in (0, r_{max}) \\ \dfrac{2r}{\left(\dfrac{D}{2}\right)^2 - \left(\dfrac{s-\alpha_2 Q\frac{D}{2}}{\alpha_1}\right)^2} & D > \dfrac{2s}{(\alpha_1+\alpha_2)Q}; \qquad r \in (0, r_{max}) \end{cases} \tag{5.11}$$

The pierced length measured by the probe is the distance between the points where the probe intersect the bubble surface in its ascension, and is given by (see Fig. 5.9)

$$y = \begin{cases} \alpha_1 \dfrac{D}{2}\sqrt{1-\left(\dfrac{2r}{D}\right)^2} + \alpha_2 Q\dfrac{D}{2} & 0 \le 2r \le D\sqrt{1-Q^2} \\ (\alpha_1+\alpha_2)\dfrac{D}{2}\sqrt{1-\left(\dfrac{2r}{D}\right)^2} & D\sqrt{1-Q^2} \le 2r \le D \end{cases} \tag{5.12}$$

Then the following statistical property can be used

$$P_s(y|D,\alpha_1,\alpha_2,Q) = P_s(r|D,\alpha_1,\alpha_2,Q)\left|\frac{dr}{dy}\right| \tag{5.13}$$

where

$$\left|\frac{dy}{dr}\right| = \begin{cases} \dfrac{\alpha_1^2 r}{y - \alpha_2 Q\dfrac{D}{2}} & 0 \le 2r \le D\sqrt{1-Q^2} \\ \dfrac{(\alpha_1+\alpha_2)^2 r}{y} & D\sqrt{1-Q^2} \le 2r \le D \end{cases} \tag{5.14}$$

Then if the bubble diameter is known the PDF of pierced lengths can be obtained as following

$$P_s(y|D,\alpha_1,\alpha_2,Q) = \begin{cases} D \leq \dfrac{2s}{(\alpha_1+\alpha_2)Q} \begin{cases} \dfrac{2\left(y-\alpha_2 Q\dfrac{D}{2}\right)}{\alpha_1^2\left[\left(\dfrac{D}{2}\right)^2-\left(\dfrac{s-\alpha_2 Q\dfrac{D}{2}}{\alpha_1}\right)^2\right]}; \\ (\alpha_1+\alpha_2 Q)\dfrac{D}{2} \geq y \geq s \end{cases} \\ D > \dfrac{2s}{(\alpha_1+\alpha_2)Q} \begin{cases} \dfrac{2\left(y-\alpha_2 Q\dfrac{D}{2}\right)}{\alpha_1^2\left[\left(\dfrac{D}{2}\right)^2-\left(\dfrac{s}{\alpha_1+\alpha_2}\right)^2\right]}; \\ (\alpha_1+\alpha_2 Q)\dfrac{D}{2} \geq y \geq (\alpha_1+\alpha_2)Q\dfrac{D}{2} \\ \dfrac{2y}{(\alpha_1+\alpha_2)^2\left[\left(\dfrac{D}{2}\right)^2-\left(\dfrac{s}{\alpha_1+\alpha_2}\right)^2\right]}; \\ (\alpha_1+\alpha_2)Q\dfrac{D}{2} \geq y \geq s \end{cases} \end{cases} \tag{5.15}$$

The raw moment of order i of the pierced length y can be calculated applying the total probability theorem

$$\langle y^i|\alpha_1,\alpha_2,Q\rangle = \int_s^\infty y^i P_s(y|\alpha_1,\alpha_2,Q)dy = \int_s^\infty y^i \int_{\frac{2y}{\alpha_1+\alpha_2 Q}}^\infty P_s(y|D,\alpha_1,\alpha_2,Q)P_s(D|\alpha_1,\alpha_2,Q)dDdy \tag{5.16}$$

The lower limit of the last integral in Eq. (5.16) is the minimum diameter D_{min} that is possible to obtain provided the minimum measurable pierced length is s. Inverting the

integral limits and introducing Eq. (5.15) in the above expression

$$\langle y^i|\alpha_1,\alpha_2,Q\rangle = \int_{\frac{2s}{\alpha_1+\alpha_2Q}}^{\frac{2s}{(\alpha_1+\alpha_2)Q}}\int_{s}^{(\alpha_1+\alpha_2Q)\frac{D}{2}} \frac{y^i 2\left(y-\alpha_2Q\frac{D}{2}\right)}{\alpha_1^2\left[\left(\frac{D}{2}\right)^2-\left(\frac{s-\alpha_2Q\frac{D}{2}}{\alpha_1}\right)^2\right]}dyP_s(D|\alpha_1,\alpha_2,Q)dD+$$
$$+\int_{\frac{2s}{(\alpha_1+\alpha_2)Q}}^{\infty}\int_{s}^{(\alpha_1+\alpha_2)Q\frac{D}{2}} \frac{2y^{i+1}}{(\alpha_1+\alpha_2)^2\left[\left(\frac{D}{2}\right)^2-\left(\frac{s}{\alpha_1+\alpha_2}\right)^2\right]}dyP_s(D|\alpha_1,\alpha_2,Q)dD+$$
$$+\int_{\frac{2s}{(\alpha_1+\alpha_2)Q}}^{\infty}\int_{(\alpha_1+\alpha_2)Q\frac{D}{2}}^{(\alpha_1+\alpha_2Q)\frac{D}{2}} \frac{y^i 2\left(y-\alpha_2Q\frac{D}{2}\right)}{\alpha_1^2\left[\left(\frac{D}{2}\right)^2-\left(\frac{s}{\alpha_1+\alpha_2}\right)^2\right]}dyP_s(D|\alpha_1,\alpha_2,Q)dD \quad (5.17)$$

The first term can be neglected in the calculation of the above integrals obtaining:

$$\frac{i+2}{2}\langle y^i|\alpha_1,\alpha_2,Q\rangle = \int_{\frac{2s}{\alpha_1+\alpha_2Q}}^{\infty} \frac{\left(\frac{D}{2}\right)^{i+2}S_i - s^{i+2}}{(\alpha 1+\alpha_2)^2\left(\left(\frac{D}{2}\right)^2-\left(\frac{s}{\alpha_1+\alpha_2}\right)^2\right)}P_s(D|\alpha_1,\alpha_2,Q)dD \quad (5.18)$$

where

$$S_i = \frac{(\alpha_1+\alpha_2)^{i+2}}{(i+1)\alpha_1^2}\left[Q^{i+2}\alpha_2(\alpha_2-i\alpha_1)+\frac{(\alpha_1+Q\alpha_2)^{i+1}}{(\alpha_1+\alpha_2)^i}(\alpha_1(i+1)-\alpha_2Q)\right] \quad (5.19)$$

It has been explained that the estimation of the distribution $P_s(D)$ has been made considering that only pierced lengths larger than the distance between probes ($y > s$) could be measured by the probes. In other words, $P_s(D)$ in Eq. (5.18) is the diameter distribution of the bubbles that get immersed in both probes in their ascension. Then Bayes theorem is applied to obtain the PDF of D, $P(D)$,

$$P(D_s|D) = P(D|D_s)\frac{P_s(D)}{P(D)} \quad (5.20)$$

where

$$P(D|D_s) = 1$$
$$P(D_s|D) = \frac{D^2 - \left(\frac{2s}{\alpha_1+\alpha_2}\right)^2}{D^2} \tag{5.21}$$

Hence the following expression is obtained for $P(D)$:

$$\frac{i+2}{2}\langle y^i|\alpha_1,\alpha_2,Q\rangle = \int_{\frac{2s}{\alpha_1+\alpha_2 Q}}^{\infty} \frac{\left(\frac{D}{2}\right)^{i+2} S_i - s^{i+2}}{(\alpha_1+\alpha_2)^2\left(\frac{D}{2}\right)^2} P(D|\alpha_1,\alpha_2,Q)dD \tag{5.22}$$

where S_i is given in Eq. (5.19). The relation between D and the volume equivalent diameter D_v, which is the diameter of a sphere having the same volume is

$$\delta = \frac{D_v}{D} = \left(\frac{6V}{\pi}\right)^{1/3}\frac{1}{D} = \left(\frac{\alpha_2 Q(3-Q^2)+2\alpha_1}{4}\right)^{1/3} \tag{5.23}$$

Therefore an expression to estimate $P(D_v)$ can be deduced from Eq. (5.22)

$$\frac{i+2}{2}\langle y^i|\alpha_1,\alpha_2,Q\rangle = \int_{\frac{2s}{\alpha_1+\alpha_2 Q}}^{\infty} \frac{\left(\frac{D_v}{2}\right)^{i+2}\delta^{-\frac{i+2}{3}} S_i - s^{i+2}}{(\alpha 1+\alpha_2)^2\left(\frac{D_v}{2}\right)^2\delta^{-2/3}} P(D_v|\alpha_1,\alpha_2,Q)dD_v \tag{5.24}$$

5.4.4 Estimation of the bubble diameter distribution using the Maximum Entropy Method

It was explained in section 5.4.2 that the difficulty on applying the Maximum Entropy Method for the estimation of the bubble diameter distribution was to obtain the raw moments since the diameter can not be obtain experimentally. However an estimator for the raw moment of a function f of D_v was shown in Eq. (5.24). Therefore the problem to be solved to estimate the probability density function of bubble equivalent volume

diameter D_v using the maximum entropy method is

$$\begin{aligned} \max_{P(D_v)} & \int_{D_v \in \Delta} -P(D_v) ln(P(D_v)) dD_v \\ \text{s.t} & \int_{D_v \in \Delta} f_i P(D_v) dD_v = \langle f_i \rangle \quad i = 1, 2, ...n. \\ & \int_{y \in \Delta} P(D_v) dD_v = 1 \end{aligned} \tag{5.25}$$

It can be seen from Eq. (5.24) that

$$f_i = \frac{\left(\frac{D_v}{2}\right)^{i+2} \delta^{-\frac{i+2}{3}} S_i - s^{i+2}}{(\alpha_1 + \alpha_2)^2 \left(\frac{D_v}{2}\right)^2 \delta^{-2/3}} \tag{5.26}$$

An estimator for the raw moments of f_i using the experimental pierced length data was also found (see Eq. (5.24))

$$\langle f_i \rangle = \frac{i+2}{2} \langle y^i | \alpha_1, \alpha_2, Q \rangle \tag{5.27}$$

Santana et al. (2006) applied this method without considering the distance between probes s in the calculation of $P(y)$. They showed that in that case the resulting equation relates directly the raw moments of the diameter with the pierced length. Then the different moments of the bubble diameter can be obtained analytically from measured pierced lengths ($f_i = D^i$ in their work). It was shown in Eq. (5.22) that this does not happen when the distance s is taken into account, since the function f_i is a more complex function of D. Then the obtained $P(D)$ must be numerically integrated in order to obtain the different moments of the bubble diameter.

Shape factor

Werther (Werther, 1974a) showed how an elipsoidal bubble shape may be easily assimilated to another one with a shape similar to that of a spherical cap bubble without altering the maximum horizontal and vertical dimension of the bubble, nor its volume or the distribution of pierced lengths. Then, the parameters α_1 and α_2 have been chosen equal to 1. Werther (1976) also proposed a correlation for the shape factor ρ, which is

the ratio of the volume of the bubble to the volume of a sphere of the same diameter

$$\rho = (1 - 0.3 \exp\left[-8\left(U - U_{mf}\right)\right]) \exp(-\phi z) \tag{5.28}$$

$$\phi = 7.2(U - U_{mf}) \exp[-4.1(U - U_{mf})] \tag{5.29}$$

where h and $(U - U_{mf})$ are in m and m/s respectively. The shape factor for the geometry in Fig. 5.8 is

$$\rho = \frac{V}{V_v} = \frac{\alpha_2 Q(3 - Q^2) + 2\alpha_1}{4} \tag{5.30}$$

Setting $\alpha_1 = \alpha_2 = 1$ and using Eq. (5.28) and (5.29) the parameter Q can be calculated. It depends on the excess gas $U - U_{mf}$ and the height above the distributor z. An experimental determination of the actual bubble shape may be achieved with a four-point probe for gas-liquid systems (Luther et al., 2004) and the parameter Q will be measured for each bubble together with the pierced length.

5.4.5 Numerical implementation of the Maximum Entropy Method

Sellens and Brzustowski (1985) showed that the solution of the maximum entropy problem (Eq. (5.5)) is

$$P(x) = \exp\left(\lambda_0 + \sum_{i=1}^{n} \lambda_i f_i\right) \tag{5.31}$$

where λ_i is the Lagrange multiplier for the ith constraint.
Rockinger and Jondeau (2002) showed that the problem of calculating the Lagrangian multipliers reduces to the minimization of the potencial function

$$G(\lambda_1, \ldots, \lambda_n) = \int_{x \in \Delta} \exp\left(\sum_{i=1}^{n} \lambda_i \left(f_i - \langle f_i \rangle\right)\right) dx \tag{5.32}$$

i.e. the obtention of the zeros of the gradient vector g

$$g_i = \frac{\partial G}{\partial \lambda_i} = 0 \tag{5.33}$$

This problem can be solved applying Newton's method:

$$\lambda^{(k)} = \lambda^{(k-1)} - H^{-1}(\lambda^{(k-1)}) g(\lambda^{(k-1)}) \tag{5.34}$$

where λ is the vector of Lagrangian multipliers, g is the gradient vector

$$g_i = \frac{\partial G}{\partial \lambda_i} = \int_{x\in\Delta} (f_i - \langle f_i \rangle) P(x) dx \qquad i = 1, 2, ...n. \tag{5.35}$$

and H is the hessian matrix

$$H_{ij} = \frac{\partial^2 Q}{\partial \lambda_i \partial \lambda_j} = \int_{x\in\Delta} (f_i - \langle f_i \rangle)(f_j - \langle f_j \rangle) P(x) dx \qquad i, j = 1, 2, ...n. \tag{5.36}$$

To calculate the above integrals a Gaussian-Legendre quadrature rule was used:

$$\int_{-1}^{1} h(x) dx \approx \sum_{i=1}^{n} w_i h(x_i) \tag{5.37}$$

where w_i are the Gauss-Legendre weights. If the domain Δ is a finite interval [a,b] the change of variable $\xi = (2x - a - b)/(b - a)$ must be done before applying the quadrature rule resulting

$$\int_a^b h(x) dx = \frac{b-a}{2} \int_1^1 h\left(\frac{b-a}{2}\xi + \frac{a+b}{2}\right) d\xi \tag{5.38}$$

A 96-point Gaussian quadrature was used here (Santana et al., 2006).
The estimation of the maximum entropy distribution was started introducing the first two constraints, and the initial value for the iterative procedure in Eq. (5.34) was $\lambda^{(0)} = (0, 0)$. The convergence criterion to be fulfilled was $g(\lambda^{(k-1)}) \leq 10^{-6}$. Afterwards the other constraints are successively introduced. However, the Kullback-Leiber entropy discrepancy criterion was applied as explained by Santana et al. (2006). This criterion establishes that if the Kullback-Leibler discrepancy, Δ_{KL} given by

$$\Delta_{KL}(i) = \int_{\Delta} P_i(D) \log(P_i(D)/P_{i+1}(D)) dD \tag{5.39}$$

reaches a minimum value, distribution obtained introducing i constraints and $i + 1$ constraints are the same. The inclusion of a new constraint does not contribute to maximize the information content of the PDF but the errors. Thus the optimum distribution must be the maximum entropy distribution that fits the maximum number of moment constraints i and has the minimum Δ_{KL}.

5.5 Results and discussion

Probability density functions of bubble pierced length, velocity and diameter were obtained using the method described above. Results for pressure and optical measurements carried out using the experimental set-up shown in Fig. 5.1 are compared in Fig 5.10. The mean and standard deviation of y and D_v are summarized in Table 5.1.
It can also be observed in Fig. 5.10(a) that the PDF of pierced lengths obtained from

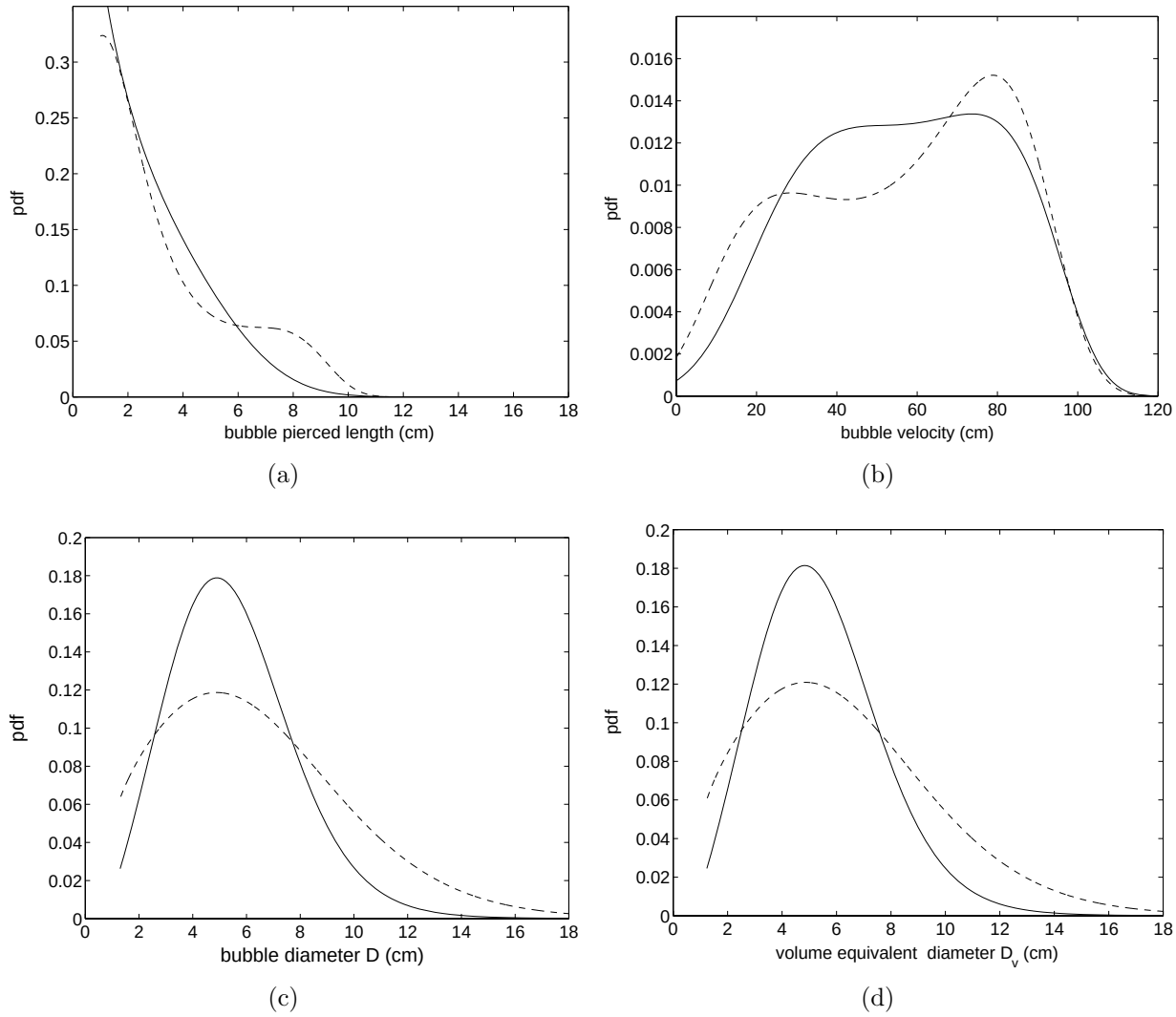

Figure 5.10: PDF of (a) bubble pierced length (b) bubble velocity (c) bubble diameter D (d) volume equivalent diameter D_v from optical (solid line) and pressure (dash line) measurements. $U = 0.57m/s$, $U/U_{mf} = 1.4$. $z_{op} = 10.5$ cm, $z_{pt} = 13$ cm. $r/R = 0$.

pressure measurements exhibits a second peak around $y = 8$ cm. This behavior is not observed in the PDF obtained from the optical measurements. This may be due to the be-

ginning of the coalescence phenomenon, since first, the pressure probes are located higher in the bed and second, it is not possible to distinguish between two bubbles coalescing and one single large bubble using pressure signals. PDF of bubble velocity (Fig. 5.10(b)) could be considered somehow a uniform distribution. As for bubble diameter and bubble equivalent diameter distributions (Fig. 5.10(c) and 5.10(d)) it can be seen that the most frequent value is very similar for the pressure and optical measurements. Slight differences may be explained by the difference in the height position. However, the variance of the pressure measurements is higher. This is due to the pressure signals are influenced by other phenomena but bubble passage whereas optical are very good phase detection probes.

Bubble characteristics were also measured at a lower height in the bed, using optical probes. It was not possible to obtain bubble parameters from pressure signals close to the distributor as the bubble detection was very difficult due to the smaller size of the bubbles. Besides no works have been found in the literature reporting experimental measurements at such low height.

z (cm)	y (cm)	D_v (cm)
10.5	**Optical:** mean = 3.20 std = 1.78 **Pressure:** mean = 3.72 std = 2.36	**Optical:** mean = 5.51 std = 2.38 **Pressure:** mean = 6.49 std = 3.41
5.5	**Optical:** mean = 2.82 std = 1.43	**Optical:** mean = 4.75 std = 1.68

Table 5.1: Mean and standard deviation of y and D_v of bubbles measured at $z = 10.5$ cm and $z = 5.5$ cm.

Results for a height $z = 5.5$ cm above the distributor and a radial position $r/R = 0.8$ are shown in Fig. 5.11. The mean and standard deviation of y and D_v are summarized in Table 5.1. Comparing Fig. 5.10 and 5.11 it is shown that as expected, the mean values of y, D and D_v are smaller for the lower height. The variance is also smaller. In this case, unlike $z = 10.5$ cm case, the peak of the $PDF(y)$ (the most frequent value) can be seen in the distribution. This is because the mode of this distribution is greater than s. However the mean value and the standard deviation are, as noted earlier, smaller. Observing the PDF(y) in Fig. 5.11(a) it can be concluded that just a small portion of the distribution is truncated. This is also the case for the PDF(D_v) (or PDF(D)) for both cases ($z = 10.5$

cm and $z = 5.5$ cm). Observing these distributions in Fig. 5.10(d) and Fig. 5.11(d) it is expected that the number of bubbles which have a diameter smaller than the minimum measurable diameter is very small.

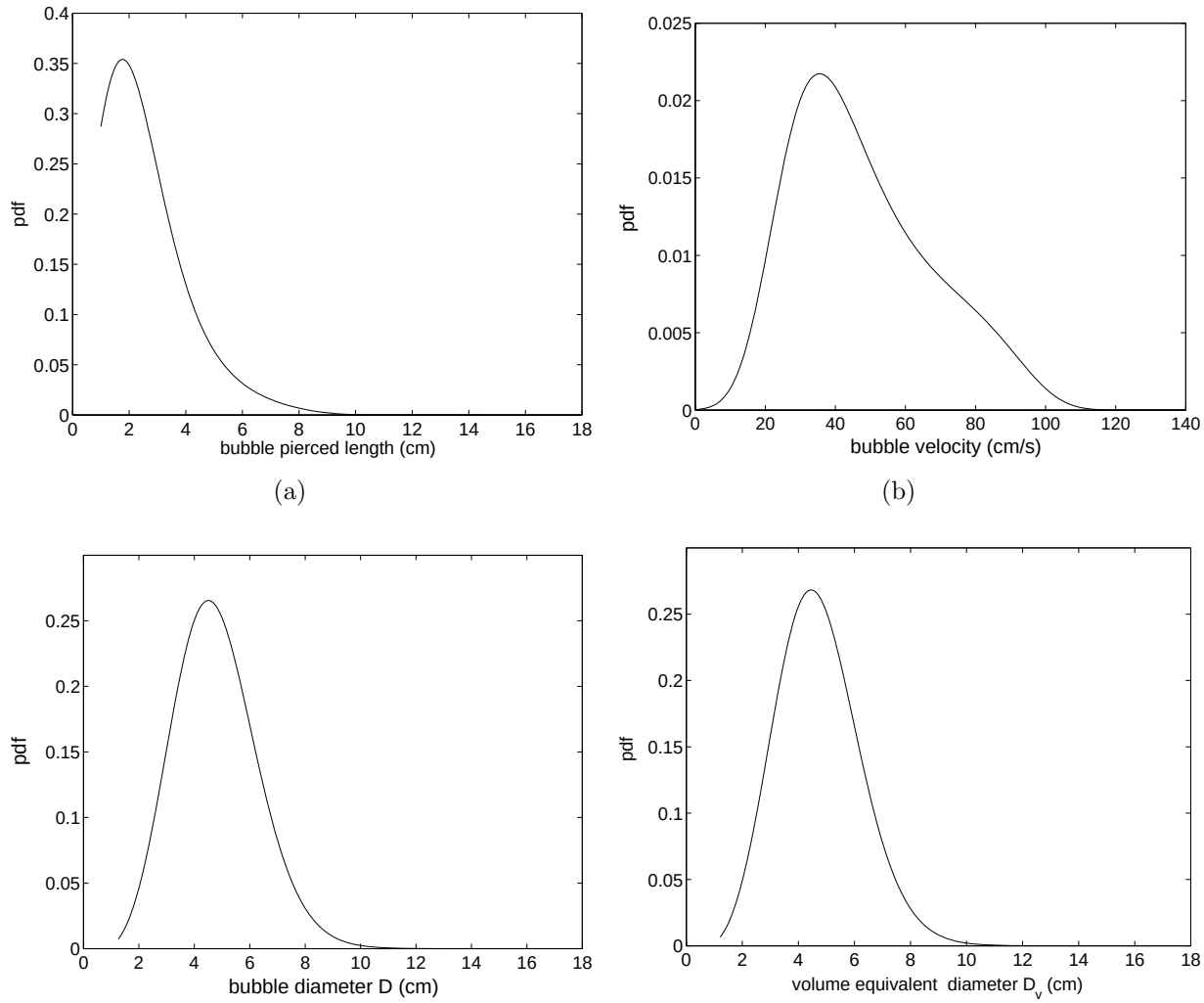

Figure 5.11: PDF of (a) bubble pierced length (b) bubble velocity (c) bubble diameter D (d) volume equivalent diameter D_v from optical measurements. $U = 0.57m/s$, $U/U_{mf} = 1.4$. $z_{op} = 5.5$ cm. $r/R = 0.8$.

5.6 Conclusions

In this chapter the probability distributions of bubble pierced length, velocity and diameter in a three-dimensional fluidized bed have been obtained.

Experimental measurements of bubble pierced length and bubble velocity were carried out recording differential pressure and optical probe signals. Optical probes have been found to be more flexible, being able to measure along the whole bed height. The optical signal is also less affected by the whole bed phenomena other than the bubble passage. The pressure probe gave similar results to optical probes regarding mean values but the variance of the distributions were higher due to the influence of other phenomena in the bed besides bubble passage. The analysis of differential pressure signal was not enough to distinguish two bubbles coalescing from a large bubble. However pressure probes provide useful information on bubble characteristics having the advantage of being very simple instrumentation and can be used in hot devices.

The Maximum Entropy Method was applied to obtain the probability density distributions of bubble pierced length, bubble velocity and bubble diameter in fluidized beds for the first time. Bubble pierced length and velocity distributions were obtained directly from experimental measurements. However an expression for the estimation of the bubble diameter distribution from pierced length raw moments had to be obtained, as diameters can not be measured. The sampling probes do not allow to measured pierced lengths smaller than the distance between probes s. This lower limit was introduced in the size distribution estimation.

Chapter 6

Rotation effect in bubble characteristics

In this chapter the effect of the distributor rotation on the bubble size, bubble passage frequency and bubble distribution is studied for different radial and axial positions in the bed.
A simple theoretical expression is obtained and used to analyze the influence of the centrifugal acceleration on the bubble when it detaches from the distributor.
Bubble pierced lengths have been measured using optical probes. The probability distributions of bubble diameter have been obtained from these experimental measurements using the method explained in the previous chapter. The minimum fluidization velocity decreases when the rotational speed increases as reported by Sobrino et al. (2008). In this chapter experiments at the same gas velocity and also at the same excess gas U/U_{mf} with the static distributor and with the distributor rotating at 100 rpm were compared.

6.1 Introduction

Gas bubbles present in most gas-solids beds can cause both chemical and mechanical difficulties. For instance, in gas-solids reactions, some of the gas in the bubbles may by-pass the particles altogether with little contact with the bed solids, thus, the overall efficiency of contact is lowered (Davidson and Harrison, 1963). However bubbles have also advantageous effects since they are responsible for the gas solids mixing and gas circulation and thus they play an important role in chemical reactions in fluidized beds. Therefore controlling the bubble size to avoid large and fast bubbles that bypass the bed and increase

the elutriation is an important task.

Bubble characteristics such as bubble size, shape or ascending velocity are important parameters that have been extensively studied in the past (Ghadiri et al., 1988; Dent et al., 1989; Werther and Molerus, 1973; Werther, 1974b; Ramaya et al., 1993). Different techniques have been developed to study the bubble properties in fluidized beds, some of them reviewed by Cheremisinoff (1986); Yates and Simons (1994) and Werther (1999). One of the most popular techniques is the use of optical probes. They have been widely applied for the measurement of particle velocity and particle concentration in three-dimensional fluidized beds and to a lesser extent to detect the passage of bubbles and measure their main parameters (Ishida and Shirai, 1980; Hatano and Ishida, 1981; Schweitzer et al., 2001; Glicksman et al., 1987).

The interpretation of the signals from dual submergible probes for bubble size determination is difficult as they give information on pierced length rather than characteristic diameter and this conversion is not straightforward. An extended review of the different methods employed for this conversion can be found in Santana et al. (2006). In the previous chapter the Maximum Entropy Method was explained.

Several methods have been used to improve the quality of fluidization. Vibration (Mawatari et al., 2003) and agitation (Kim and Han, 2006) have been used in some designs to avoid unwanted phenomena as channeling or agglomeration, in the fluidization of cohesive fine particles. On the other hand, flow pulsation (Köksal and Vural, 1998) has been studied as a way to control the bubble size. Other attempts consist on the design of special distributors. Swirling fluidizing patterns generated by different distributor designs (Chyang and Lin, 2002; Sreenivasan and Ragahavan, 2002) or the tangential injection of gas proved to increase the lateral mixing of solids giving a substantial improvement over the predominant axial flow pattern in conventional fluidized beds. The injection of secondary air with a swirl has been also successfully tested to intensify the lateral dispersion of particles in circulating fluidized beds (Ran et al., 2001). None of these works give information on the behavior of the bubbles.

In this work the rotating distributor and the static distributor designs are compared. In Chapter 4 the main global characteristics were compared. In this chapter bubbles characteristics and bubble flow patterns are studied using dual optical fiber probes (Vázquez et al., 2007). The new methodology explained in the previous chapter is applied to obtain the probability distribution of bubble diameter from the pierced length measurements.

6.2 Experiments

Bubble pierced lengths were measured using optical probes. Experimental set-up and signal processing were explained in Chapter 5. The rotating distributor described in Chapter 3 was used to study the rotation effect on bubble size and bubble distribution in the bed. The rotational speed was set to 100 rpm and this configuration was compared with the static configuration. The influence of two different parameters was studied: the height of the bed above the distributor, z and the radial position in the bed r. The effect of varying the superficial gas velocity was also varied.

6.3 Bubble formation model

Bubbles in a fluidized bed rise as if they were in an ordinary liquid of small viscosity and zero surface tension (Davidson and Harrison, 1963). The bubble and particulate phases of a fluidized bed appear to be analogous to the gas and liquid phases in a two-phase system. When air is blown steadily through an orifice into a liquid of small viscosity at intermediate flow-rates, a more or less regular train of bubbles is formed. The mechanism of bubble formation at the distributor orifices in fluidized beds has been extensively studied. Harrison and Leung (1961) found good agreement between experiments on bubble formation at an orifice in air-fluidized beds and in air-water systems. In this section, the influence of the rotational speed on the size of bubbles formed at the orifices on the basis of a simplified model will be studied.

The frequency and size of bubbles in fluidized beds at intermediate flow-rates is governed mainly by a balance between buoyancy forces and inertial forces (Davidson and Harrison, 1963). The flow-rate in the emulsion phase can be thus neglected. In the present study the perforated plate where bubbles are formed rotates and thus the centrifugal force acting on the bubble when it detaches form the distributor plays also a role. The viscous drag is considered negligible, provided the low viscosity of fluidized beds. The magnitude of the buoyancy force, F_b and the centrifugal force, F_c, can be given as:

$$F_b = \rho_{bulk} V g \tag{6.1}$$

$$F_c = \frac{1}{2} \rho_{bulk} V \omega^2 r \tag{6.2}$$

Where $\rho_{bulk} = [\rho_p(1-\epsilon) + \rho_f\epsilon]$ is the bulk density of the particulate phase and V is the bubble volume at time t. The bubble motion at detachment is defined as balance of the buoyancy and centrifugal forces against the rate of change of upward momentum of the particle phase surrounding the bubble. The inertia of the air within the bubble is neglected. For the forming bubble the upward momentum at any instant is therefore:

$$\frac{1}{2}\rho_{bulk} V u_o \tag{6.3}$$

Where u_o is the rising velocity of the bubble centre. It has to be noted that when a sphere moves in an inviscid fluid, with no separation of the flow, the effective mass added to the sphere by the surrounding fluid is half the displaced mass. This mass has been introduced in Eq. (6.2) and (6.3).
The buoyancy and centrifugal forces have perpendicular directions and hence the equation of the upward motion is

$$\sqrt{(\rho_{bulk} V g)^2 + \left(\frac{1}{2}\rho_{bulk} V \omega^2 r\right)^2} = \frac{d}{dt}\left(\frac{1}{2}\rho_{bulk} V u_o\right) \tag{6.4}$$

On the other hand, the bubble volume growth rate is:

$$\frac{dV}{dt} = q \tag{6.5}$$

Where q denotes the volumetric flow rate through a hole of the distributor that goes into the bubble,

$$q = \frac{(U - U_{mf})A}{N_o} \tag{6.6}$$

where A is the area of the distributor and N_o is the number of holes in the distributor. The volume of the bubble is $V = \frac{4}{3}\pi r_b^3$ and hence

$$\frac{dr_b}{dt} = \frac{q}{4\pi r_b^2} \tag{6.7}$$

Assuming that the velocity of the bubble center, u_o is equal to the growth rate of the bubble dr_b/dt (Fujikawa et al., 2003) and introducing Eq. (6.7) in the forces balance (6.4)

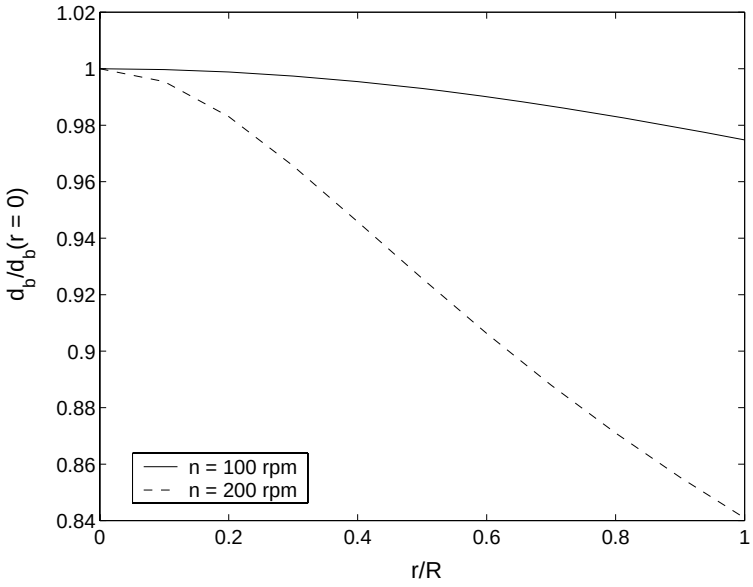

Figure 6.1: Bubble diameter at detachment for two different rotational speeds.

gives,

$$\sqrt{(\rho_{bulk} V g)^2 + (\frac{1}{2}\rho_{bulk} V \omega^2 r)^2} = \frac{\rho_{bulk} q^2}{24\pi r_b^2} \tag{6.8}$$

From this equation the bubble radius at the detachment can be obtained as

$$r_b = \left[\frac{q^2}{32\pi^2\sqrt{g^2 + (\frac{1}{2}\omega^2 r)^2}}\right]^{1/5} \tag{6.9}$$

Fig. 6.1 shows the expected bubble diameters at detachment for the rotating distributor as a function of the radial position calculated using the above equation. The diameter has been non-dimensionalized with the bubble diameter at the center of the plate, where the centrifugal acceleration $\omega^2 r$ is zero. The maximum rotational speed reached during the experiments was 100 rpm but Fig. 6.1 shows results for 100 rpm and 200 rpm. It can be seen that for a given excess of gas, the rotation makes the bubble size to decrease. This decrease is higher at higher r or higher rotational speed since the centrifugal acceleration increases with r and ω.

6.4 Results and discussion

The effect of the distributor rotation in the bubble frequency and size was studied. It was shown in Chapter 3 that U_{mf} decreases when the rotational speed increases, therefore three different cases were studied:

(a) The static distributor with a gas velocity $U = 0.57$ m/s and an excess gas $U/U_{mf,0} = 1.42$.

(b) The distributor rotating at $n = 100$ rpm with a gas velocity $U = 0.57$ m/s and an excess gas $U/U_{mf,100} = 1.9$.

(c) The distributor rotating at $n = 100$ rpm with a gas velocity $U = 0.46$ m/s and an excess gas $U/U_{mf,100} = 1.53$.

The comparison between cases (a) and (b) shows the effect of the rotation for equal gas velocities. Since U_{mf} is higher for the rotating distributor, the excess gas is higher in this case (case (b)) than for the static distributor (case (a)). A comparison between cases (a) and (c) shows the effect of rotation for equal excess gas conditions.

6.4.1 Radial profile of bubble size

The theory of bubble formation explained in the previous section pointed out the influence of the rotation on the bubble diameter at its detachment. It was shown that the centrifugal acceleration promotes the decrease of the bubble size.
Bubble pierced lengths were measured along the bed radius at 7.5 cm above the distributors. Three different cases were studied corresponding to the experimental conditions described at the beginning of this section.
Fig. 6.2 shows the mean value of the pierced length measurements. At the higher velocity ($U = 0.57$ m/s) the influence of the rotation is not important since the axial velocity predominates over the rotation. At this velocity, the bubble pierced length for the rotating distributor is only slightly larger than for the static case, even though the excess gas is much higher. For the lower velocity ($U = 0.46$ m/s) the rotation effect is appreciable and thus the bubble pierced length diminishes with the radial position (higher centrifugal acceleration). At this gas velocity the excess gas for the rotating distributor is equal to the excess gas for the static case. Comparing these two cases it can be concluded that except for radial positions close to the bed axis, the mean pierced lengths are smaller for

the rotating distributor.

The pierced length data were used to obtain the distribution of bubble diameter. This

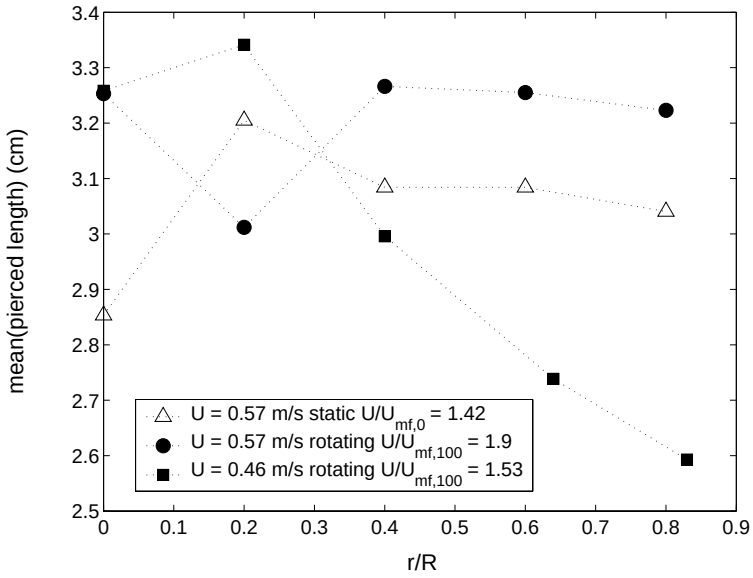

Figure 6.2: Bubble pierced length against the radial position for the static and rotating configuration (n = 100 rpm) at different gas velocities and excess gas conditions. z = 7.5 cm.

was done applying the Maximum Entropy Method explained in Chapter 5. Fig. 6.2 compares the probability distribution of the volume equivalent diameter, D_v, at different radial positions for the static distributor and with the distributor rotating at 100 rpm. Fig. 6.3(a) shows the results for the static configuration (case (a)) and Fig. 6.3(b) and 6.3(c) show the results for the rotating configuration for the same gas velocity and excess gas as in the static case. The minimum value that was measurable with the probes was y = 1 cm, which is the distance between probes. Therefore the distributions in Fig. 6.3 are the distributions of diameters larger than $D_{v,min}$, where $D_{v,min}$ is determined by s and the bubble shape as explained in Chapter 5. It can be seen that for values of r/R larger than 0.4 distributions for the rotating and static cases, at the same excess gas differ: when the distributor rotates the peak is displaced to lower D_v and the variance also diminishes (Fig. 6.3(c)). For larger excess gas the rotation effect tends to disappear (Fig 6.3(b)).

The mean values of the distributions are plotted in Fig. 6.4 as a function of the radial position. It can be observed that for the same gas velocity U = 0.57 m/s the bubble diameters are slightly bigger for the rotating distributor. According to the excess gas, which in this case is much higher, it seems that the rotation leads to a better excess gas distribution. When similar excess gas conditions are compared ($U/U_{mf,0}$ = 1.42 and

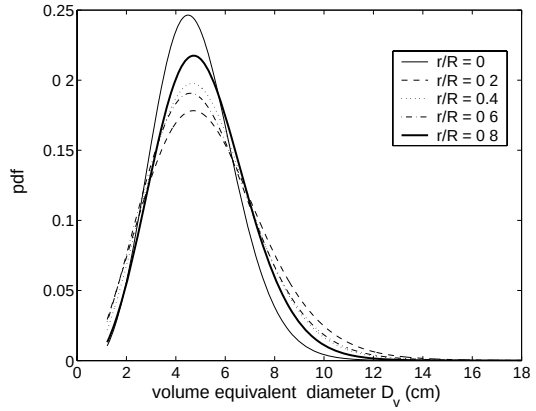

(a)

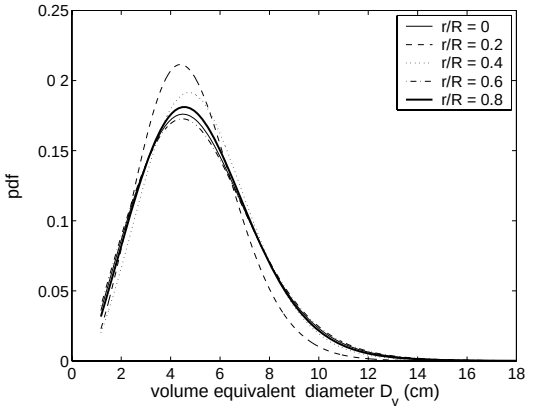

(b)

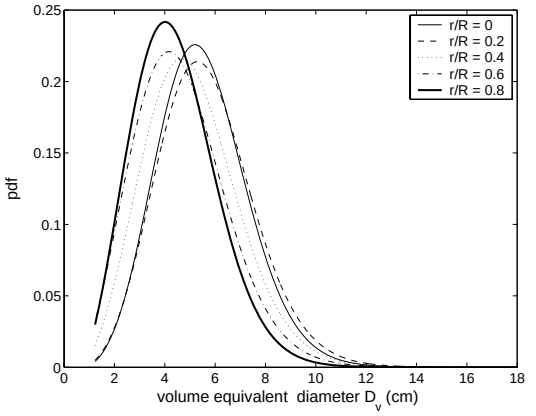

(c)

Figure 6.3: PDF of volume equivalent diameter at different radial positions (a) Static distributor, $U = 0.57$ m/s, $U/U_{mf,0} = 1.42$. (b) Rotating distributor $n = 100$ rpm, $U = 0.57m/s$, $U/U_{mf,100} = 1.9$. (c) Rotating distributor $n = 100$ rpm, $U = 0.46m/s$, $U/U_{mf,100} = 1.53$. $H = 20$ cm. $z = 7.5$ cm.

$U/U_{mf,100} = 1.53$ for the static and rotating distributor respectively) it can be observed that quite smaller bubbles are found close to the bed wall for the rotating case. At higher r, the centrifugal acceleration is higher and then there is a marked effect on bubble size. This is in agreement with the behavior predicted from the forces balance shown in Fig. 6.1. When the gas velocity is higher ($U = 0.57$ m/s) the rotation effect is negligible, since the axial velocity of the flow in the bed is far larger than the tangencial velocity imparted by the rotation. This is also in agreement with the conclusions of the pressure fluctuations analysis in Chapter 4: the rotation effect becomes less noticeable at high gas flow rates. This behavior was not considered in the theoretical deduction since the flow-rate in the emulsion phase was neglected.

Fig. 6.5 shows the number of bubbles that are detected at each radial positions for each of the three cases described above. It can be seen that there are only a few bubbles ascending at the bed axis for the static distributor. This is a consequence of the holes layout and the absence of holes in this area. However, when the plate rotates, more bubbles appear in the bed axis since the rotation promotes the more homogenous distribution of bubbles in the bed. Moreover it was shown in Fig. 6.4 that if U is the same when the static and rotating distributors are compared, even if the excess gas is higher in the rotating case, the size of the bubbles is quite similar. Fig. 6.5 shows that this excess gas is transported by this higher number of bubbles. This higher number of bubbles is more pronounced

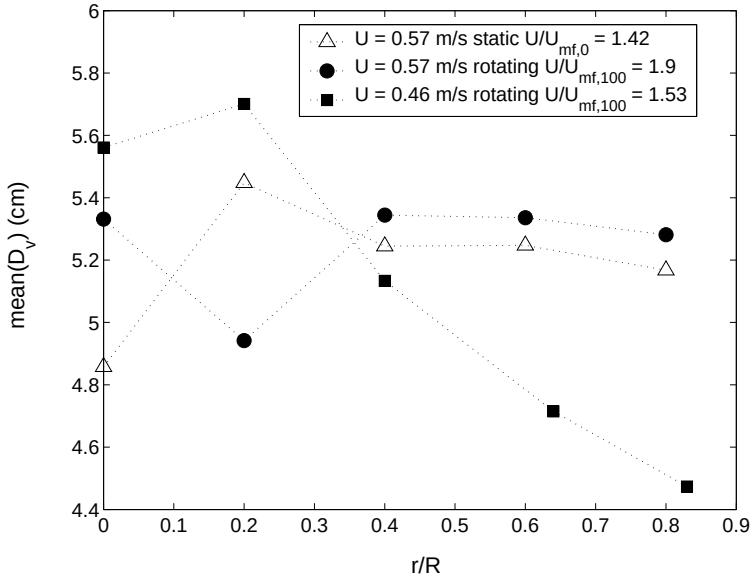

Figure 6.4: Mean volume equivalent diameter against the radial position for the static and rotating configuration ($n = 100$ rpm) at different gas velocities and excess gas conditions. $H = 20$ cm. $z = 7.5$ cm.

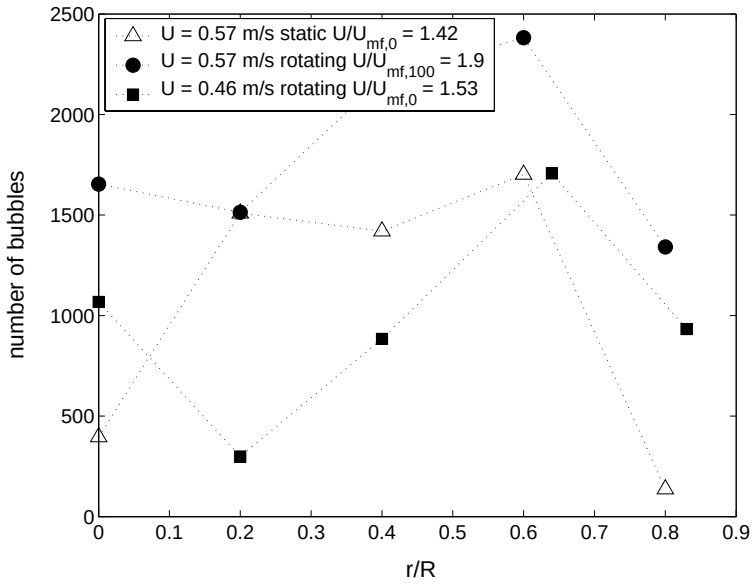

Figure 6.5: Number of bubbles detected at different radial positions for the static and rotating configuration ($n = 100$ rpm) at different gas velocities and excess gas conditions. $H = 20$ cm. $z = 7.5$ cm.

as the bed wall is approached since the detachment at a higher r/R is promoted earlier because of the effect of the centrifugal force.

It was explained in Chapter 5 that the relation between bubble pierced length and bubble diameter depends on the shape factor. The shape factor was obtained using the correlation (5.29) proposed by Werther (1976). In this correlation the bubble shape depends on the excess gas and the height in the bed and therefore on bubble size. This indicates that changes on excess gas or height will affect on a different manner the bubble pierced length and bubble diameter. This explains the differences on pierced length to diameter relation along r observed when comparing Fig. 6.2 and 6.4.

6.4.2 Height effect

The change of the bubble size with the height in the bed has been studied carrying out measurements at different axial positions and a given radial position r/R = 0.8. Experiments with the static and rotating distributor at the same gas velocity were compared. Probability distributions of the volume equivalent diameter at different heights in the bed are shown in Fig. 6.6. With the static distributor there are clear differences when measuring at different heights in the bed: the mode of D_v increasing with the height and the variance is also larger. In the case of the rotating distributor more homogeneity is

found all over the bed (at this radial position): the mode and the variance remains almost the same at different heights.

The mean values of these distributions and the mean values of the measured pierced lengths are shown in Fig. 6.7. It can be observed that the differences in bubble sizes due to the distributor rotation are important close to the distributor and become less noticeable as one moves upward in the bed. Bubble diameter using the rotating distributor barely increases as height increases. For heights larger than 10 cm the bubble size is similar for both distributors and even smaller for the rotating case. This effect could be explained by the bubble coalescence rate that seems to be lower for the rotating distributor (bubble preferential paths are broken with the rotation).

Measurements at other radial positions ($r/R = 0.5$ and $r/R = 0$) and higher z are shown in Fig. 6.8.

It can be seen again in Fig. 6.8 that at high axial positions when the amount of gas used

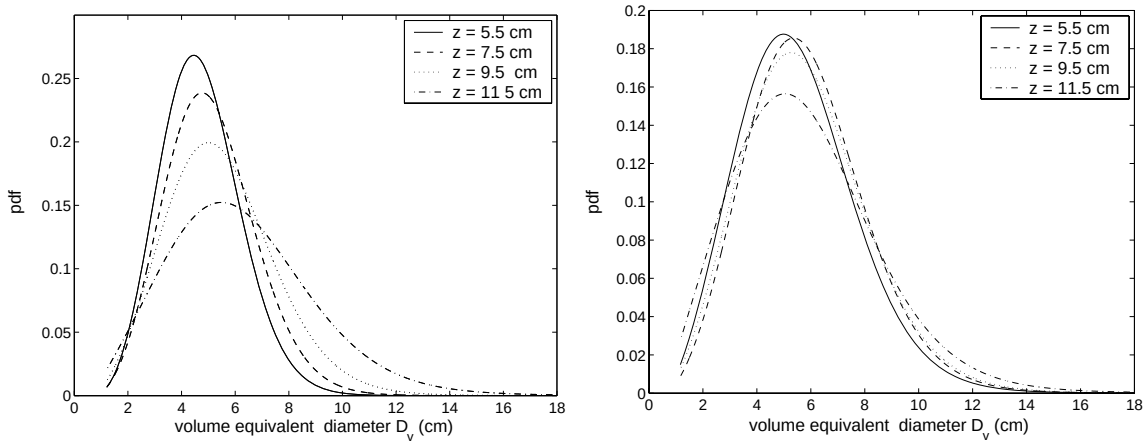

(a) (b)

Figure 6.6: PDF of D_v at different heights above the distributor. (a) Static distributor $U = 0.57$ m/s, $U/U_{mf,0} = 1.42$. (b) Rotating distributor at $n = 100$rpm $U = 0.57$ m/s $U/U_{mf,100} = 1.9$. r/R = 0.8

to fluidize both the static and the rotating distributor beds is the same, even if the excess gas is higher, the bubble diameter is lower for the rotating distributor. The number of bubbles detected for each case is shown in the figure. It is seen that more bubbles are found in the rotating case and even if the bed is operating with more excess gas the bubbles are smaller: in the rotating bed higher excess gas can be handled with a larger number of bubbles.

6.5 Conclusions

The size, spatial distribution and frequency of the bubbles found in a fluidized bed for configurations involving a static distributor and a rotating one were compared. The

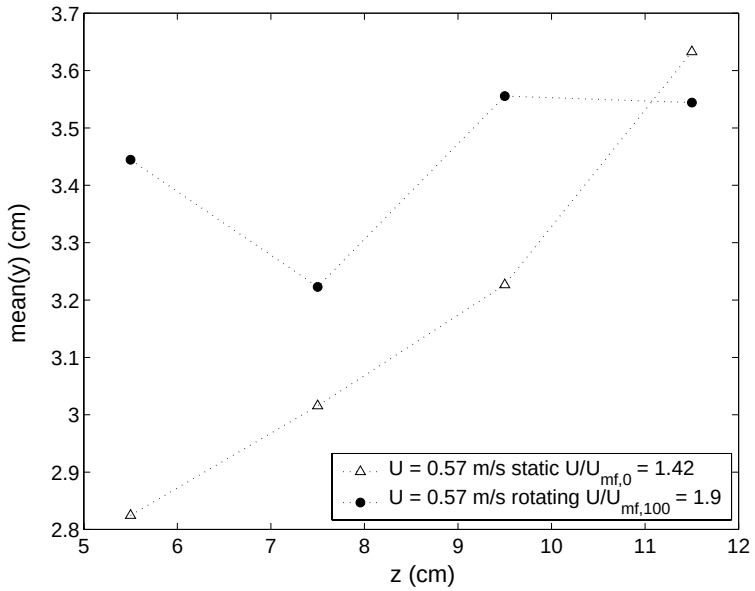

(a)

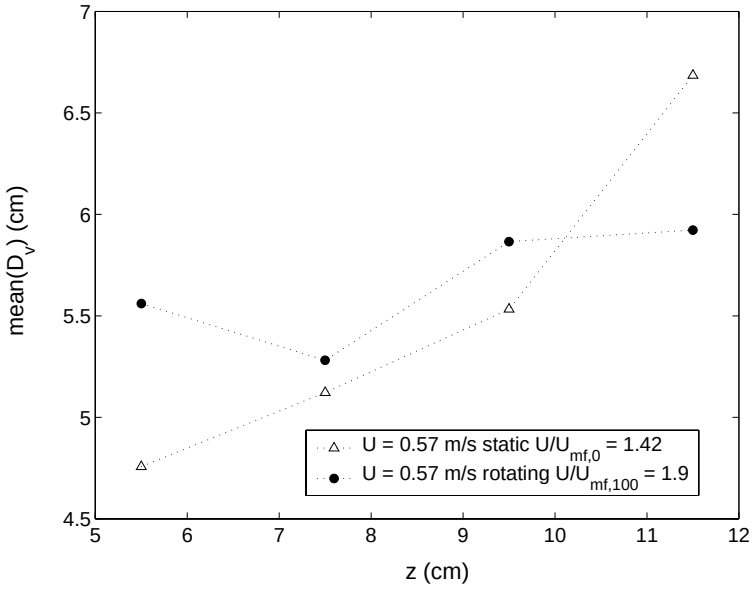

(b)

Figure 6.7: Mean value of (a) pierced length (b) volume equivalent diameter, against the height above the distributor for the static and rotating configuration ($n = 100$ rpm) at the same gas velocity. $r/R = 0.8$ cm.

motion equation of the bubbles formed at the distributor points out that the centrifugal acceleration imparted by the rotation causes the decrease of the initial bubble radius. This theoretical result is corroborated by experimental measurement of bubble size in the bed, near the distributor.

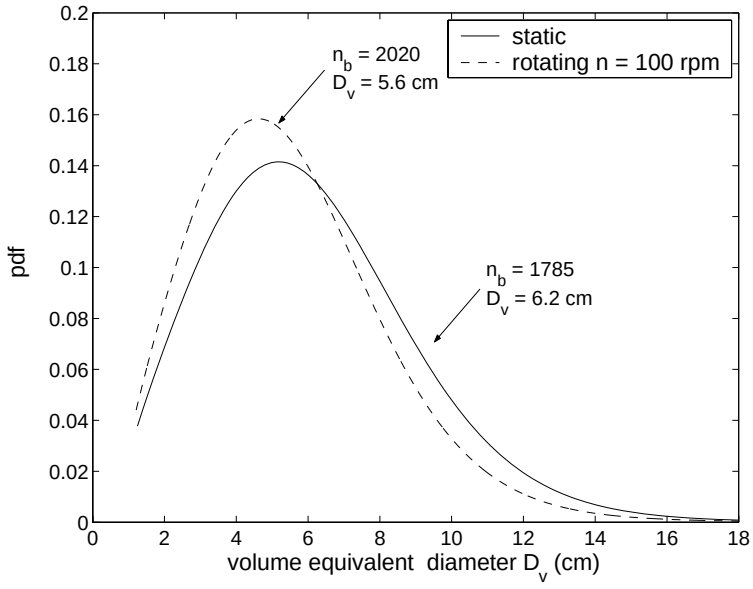

(a)

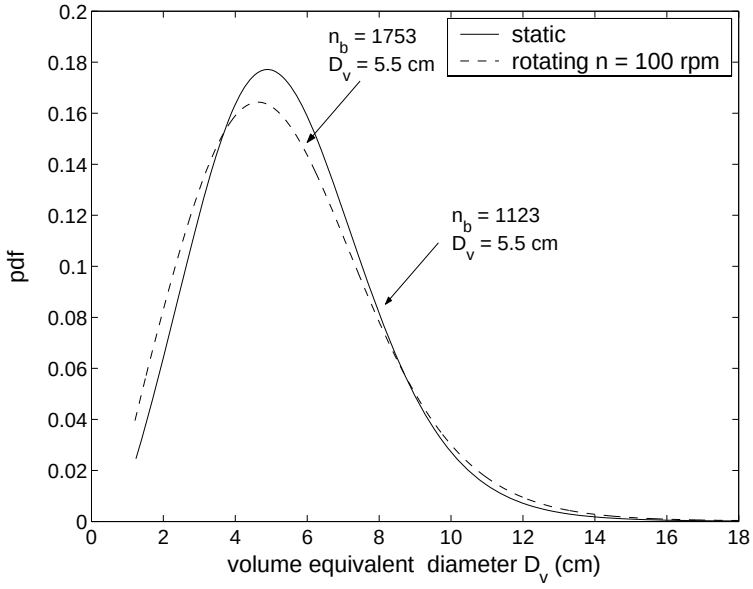

(b)

Figure 6.8: PDF of D_v at $U = 0.57$ m/s and $z = 12.5$ cm for the static ($U/U_{mf,0} = 1.42$) and rotating distributor ($U = 0.57$ m/s $U/U_{mf,100} = 1.9$). (a) r/R = 0.5 (b) r/R = 0

Smaller bubbles were found for the rotating distributor when the excess gas for the static and rotating configuration was similar. The bubble size radial profile indicates that when the distributor rotates, the diameter of the bubbles close to the bed walls is smaller, the centrifugal acceleration being higher. The distributor rotation also promotes a more homogenous distribution of the bubbles over the bed surface. The study of the bubble size at different heights in the bed shows that for the same gas velocity bubble diameter is higher when the distributor rotates than for the static distributor. This was expected since the minimum fluidization velocity is much lower for a rotational speed of 100 rpm. However the differences in bubble diameter is lost at higher axial positions and even smaller bubbles are found for the rotating case at heights over about 11 cm above the distributor. This may be due to the rupture of the preferential paths by the effect of the rotation what makes bubble coalesce events less frequent for the rotating distributor.

Chapter 7

Conclusions

The experiments carried out in the novel fluidized bed with rotating distributor presented in this thesis have led to remarkable insights into the fluid dynamic behavior of this system.

The study on the nature of the pressure fluctuations in fluidized beds which conclusions have been built across all the work carried out in the laboratory and its post-analysis, has been decisive for the success of the experiments and their correct interpretation. Single-point pressure measurement have been found to reflect what happens in the whole bed while differential pressure measurements reflect what happens between the two ports of the probe. A model that predicts the pressure signal on Geldart B bubbling fluidized bed was proposed. The calculated standard deviation of pressure fluctuations, σ_p, which depends on the distance between the measuring port and the bed surface, the excess gas $U - U_{mf}$ and the particles properties compared well with experimental results.

Gauge pressure measurements were carried out in the bed in order to study the effect of the distributor rotation on the bed behavior. The minimum fluidization velocity, U_{mf} was found to decrease with the increase of the distributor rotational speed. Then, bed performance was compared for different rotational speeds but keeping the same excess gas ratio (U/U_{mf}). Under these conditions the standard deviation of the pressure fluctuations does not vary significantly not depending on the rotational speed for low fluidizing gas flow rates. This indicates that bubble size is similar for the different rotational speeds what points out that this parameter allows to achieve the same quality of fluidization (e.g. the same size of bubbles, the same bubbling frequency) fluidizing the gas with different amount of gas just varying the rotational speed of the distributor. The power spectra of the pressure signals confirmed these results and even a lower power density was found for the rotating case if the superficial gas velocity was not too high. The rotation also allows

to fluidize very shallow beds since channels that are shown with the static distributor seem to turn into a smother bubbling when the rotation of the distributor is introduced. Since the explained results mainly reflect the global behavior of the bed, differential pressure measurements and measurements with optical probes were carried out with the aim of obtaining the main characteristics of the bubbles rising in the bed and the influence of the rotation on these bubbles. Optical reflective probes were in-house developed and they were found to have a very small measuring volume compared with differential pressure probes. Bubble pierced lengths and bubble velocities were obtained from these signals programming the signal processing with Matlab. The probability distributions of pierced length and velocity were obtained from these measurements using the Maximum Entropy Method which was here applied to experimental data for a 3D fluidized bed for the first time. Mean values of the pierced lengths and velocities obtained from optical and pressure signals were very similar, however the variance of the resulting distribution from pressure measurements was much higher. This may be explained by the influence of other phenomena rather than the bubble passage on the pressure signal.

The same method was also used to obtain the PDF of the bubble diameter from bubble pierced length measurements using statistical principles. The analysis by Santana et al. (2006) was modified in order to introduce the characteristic bubble geometry in fludized beds (a truncated oblate spheroid) and the effect of the finite size of the measuring probe which introduces a lower limit to the size distributions.

The optical probes and the developed new method are then used to characterize the bubbles in the fluidized bed and how they change when the distributor rotates. These probes were chosen since they showed to provide a more local measurement than pressure probes and also were capable of measuring at any point in the bed even close to the distributor. Results showed similar bubbles sizes for the static and the rotating distributor when the fluidizing gas velocity was the same (higher excess gas $U - U_{mf}$ for the rotating case) and smaller bubbles with the rotating distributor when fluidizing the bed at the same excess gas rate. When the bed worked with the rotating distributor, smaller bubbles rose near the walls since the centrifugal acceleration is higher at higher radial distances. The rotation was also found to distribute the bubbles more homogenously in the bed surface; only a few bubbles were detected on the bed axis with the static distributor while this number rose a lot when the distributor rotated. This indicates that the rotation introduces a radial component to the predominant axial component of the flow present in classical fluidized beds. The bubbles growth in size as they rise in the bed is found to be much lower when the distributor plate rotates. This may be due to a lower coalescence rate

since the preferential paths for bubbles are cut off by the rotation.

Further interesting results will emerge from the use of this distributor in a hot fluidized bed. This distributor will be used in a biomass gasifier in Carlos III University that will be launched shortly. The study of the conversion rate and the gas product in the gasifier will provide data on the expected enhances achieved with the novel distribution.
It would be also interesting to study the particles and gas mixing using tracer particles and tracer gases particles and the residence time of the fuel using e.g. Positron-Emision Particle Technique (PEPT). These experiments could confirm the enhancement of the radial mixing and the avoidance of hot spots due to fuel feeding that are expected to be achieved with the novel distributor.
The novel rotating distribution could have also a promising performance in the fluidization of Geldart C particles. Other techniques as vibrating or sound assisted fluidized beds have been reported to fluidize these particles otherwise impossible to achieve.

Bibliography

Alzahrani, A. A., Wali, M. M. N., 1993. A study of pressure drop fluctuations in a gas-solids fluidized bed. Powder Technology 76, 185–189.

Bai, B., Gheorghiu, S., van Ommen, J. R., Nijenhuis, J., Coppens, M.-O., 2005. Characterization of the void size distribution in fluidized beds using statistics of pressure fluctuations. Powder Technology 160, 81–92.

Baskakov, A. P., Tuponogov, V. G., Filippovsky, N. F., 1986. A study of pressure fluctuations in a bubbling fluidized bed. Powder Technology 45, 113–117.

Bi, H. T., 2007. A critical review of the complex pressure fluctuation phenomenon in gas-solids fluidized beds. Chemical Engineering Science 62, 3473–3493.

Bi, H. T., Grace, J. R., Zhu, J., 1995. Propagation of pressure waves and forced oscillations in gas-solid fluidized beds and their influence on diagnostics of local hydrodynamics. Powder Technology 82, 239–253.

Bratu, E., Jinescu, G. I., 1971. Effect of vertical vibrations on pressure drop in a fluidised layer. British Chemical Engineering 16, 691–695.

Briongos, J. V., Aragón, J. M., Palancar, M. C., 2006. Fluidised bed dynamics diagnosis from measurements of low-frequency out-bed passive acoustic emissions. Powder Technology 162, 145–156.

Chan, I. H., Sishtla, C., Knowlton, T. M., 1987. The effect of pressure on bubble parameters in gas-fluidized beds. Powder Technology 53, 217–235.

Chen, A. H., Bi, H. T., 2003. Pressure fluctuations and transition from bubbling to turbulent fluidization. Powder Technology 133, 237–246.

Cheremisinoff, N. P., 1986. Review of experimental methods for studying the hydrodynamics of gas-solid fluidized beds. Ind. Eng. Chem. Process Des. Dev 25, 329–351.

Chyang, C.-S., Lin, Y.-C., 2002. A study in the swirling fluidizing pattern. Journal of Chemical Engineering of Japan 35, 503–512.

Clark, N. N., Atkinson, C. M., 1988. Amplitude reduction and phase lag in fluidized-bed pressure measurements. Chemical Engineering Science 43, 1547–1557.

Clark, N. N., Liu, W., Rurton, R., 1996. Data interpretation techniques for inferring bubble size distribution from probe signals in fluidized systems. Powder Technology 88, 179–188.

Clark, N. N., Turton, R., 1988. Chord length distributions related to bubble size distributions in multiphase flows. International Journal of Multiphase Flow 14, 413–424.

Croxford, A. J., Harrison, A. J. L., Gilbertson, M. A., 2005. The optimization of pressure measurements for the control of bubbling fluidised beds. International Journal of Chemical Reactor Engineering 3, A39.

Darton, R. C., LaNauze, R. D., Davidson, J. F., Harrison, D., 1977. Bubble-growth due to coalescence in fluidized-beds. Transactions of the institution of chemical engineers 55, 274–280.

Davidson, J. F., Harrison, D., 1963. Fluidized particles. Cambridge University Press.

Davidson, J. F., Harrison, D., Guedes de Carvalho, J. R. F., 1977. On the liquidlike behavior of fluidized beds. Ann. Rev. Fluid Mech. 9, 55–86.

Delebarre, A., Morales, J. M., Ramos, L., 2004. Influence of the bed mass on its fluidization characteristics. Chemical Engineering Journal 98, 81–88.

Dent, D., LaNauze, R. D., Joyce, T., Fulford, V., Peeler, P., 1989. Differential pressure measurements - their application to measuremets of fluidized bed combustion parameters. In: Proc. 10th Conf. Fluidized Bed Combustion. pp. 451–456.

Elder, H. J., 1956. US Patent 276176.

Ellenberger, J., Krishna, R., 1994. A unified approach to the scale-up of gas-solid fluidized bed and gas-liquid bubble column reactors. Chemical Engineering Science 49, 5391–5411.

Ellenberger, J., Krishna, R., 2003. Shaken, not stirred, bubble column reactors: Enhancement of mass transfer by vibration excitement. Chemical Engineering Science 58, 705–710.

Ergun, S., 1952. Fluid flow through packed columns. Chemical Engineering Progress 48, 89–94.

Esin, A., Cakaloz, T., 1979. Effect of distributor rotation on gas mixing in a fluidized bed. Powder Technology 23, 245–251.

Fan, L. T., Ho, T.-C., Hiraoka, S., Walawender, W. P., 1981. Pressure fluctuations in a fluidized bed. AIChE Journal 27, 388–396.

Felipe, C. A. S., Rocha, S. C. S., 2007. Prediction of minimum fluidization velocity of gas-solid fluidized beds by pressure fluctuation measurements - analysis of the standard deviation methodology. Powder Technology 174, 104–113.

Fujikawa, S., Zhang, R., Hayama, S., Peng, G., 2003. The control of micro-air-bubble generation by a rotational porous plate. International Journal of Multiphase Flow 29, 1221–1236.

Geldart, D., 1973. Types of gas fluidization. Powder Technology 7, 285–292.

Ghadiri, M., Carter, B., Rathbone, R. R., Clift, R., Medhurst, S. J., Rogers, E. A., Summerfield, I., 1988. Diagnosis of gas flow patterns in fluidised beds. In: Proc. 4th International Fluidized Bed Combustion Conference. Institute of Energy.

Glicksman, L. R., Lord, W. K., Sakagami, M., 1987. Bubble properties in large-particle fluidized beds. Chemical Engineering Science 42, 479–491.

Hao, B. G., Bi, H. T., 2005. Forced bed mass oscillations in gas-solid fluidized beds. Powder Technology 149, 51–60.

Harrison, D., Leung, L. S., 1961. Bubble formation at an orifice in a fluidised bed. Trans. Instn. Chem. Engrs., Lond. 39, 409–414.

Hatano, H., Ishida, M., 1981. The entrainment of solid particles from a gas-solid fluidized bed. Journal of Chemical Engineering of Japan 14, 306–311.

Herrera, C. A., Levy, E. K., 2001. Bubbling characteristics of sound-assisted fluidized beds. Powder Technology 119, 229–240.

Herringe, R. A., Davis, M. R., 1976. Gas-liquid mixture flows. Journal of Fluid Mechanics 73, 97–123.

Hiraoka, S., Kim, K. C., Shin, S. H., Fan, L. T., 1986. Properties of pressure fluctuations in a gas-solids fluidized bed under a free bubbling condition. Powder Technology 45, 245–265.

Hiraoka, S., Shin, S. H., Fan, L. T., Kim, K. C., 1984. Pressure fluctuations in a gas-solids fluidized bed - effect of external noise and bubble residence time distribution. Powder Technology 38, 125–143.

Hong, S. C., Jo, B. R., Doh, D. S., Choi, C. S., 1990. Determination of minimum fluidization velocity by the statistical analysis of pressure fluctuations in a gas-solid fluidized bed. Powder Technology 60, 215–221.

Ishida, M., Shirai, T., 1980. Measurement of the velocity and direction of flow of solid particles in a fluidized bed. Powder Technology 27, 1–6.

Jaynes, E. T., 1957. Information theory and statistical mechanics. Phys. Rev. 106, 620–630.

Johnsson, F., 2007. Fluidized bed combustion for clean energy. In: Xiaotao, B., Berruti, F., Pugsley, T. (Eds.), Fluidization XII. pp. 47–62.

Johnsson, F., Zijerveld, R. C., Schouten, J. C., van den Bleek, C. M., Leckner, B., 2000. Characterization of fluidization regimes by time-series analysis of pressure fluctuations. International Journal of Multiphase Flow 26.

Kai, T., Misawa, M., Takahashi, T., Tiseanu, I., Ichikawa, N., Takada, N., 2000. Application of fast x-ray CT scanner to visualization of bubbles in fluidized bed. Journal of Chemical Engineering of Japan 33, 906–909.

Karry, S. B. R., Werther, J., 2003. Gas distributor and plenum design in fluidized beds. In: Yang, W.-C. (Ed.), Handbook of fluidization and fluid-particle systems. Marcer Dekker, Inc., pp. 155–170.

Kim, J., Han, G. Y., 2006. Effect of agitation on fluidization characteristivcs of fine particles in a fludized bed. Powder Technology 166, 113–122.

Köksal, M., Vural, H., 1998. Bubble size control in a two- dimensional fluidized bed using a moving double plate distributor. Powder Technology 95, 205–213.

Kunii, D., Levenspiel, O., 1991. Fluidization Engineering. Butterworth-Heinemann.

Kwauk, M., Li, J., 1996. Fluidization regimes. Powder Technology 87, 193–202.

Lee, S. L. P., Soria, A., Lasa, H., 1990. Evolution of bubble length distribution in 3-phase fluidized beds. AIChE Journal 40, 1763–1767.

Leu, L.-P., Li, J.-T., Chen, C.-M., 1997. Fluidization of group b particles in an acoustic field. Powder Technology 94, 23–28.

Lirag, R. F., Littman, H., 1971. Statistical study of the pressure fluctuations in a fluidized bed. AIChE Journal 116, 11–22.

Littman, H., Homolka, G. A. J., 1973. The pressure field around a two-dimensional gas bubble in a fluidized bed. Chemical Engineering Science 28, 2231–2243.

Liu, J., Grace, J. R., Bi, X. T., 2003. Novel multifunctional optical-fiber probe: I. development and validation. AIChE Journal 49, 1405–1420.

Liu, W., Clark, N. N., 1995. Relationships between distributions of chord lengths and distributions of bubble size including their statistical parameters. International Journal of Multiphase Flow 21, 1073–1089.

Liu, W., Clark, N. N., Karamavruc, A. I., 1996. General method for the transformation of chord-length data to a local bubble size distribution. AIChE Journal 42, 2713–2720.

Liu, W., Clark, N. N., Karamavruc, A. I., 1998. Relationship between bubble size distribution and chord-length distribution in heterogeneously bubbling systems. Chemical Engineering Science 53, 1267–1276.

Luther, S., Rensen, J., Guet, S., 2004. Bubble espect ratio and velocity measurements using a four-point fober-optical probe. Experiments in fluids 36, 326–333.

Mainland, M. E., Welty, J. R., 1995. Use of optical probes to characterize bubble behavior in gas-solid fluidized beds. AIChE Journal 41, 223–227.

Mawatari, Y., Tatemoto, Y., Noda, K., 2003. Prediction of minimum fluidization velocity for vibrated fluidized bed. Powder Technology 131, 66–70.

Moussa, N. A., Fowle, A. A., Delichatsios, M. M., Caron, R. N., Wilson, R., 1982. Advanced design for pulsed atmospheric fluidized bed combustion. Final Rep. to DOE/METC, Morgantown Energy Technology Center.

Müller, C. R., Davidson, J. F., Dennis, J. S., Fennell, P. S., Gladden, L. F., Hayhurst, A. N., Mantle, M. D., Rees, A. C., Sederman, A. J., 2006. Real-time measurement of bubbling phenomena in a three-dimensional gas-fluidized bed using ultrafast magnetic resonance imaging. Physical Review Letters 96, 154504–1–4.

Noda, K., Mawatari, Y., Uchida, S., 1998. Flow patterns offine particles in a vibrated fluidized bed under atmospheric or reduced pressure. Powder Technology 99, 11–14.

Olowson, P. A., Almstedt, A. E., 1990. Influence of pressure and fluidization velocity on the bubble behavior and gas flow distribution in a fluidized bed. Chemical Engineering Science 45, 1733–2176.

Ouyang, F., Levenspiel, O., 1986. Spiral distributor for fluidized beds. Industrial & Engineering Chemistry Process Design and Development 25, 504–507.

Puncochar, M., Drahos, J., 2005. Origin of pressure fluctuations in fluidized beds. Chemical Engineering Science 60, 1193–1197.

Puncochar, M., Drahos, J., Cermak, J., Selucky, K., 1985. Evaluation of minimum fluidizing velocity in gas fluidized bed from pressure fluctuations. Chem. Eng. Commun. 35, 81–87.

Ramaya, A. V., Venkateshan, S. P., Kolar, A. K., 1993. Large particle fluidization studies witha differential pressure fluctuation record. In: Rubow, L. (Ed.), Proceedings of the 12th International Conference on Fluidized Bed Combustion. Vol. 2. ASME, pp. 877–885.

Ramaya, A. V., Venkateshan, S. P., Kolar, A. K., 1996. Estimation of bubble parameters from differential pressure measuremets in gas-fluidized beds. Powder Technology 87, 113–126.

Ran, X., Wei, F., Zhanwen, W., Yong, J., 2001. Lateral solids dispersion in high-density riser with swirling air flow. Powder Technology 121, 123–130.

Rockinger, M., Jondeau, E., 2002. Entropy densities with an application to autoregressive conditional skewness and kurtosis. Journal of Econometrics 106, 119–142.

Rowe, P. N., Masson, H., 1981. Interaction of bubbles with probes in gas fluidised beds. Trans IChemE 59, 177–185.

Roy, R., Davidson, J. F., 1989. Similarity between gas-fluidized beds at elevated temperature and pressure. In: Shemilt, G. . (Ed.), Fluidization VI.

Santana, D., Macías-Machín, A., 2000. Local bubble-size distribution in fluidized beds. AIChE Journal 46, 1340–1347.

Santana, D., Rodríguez-Rodríguez, J., Almedros-Ibáñez, J. A., Martínez-Bazán, C., 2006. Characteristics lengths and maximum entropy estimation from probe signals in the ellipsoidal bubble regime. International Journal of Multiphase Flow 32, 1123–1139.

Schweitzer, J-M., B. J., Gauthier, T., 2001. Local gas hold-up measurements in fluidized bed and slurry bubble column. Chemical Engineering Science 56, 1103–1110.

Sellens, R. W., Brzustowski, T. A., 1985. A prediction of the drop siza distribution in a spray from first principles. Atom. Spray. Technol. 1, 89–102.

Sitnai, O., 1982. Utilization of the pressure differential records from gas-fluidized beds with internals for bubble parameters determination. Chemical Engineering Science 37, 1059–1066.

Sobrino, C., Almedros-Ibáñez, J. A., Sánchez-Delgado, S., de Vega, M., Santana, D., Ruiz-Rivas., U., 2007. Hydrdynamic characterization of a fluidized bed with rotating distributor. In: Bi, X., Berruti, F., Pugsley, T. (Eds.), Fluidization XII. pp. 767–774.

Sobrino, C., Almedros-Ibáñez, J. A., Santana, D., de Vega, M., 2008. Fludization of group b particles with a rotating distributor. Powder Technology 181, 273–280.

Sreenivasan, B., Ragahavan, V. R., 2002. Hydrodynamics of a swirling fluidised bed. Chemical Engineering Science 41, 99–106.

Svoboda, K., Cermak, J., Hartman, M., Drahos, J., Selucky, K., 1983. Pressure fluctuations in gas-fluidized beds at elevated temperatures. Industrial & Engineering Chemistry Process Design and Development 22, 514–520.

Svoboda, K., Cermak, J., Hartman, M., Drahos, J., Selucky, K., 1984. Influence of particle size on the pressure fluctuations and slugging in a fluidized bed. AIChE Journal 30, 513–517.

Talmor, E., Benenati, R. F., 1963. Solids mixing and circulation in gas fluidized beds. AIChE Journal 9, 536–540.

Turton, R., Clark, N. N., 1989. Interpreting probe signals from fluidized beds. Powder Technology 59, 117–123.

van der Schaaf, J., Schouten, J. C., Johnsson, F., van den Bleek, C. M., 2002. Non-intrusive determination of bubble and slug length scales in fluidized beds by decomposition of the power spectral density of pressure time series. International Journal of Multiphase Flow 28, 865–880.

van Ommen, J. R., Mudde, R. F., 2007. Measuring the gas-solids distribution in a fluidized bed - a review. In: Bi, X., Berruti, F., Pugsley, T. (Eds.), Fluidization XII. pp. 31–46.

van Ommen, J. R., van der Schaaf, J., Schouten, J. C., van Wachem, B. G. M., Coppens, M., van den Bleek, C. M., 2004. Optimal placement of probes for dynamic pressure measurements in large scale fluidized beds. Powder Technology 139, 264–276.

Vázquez, C., Nombela, J. L., Sobrino, C., de Vega, M., Zubía, J., Montero, D. S., 2007. Plastic fiber-optic probes for characterizing fluidized beds in bubbling regime. Vol. 16th International Conference on Plastic Optical Fiber (POF).

Verloop, J., Heertjes, P. M., 1974. Periodic pressure fluctuations in fluidized beds. Chemical Engineering Science 29, 1035–1042.

Welch, P. D., 1967. The use of a fast fourier transform for the estimation of power spectra. IEEE Trans. Audio and Electroacoustics AU-15, 70–73.

Werther, J., 1974a. Bubbles in gas fluidised beds - Part I. Trans. Instn. Chem. Engrs 52, 160–169.

Werther, J., 1974b. Bubbles in gas fluidised beds - Part II. Trans. Instn. Chem. Engrs 52, 149–159.

Werther, J., 1976. Convective solids transport in large diameter gas fluidized beds. Powder Technology 15, 155–167.

Werther, J., 1978. Effect of gas distributor on the hydrodynamics of gas fluidized beds. German Chemical Engineering 1, 166–174.

Werther, J., 1999. Measurements techniques in fluidized beds. Powder Technology 2, 15–36.

Werther, J., Molerus, O., 1973. The local structure of gas fluidized beds -I. a statistically based measuring system. International Journal of Multiphase Flow 1, 103–122.

Wilkinson, D., 1995. Determination of minimum fluidization velocity by pressure fluctuation measurement. The Canadian Journal of Chemical Engineering 73, 562–565.

Wiman, J., Almstedt, A. E., 1998. Influence of pressure, fluidization velocity and particle size on the hydrodynamics ofa freely bubbling fluidized bed. Chemical Engineering Science 53, 2167–2176.

Xie, H. Y., Geldart, D., 1997. The reponse time of pressure probes. Powder Technology 90, 149–151.

Yasui, G., Johanson, L. N., 1958. Characteristics of gas pockets in fluidized beds. AIChE Journal 4, 445–452.

Yates, J. G., Simons, S. J. R., 1994. Experimental methods in fluidization research. International Journal of Multiphase Flow 20 Suppl., 297–330.